Bio-Inspired Ice Adhesion Robot FLICK for Exploring Icy Moons

Freezing Locomotion Integrated Chain Kinematics

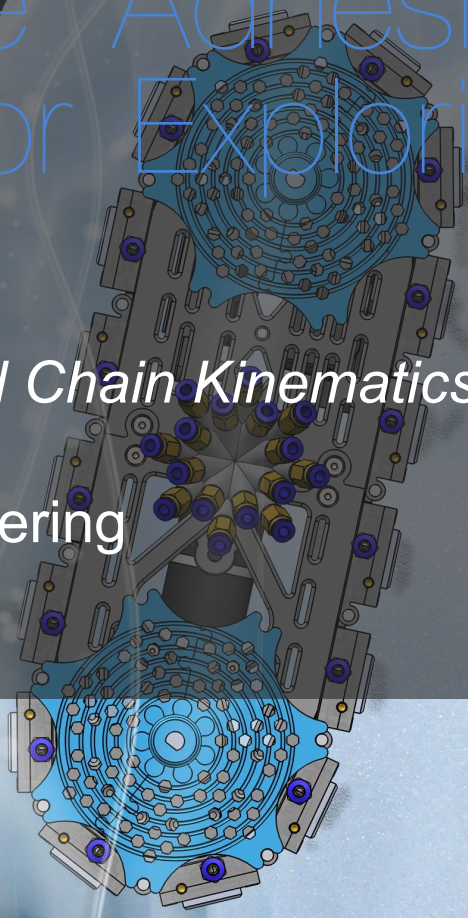

MSc Thesis Mechanical Engineering

Thomas Anthonie Mooijman

Delft University of Technology

TU Delft

Bio-Inspired Ice Adhesion Robot FLICK for Exploring Icy Moons

Freezing Locomotion Integrated Chain Kinematics

by

Thomas Anthonie Mooijman

Student Name	Student Number	Report Number
Mooijman	4393619	**2023.MME.8827**

Daily supervisor: Dr. Stéphanie Cazaux
Supervisor: Dr. Jovana Jovanova
Project Duration: March, 2022 - June, 2023
Faculty: Faculty of Mechanical, Maritime and Materials Engineering, Delft

Cover: Ice adhesion robot in Enceladus' crevasse

TU Delft

Contents

List of Figures

List of Tables

Nomenclature

Abbreviations

Abbreviation	Definition
CAD	Computer Aided Design
CC	Constant Current
CV	Constant Voltage
DOF	Degree of Freedom
EELS	Exobiology Extant Life Surveyor
EVE	Enceladus Vent Explorer
IC	Integrated Circuits
PSU	Power Supply Unit
SPR	South Polar Region
TIM	Thermal Interface Material

Symbols

Symbol	Definition	Unit
α	thermal diffusivity	[m^2/s]
c_p	specific heat capacity	[J/(kg K)]
c_v	volumetric heat capacity	[J/(m^3 K)]
$\dot{Q}$	heat flux	[J/s]
γ	surface energy	[J/m^2]
g	Gravitational Acceleration	[m/s^2]
I	Current	[ampere, A]
k	thermal conductivity	[W/(m K)]
Π	Peltier coefficient	[μ V]
ρ	density	[kg/m^3]
R	Electrical Resistivity	[Ω]
S	Seebeck coefficient	[µV/K]
T	Temperature	[K]
τ	Torque	[Nm]
V	Volume	[m^3]
ZT	Figure of Merit	[-]
P	Pressure	[Pa]

1

Introduction

1.1. Background

In the quest to unravel the mysteries of our solar system, the exploration of distant celestial bodies has captivated the minds of scientists and researchers. Among these intriguing worlds, Saturn's icy moon Enceladus has emerged as a fascinating target for exploration, holding the potential for profound scientific discoveries. In response to this call for exploration, this report presents a project that endeavors to develop a novel robotic system capable of venturing into the enigmatic crevasses of Enceladus.

Enceladus, with its icy crust and subsurface ocean, has piqued the curiosity of scientists due to the tantalizing possibility of harboring conditions conducive to life. Its plumes, erupting from the moon's surface, have offered glimpses into the hidden secrets that lie beneath. However, accessing these elusive crevasses has proven to be a significant challenge. By adapting a bio-inspired approach, this project aims to overcome these obstacles and pave the way for unprecedented exploration.

Following an extensive literature review on bio-inspired robotics, this project aims to develop a new method for effectively scaling icy terrains. The development of this robotic system entails a bio-inspired approach, in an attempt to turn the challenging conditions on Enceladus into opportunities. Taking inspiration from the character 'Flick' in the movie 'A Christmas Story', who experienced the comical mishap of getting his tongue stuck to a metal pole, this research introduces a robotic system that employs the adhesive properties of ice as an advanced locomotion principle, to enable movement on icy surfaces.

1.2. Problem Statement - Research Questions

Employing the adhesive properties of ice for transportation on icy surfaces is an unexplored concept. The feasibility of this concept is evaluated in this research by answering the following questions:

What is required for the development of an ice adhesion technology, that can be integrated in a robotic system capable of traversing icy surfaces?

Which is then divided in the following sub-questions:

- What technologies can be used to effectuate the phase change of water (liquid-solid) at the interface of the adhesive (ice) and substrate?
- What are the essential intrinsic material properties of the substrate to increase adhesive strength?
- What is the effect of the surface treatment of the substrate material on adhesive strength?
- What locomotion method is suitable to employ this adhesion technology?
- How can the mechanical interlocking adhesion technology be integrated in a small scale robotic system?

1.3. Methodology

There is no state-of-the-art in ice adhesion locomotion strategies. In fact, research in ice adhesion is solely focused on *minimizing* ice adhesion strength. Therefore a step-wise approach is adapted in this research, decomposing the problem into smaller, more tangible challenges. The findings at each step greatly influence the design scope or requirements for the next step; evaluating the findings at the end of each step is important before proceeding to the next.

1. Development of a system that can sufficiently and selectively heat and cool a small interface of ice.
2. Selection of a substrate material that has desirable material properties for both ice adhesion and thermal cycling.
3. Combine step 1 and 2 and design the experiment to quantify adhesion strength and asses feasibility for use in robotic system.
4. Integration and miniaturization of ice adhesion technology in robotic system; proof of concept.

1.4. Delimitation of Scope and Key Assumptions

The development of exploration robots is a highly resource-intensive process, especially when it comes to creating systems that can thrive in the extremely unfamiliar conditions both on and inside Enceladus. In light of this, the focus of this project is solely on the locomotion method, with the potential for further expansion if they prove successful. However, it is important to note that this project only considers conditions (e.g. temperature, gravity and pressure) that are found on Earth for the development of the ice adhesion locomotion strategy.

The objective here is not to create an *eierlegende Wollmilchsau*[1], that can address every aspect of the challenge. Such an approach would be time-consuming, costly, and often result in disappointment. Instead, the aim is the aim is to develop the concept of ice adhesion as a locomotion strategy, that then can serve as a starting point for future research and development.

Although not as exciting as Enceladus, development of a system for terrestrial conditions can still prove to be useful. Locomotion methods that enable the transportation of scientific instruments in extreme environments (e.g. glaciers or icy crevasses) can be an valuable asset for the scientific community.

1.5. Outline of the report

Chapter 2 provides the scientific background for each following chapter; a bundled literature review. In particular, it discusses the conditions on Enceladus, state-of-the-art of mission concepts to Enceladus and ice climbing robots. Additionally, multiple 'phase change technologies' are reviewed that can potentially be used as a methods to effectively heat and cool a small interface of ice. The application of these phase change technologies are then also illustrated in the state-of-the-art in ice grippers. And lastly, this chapter discusses the mechanical mechanism and factors of ice adhesion strength. Essentially, chapter 2 is the state-of-the-art, while the following chapters exclusively describe what is researched and developed in this research.

In chapter 3 the thermo-electric system that enables the heating and cooling of a small adhesion pad is developed. It discusses the component selection and design of the ice adhesion effector. The capabilities in terms of temperature of this system is also demonstrated.

Chapter 4 defines important ice adhesion substrate material properties that are derived from the ice adhesion mechanics described in chapter 2. With a set of desirable material properties, a material selection procedure constructs a set of suitable materials, from which two materials are elected that are used to produce the adhesion pads. Apart from intrinsic material properties, three surface treatments that could increase ice adhesion strength are discussed as well.

Chapter 5 describes the experiments performed to quantify the adhesion strength of the developed ice adhesion effector. The results of these experiments should indicate whether an ice adhesion approach can be a reliable, and feasible method for robotic systems to enable movement on icy surfaces.

[1] eierlegende Wollmilchsau is a German phrase that is used to describe a person, process or object that is capable to do or provide everything; an all-in-one solution.

And more specifically, what substrate material and surface treatment is most effective to achieve this goal.

Chapter 6 takes the information gathered during this research and introduces the very first prototype of a robotic system that adapts an ice adhesion locomotion strategy. The functionality, design and materials of this robot are discussed. Most importantly, the capabilities are demonstrated.

Chapter 7 provides a summary of findings during this research and recommendations for future work.

2

Literature Review and State of the Art

This chapter provides an overview of state-of-the-art for all the chapters in this research.

2.1. Conditions on Enceladus

In our solar system, there are two moons that bear the possibility of extraterrestrial life; Saturn´s moon Enceladus, and Jupiter´s moon Europa [49, 9]. For a long time, Enceladus was considered to be a solid mass of ice, but the first images of Enceladus captured during the Voyager encounters in 1980 and 1981 revealed the extraordinarily high albedo and fractured surface characteristics of the moon [79]. Simultaneously, observations from the ground suggested that Enceladus supplied Saturn's E-ring with geyser like activities as a possible source [22]. These observations and hypotheses fueled the interest in the moon, but it was not in the center of attention in Astrobiology until the Cassini mission revealed some of the geologic activities on Enceladus in 2005, during the first flybys of the moon [79, 25].

Orbit and Gravity

Enceladus orbits Saturn every 32.9 hours at a distance of 238,040 km, this places the satellite within the extended E ring; the second outermost ring of Saturn. With an equatorial diameter of 504.2 km, Enceladus is Saturn's sixth major moon, and is placed between Mimas and Tethys [59, 79]. The small diameter of the moon also means a low gravitational acceleration of 0.113 m s^{-2} [79]. The relatively close orbiting satellite Dione, Saturn's fourth major moon, takes twice as long to orbit Saturn, this 2:1 resonance with Enceladus excites an orbital eccentricity of 0.0047.

South Polar Region

Enceladus' South Polar Region (SPR) is of particular interest as the observed plume is emitted from this terrain. Cassini's flybys revealed the large rifts and faulted surface around the south pole [60, 25], these features were nicknamed 'Tiger Stripes'. The tiger stripes consists of four, linear depressions with a combined length of $\sim$500km.

2.1.1. Temperature and Atmosphere

The Saturnian moon Enceladus is one of the brightest satellites in the solar system with a mean geometric albedo of 1.38 [84] and bond albedo of 0.89 [28], which is comparable to that of fresh snow. This supports the suggestion that Enceladus undergoes continuous resurfacing by the plumes of vapor and icy grains emitted from the SPR. The incoming solar radiation is numerically and analytically approximated by Ashkenazy [3]; with a solar constant of 15.14 W m^{-1}, the incoming solar radiation at the equator has an annual mean of $\sim$4.5 W m^{-1}, and the SPR: $\sim$2.2 W m^{-1}. However, most of this sunlight is reflected due to Enceladus' high visible wavelength albedo [27]. Saturn is Enceladus' other external heating source, which has an effective temperature of 95.0 K [27]; almost all Saturn radiation is absorbed by Enceladus as the thermal infrared albedo is very low, contrarily to the visible wavelength albedo. Consequently, the expected surface temperatures on Enceladus are very low, as depicted in figure 2.1, but observations by Enceladus revealed thermal anomalies near at the South Polar Region [29], where surface temperatures of 85 K were recorded in 2005. The unusually high heat output at the SPR further suggest endogenic processes that generate the observed heat. Higher resolution imaging of the SPR allowed to make more accurate estimated of the total power output, which is currently estimated for a total of 4.2 GW, with the addition of 0.5 GW from the plume latent heat and possible inter-fault (tiger stripes) emission [78]; this total is corrected for the passive emission due to re-radiated absorbed sunlight.

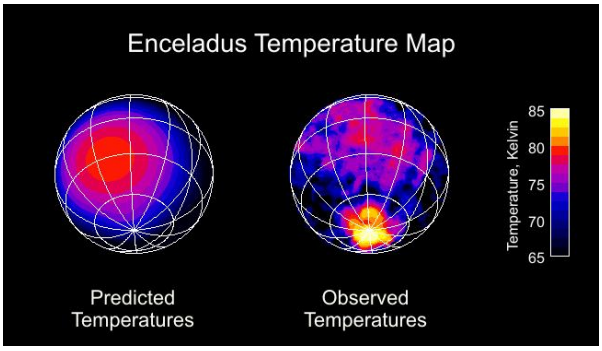

Figure 2.1: Temperature observation of Enceladus by Cassini, 2005. Image credit: NASA/JPL/GSFC [29]

The low gravity on Enceladus, approximately 87 time lower than Earth's gravity, is not able to hold an atmosphere very long. But the observations indicate that there is in fact an atmosphere [18], this atmosphere consists mostly of water vapor with thin traces of carbon dioxide, methane and nitrogen at near vacuum pressure (100 Pa). Enceladus' plume provides a continuous replenishment of the gases.

2.1.2. Surface Topography

As the South Polar Region is of particular interest for potential exploration missions [14, 56, 7], the scale of surface features is of significant importance for landing areas, as well as the mobility challenges imposed by the terrain. The term 'Tiger Stripes' represent V-shaped valleys enclosed by nearly parallel ridges [37], the height of these ridges is estimated between 100 - 150 m, whereas the valleys are between 200 - 250 m deep and the total width of these formations is between 2 - 5km. The four linear depressions are dubbed: Alexandria, Cairo, Baghdad and Damascus Sulcus [53]; referring to names in the 1900 version of the Arabian Nights. The tiger stripes are divided by 'plains' roughly 35 km wide, these plains are relatively flat, but moving closer to the formations the terrain rises with a relatively gentle gradient [37]. A combination of five high-resolution images were combined to create a mosaic that captures part of the Baghdad Sulcus and Cairo Sulcus [29], shown in figure 2.2 on the left, the images on the right are enlarged sections from the left image.

A more detailed (digital) elevation model of the Baghdad Sulcus is derived by Giese et al. [20], this model is illustrated in figure 2.3. The model indicates southwest facing flanking slopes of 30° and slope angles larger than 32° for the northeast facing slopes. The morphology of these slopes is far from smooth, instead it is described as blocky terrain with lineation[1] patterns, in fact, blocks with sizes up to 50 m have been identified [20]. These observations suggest that the shape of the troughs or depressions is determined by neither angle-of-repose, nor venting process, but rather by faulting

[1] Lineations are linear structural features within rocks or in this case, ice.

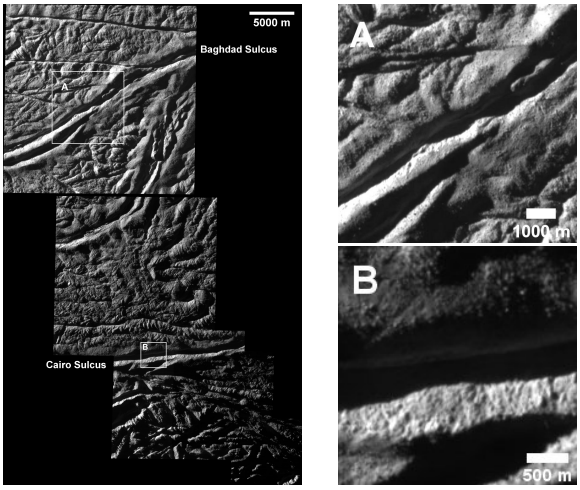

Figure 2.2: Left image: Five combined images captured by Cassini at a distances ranging from 1,288 to 3,600 km; area centered at 81.6°S, 56.6 °W. Right images: Enlarged view of the sections marked (A,B) in the left image. Images adapted from: NASA/JPL [29]

and erosion (e.g. seismic shaking and sublimation). Similarly, the morphology of the narrow valley floor (50-100 m) is dominated by faulting and tidal deformations, interspersed with obstacles such as narrow ridges and icy blocks. Even though the venting processes are concentrated in the valleys of the troughs, the observations suggest only little modification of shape by deposition of icy particles, in and surrounding the valleys.

With the help of twenty high-resolution images, ranging from 5-25m per pixel, Martens et al. [46] examined the distribution of ice blocks on Enceladus, in particular at the South Polar Region. The features that are were identified as 'ice blocks' appear as discrete positive-relief features approximately 10-100 m in diameter, equivalent to the term 'boulders'. These efforts determined that ice block concentration are systematically most concentrated within the South Polar Region, in particular within 15° latitude of the south pole. Furthermore, the highest densities are recorded at the south pole, with concentrations reaching 1500$\pm$450 blocks km^{-2}. Additionally, there is no indication of any spatial correlation or pattern with respect to the tiger stripe fissures and block concentration. Neither impact cratering, nor seismic disturbances are considered to be significant sources for the ice blocks observed in the South Polar Region, as the SPR in particular is lacking impact craters, and seismic disturbances can not account for the observed blocks on top of ridges and peaks, but will affect the appearance of the ice-block fields over time. The ejection of ice blocks by the observed vents can not be entirely ruled out, but would require "catastrophic cryovolcanic eruptions and suitably wide surface fractures". Instead, tectonic disruption of the lithospheric ice is suggested to be the largest contributor to the ice blocks in the SPR. Additionally, vapor condensation around icy fumeroles is hypothesized to have a minor contribution to ice block formation; conduits branching away from the large tiger stripe fissures could form an intricate network of narrow fractures. From these networks, small, diffuse vents can emerge at the surface where vapor condensates and forms block like features, the latent heat from condensation also explains the observed heat anomalies at the SPR. These icy fumeroles can not account for the blocks observed outside the south polar region, however, the relatively high block density around the south pole does support this hypothesis. These observations give indications for the surface features on a $\sim$20 m scale, but the surface topography on lander scales remains uncertain, this would require higher resolution images.

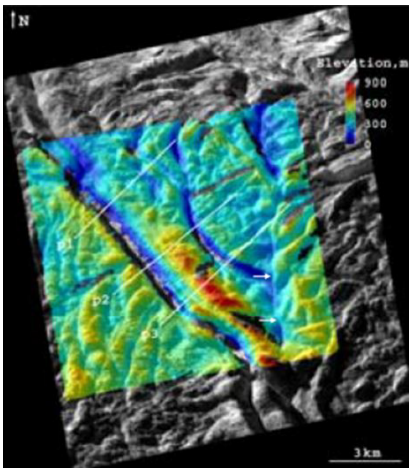

Figure 2.3: Elevation map focused at Baghdas Sulcus (76°S/323°E). Image from [37], image credit [20]

2.1.3. Surface Compostion

Early observations in 2005 using Cassini's Visual and Infrared Mapping Spectrometer were used by Brown et al. [6] to analyse the wavelength absorption spectrum of the Enceladus' surface. With this information they were able to construct images that indicate the surface composition, as shown in figure 2.4. The surface is mostly composed of pure water ice, both crystalline and amorphous. However, near the south pole the absorption spectrum indicates the presence of light organic materials and CO_2.

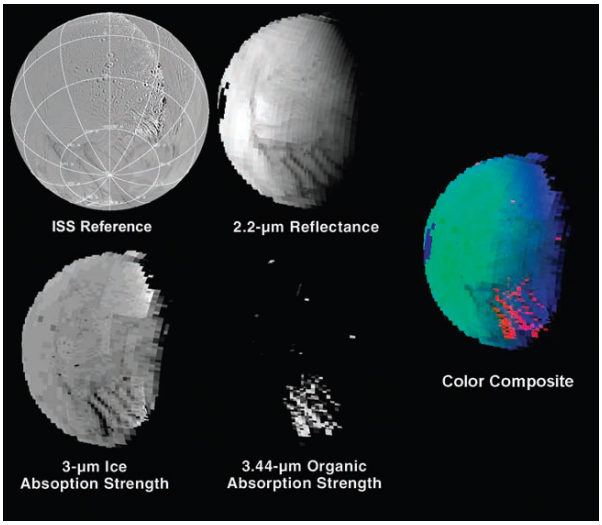

Figure 2.4: Composition map of Enceladus, here the red maps the strength of 3.44 μm organic absorption, green indicates 2.2 μm continuum reflectance to green intensity and blue maps the intensity of 3 μm water-ice absorption to blue intensity. Image from [6]

2.1.4. Enceladus' plume

Together with the extraordinarily high albedo of Enceladus, the erupting plume is one of the most characterizing feature of the moon. Examining the composition of the plume became one of the priorities during the Cassini mission, as it not only teaches about the chemical composition of the moon, but could also reveal some of the underlying mechanics driving the plumes and the conditions and chemical reactions occurring at the ocean-core interface. As Cassini performed numerous flybys, each at different distance, velocity and direction relative to the moon, more data became available over the course of the mission from 2004-2017. Reviewing the data and research performed in chronological order is therefore advised, as the research performed with a more complete data set will generally be of lower ambiguity than early research. A comprehensive review is written by Postberg et al. [62] that elaborates on all the findings regarding the plume and surface composition during the course of the mission and provides a conclusive results as well. The word 'plume' is used here to describe the entire emission originating from the South Polar Region of Enceladus, this plume comprises all individual jets and other sources of emissions.

Plume Composition

Cassini was equipped with 12 different instruments [10] to study Saturn and surrounding atmospheres, Saturnian rings (e.g.: E-ring), Titan and icy satellites (e.g.: Enceladus), a selection of these instruments were used for measuring the composition of Enceladus' plume, jets and coma; in terms of gas, solid materials (i.e. dust) and charged particles.

Neutral gases make up the largest fraction of the plume, as they are emitted with a rate of 170-250 kg/s [24]. Solid material is emitted at much lower rate, but with greater variety as the estimates range from 3-5 kg/s [74] to 50 kg/s [30], 15-65 kg/s [17] and lastly, 20 kg/s [33]. The lower emission rate of solid particles can be accounted to the lower velocity of particles [74], in fact, only 5-10% of particles ejected from jets and other sources are travelling faster than the escape velocity of 239 m/s [59].

2.1.5. Eruptions

The rate at which the plume emits materials (gases, dust and charged particles) from Enceladus is not constant. In fact, there are strong indications that the plume activity is related to the tidal deformations, caused by orbital eccentricity of Enceladus [34]; this orbital eccentricity is a result of the 2:1 resonance with Dione [60]. Diurnal variations in flux are found for both gases [24] and particles [26, 60], and there is indisputable evidence that tidal forces are related to these changes [26]. The exact interaction that relates the tidal forces to the diurnal changes in heat and mass flux is still debated.

Crust Deformations

The diurnal ice crust deformations has considerable impact on the design of an exploration mission and robot. The approaches to reach the subsurface ocean of Enceladus currently proposed, as discussed in section 2.2, either reach the ocean by penetrating the ice shell [36], or by traversing the existing crevasse [7, 56]. The spatial and temporal distributions of pressure and displacements in the ice crust as a result of the tidal deformations is investigated by Běhounková et al. [5], this research included the variations in ice shell thickness in the performed 3D finite element simulations. In fact, four structurally different models of Enceladus' ice shell are simulated; uniform/variable thickness, with/without faults, where a purely elastic response of the ice is assumed. The results, in terms of pressure and displacement, of the four models where Enceladus is at periapsis[2] with Saturn, are illustrated in figure 2.5. The model model that considers a variable ice shell thickness and the tiger stripe fault shows a maximum displacement of 7.39 m, with a deviatoric stress reaching up to 280 kPa. As the displacements are given as absolute values, and no local displacement gradients are available, there can be no conclusions drawn regarding the lateral deformations of the ice from the results in [5]. However, these results do indicate that the ice is subject to frequent deformations that could obstruct or damage any robotic system attempting to penetrate or traverse towards the sub-surface ocean.

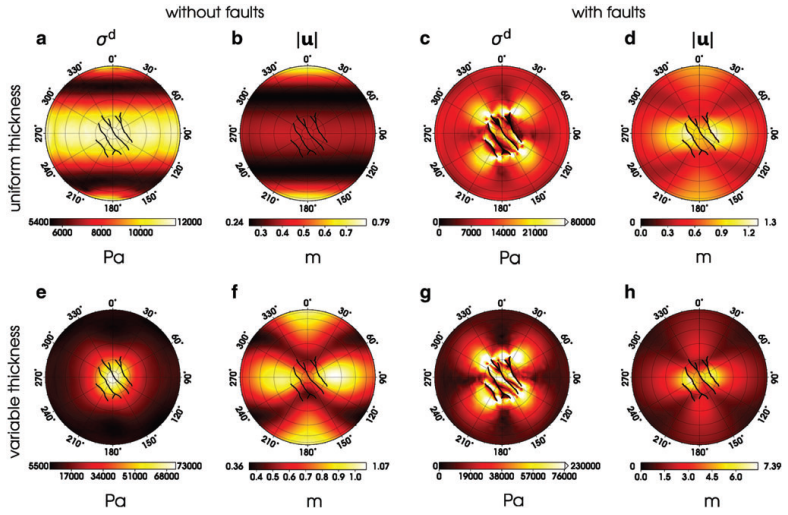

Figure 2.5: Magnitude of deviatoric stress (σ^d) and displacement ($|\boldsymbol{u}|$) at the surface of the South Polar Region of the four different models in Běhounková et al., 2017 Figure from [5]

Crevasse Deformations

The changes in plume activity related to the tidal stresses also suggest that the width of the conduits or fissures in the ice crust could change significantly [26]. In fact, Nimmo et al. [54] propose a crack motio per tidal cycle of 0.5 m slip. Though, the conduits are not expected to completely close, as the level of plume activity never completely ceases. Nevertheless, robotic systems designed to exploit the existing cracks, jets or vents found on the South Polar Terrain to reach the subsurface ocean, should consider the changes in geometry of the environment and be equipped with functions or methods to free themselves when becoming stuck in the conduits and also be able to withstand the forces exerted by the conduit walls.

[2]The point of closest approach for an object (e.g. Enceladus) moving in elliptical orbit around another celestial body (e.g. Saturn).

Nature of Eruptions

There are two distinct suggestions for the nature of the eruptions. First, stereographic imaging was used to investigate the tiger stripe fractures on the South Polar Region of Enceladus, from these measurements, 100 individual jets have been identified by Porco et al. [60], by the method of triangulation. The location of these discrete jets are shown in figure 2.6a. The jets for which the location and tilt have been identified and certain, are denoted with a circle; the diameter indicates the uncertainty in location. For five jets, the location is confirmed but the tilt is uncertain, these are indicated by the dashed circles. The two crosses indicate jets that could only be appointed to the fracture they are located on.

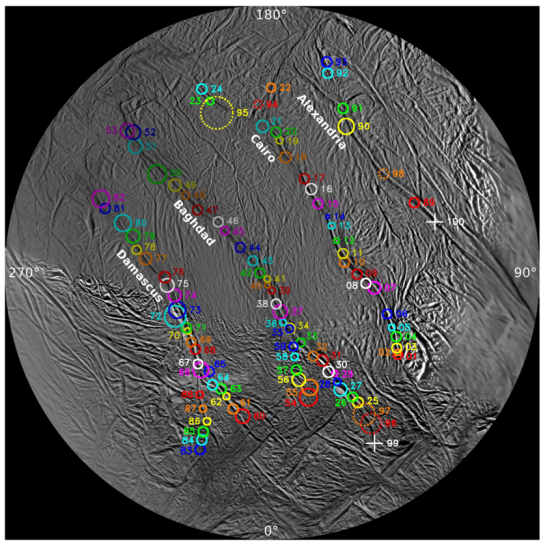

(a) Identified individual jets on the South Polar Region. Image from [60].

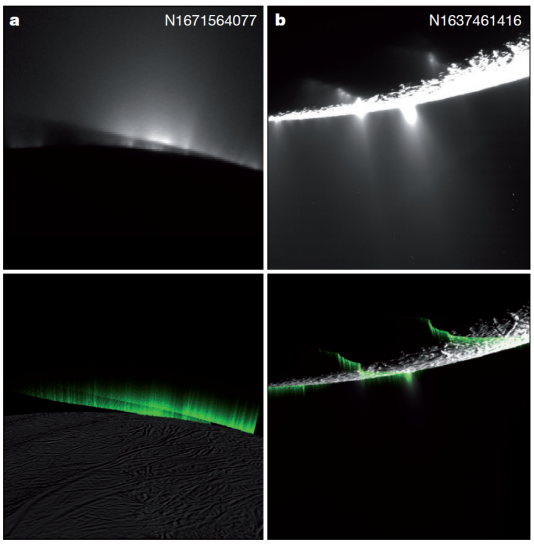

(b) textbfa, Top: cropped image captured by Cassini. Bottom: artificial image displaying the same geometry and proposed curtain eruption. **b**, Top: cropped image captured by Cassini. Bottom: artificial image displaying the same geometry and proposed curtain eruption. Image from [80].

Figure 2.6: Two theories behind the nature of the eruptions.

However, Spitale et al. [80] propose 'curtain eruptions' originating from the tiger stripes, and suggest that the discrete jets identified by Poco et al. [60] are a result of mere optical illusion. Rather than triangulation of the jet-like features among images captured by Cassini, the curtain eruptions are modeled by simulating the appearance of curtains of materials emerging from the tiger stripe fractures. An example of these rendered images is shown in figure 2.6b, these type of jets are labeled as 'phantom' jets. Representing the eruptions as phantom jets demonstrates that there are fewer local eruption sources along the tiger stripes, but the existence of discrete jet sources can not be omitted entirely to explain some of Cassini's observations, however.

2.1.6. Eruption Models

Water Circulation

Matson et al. [47] Matson et al. [48] Matson et al. [47] propose a model with a global ocean beneath Enceladus' ice crust, serving as a reservoir for heat and chemicals. The model assumes a "soda ocean" with dissolved CO_2 and moderate temperatures. Water in hydrostatic equilibrium fills the cracks caused by tidal deformations, eventually reaching the surface due to decreasing bulk density from exsolving CO_2. The water boils vigorously upon surfacing, forming ice when cooled. The model excludes a plume mechanism but incorporates plume chambers. Matson et al. [48] expand the model to explain observed CO_2 patches, illustrating the water circulation process. The trapped CO_2 can seep or burst out, contributing to visible CO_2 patches. The circulation hypothesis requires a molar fraction of 4×10^{-4} dissolved CO_2 in the global ocean and considers a high CO_2 concentration in the plume (5%). However, refined plume composition measurements suggest lower CO_2 concentrations (0.3-0.8%) [62].

Open Slots
Kite and Rubin [34] propose a model where the tiger stripe fissures in Enceladus' South Polar Region are tidally flexed slots in the ice crust, explaining the gas and particle eruptions. The model sustains eruptions throughout tidal cycles, consistent with observations, and matches the power output and IR observations. The slots, represented as rectangular openings, connect the vacuum above and the ocean below, with tidal forces changing their width. The flow of turbulent water generates heat through viscous dissipation and prevents ice formation. The research suggests wider slots increase plume activity due to supersonic flow. However, the model lacks the necessary nozzle or throat for choked flow. The slot width must be within certain limits for sustained eruptions, corresponding to observed phase lag. The proposed slot dimensions make accessing the subsurface ocean of Enceladus more feasible. Observation of individual jets across the fissures challenges the model, but curtain eruptions support it [80]. A slot width of 1 ± 0.5 m is required to sustain eruptions.

Pressurized Chamber
Schmidt et al. [74] propose a model to explain the velocity differences between gases and particles in the plume of Enceladus. The model relies on a large reservoir of water at the triple point, with a liquid-gas interface in the order of square kilometers to prevent ice formation and generate gas production. Evaporated water accelerates gases in channels, where variations in width (choke points) lead to supersonic velocities and gas condensation. Ice grains collide with channel walls, reducing their velocity and being re-accelerated by the gas. The model accounts for water-dominated type-I grains, while Postberg et al. [63, 61] adopted it to explain the formation of larger type-II and type-III grains. The type-III grains are formed from salt-ice condensation cores, accelerated by gas, and with additional water condensing on their circumference. Observations indicate both slow and diffuse sources as well as supersonic, collimated gas jets, with eight jet-like particle sources providing most of the larger type-III grains. Proposed channel width is $\sim$0.10 m.

Controlled Boiling
Nakajima and Ingersoll [52] propose a controlled boiling model for Enceladus' plume. The model considers water-filled cracks with different geometries and isostasy determines the water table height. The boiling is regulated by back pressure in the cracks caused by gas flow. The model matches the observed infrared radiation (4.2 GW [78]) by conducting latent heat from water condensation on icy walls near the tiger stripe fissures. Different crack dimensions have been evaluated to match gas and particle flux and estimated power output. A total crack length of $\sim 1.7 \times 500$km is required to obtain the observed 4.2 GW power output. Preferable crack widths are estimated between 0.05 and 0.075 m for straight and parallel cracks, while tapered and tortuous cracks can also account for wider crack widths without increased vapor production rates. Straight parallel cracks of 0.05 m to 0.075 m might be considered infeasible as they would close every tidal cycle, causing jet activity to cease.

2.2. Sub-surface Exploration Robots for Enceladus

In order to reach definitive answers regarding the question:'Is there life on Enceladus', the only option is to explore the subsurface ocean. There are multiple proposals and concepts for missions to explore Enceladus' subsurface ocean, these will be discussed in this section. However, to increase the odds of a successful mission, more information regarding the conditions on Enceladus exterior is required. There are also missions proposing a dedicated orbiter for Enceladus, with specialized instruments to observe Enceladus' surface and probe the plume for indications of life (e.g. [44]). These orbiting mission proposals are not included.

2.2.1. Enceladus Vent Explorer (EVE)

The Enceladus Vent Explorer (EVE) [56] mission aims to reach Enceladus' subsurface ocean by descending into erupting jets in the South Polar Region. EVE consists of a Surface Module and multiple Descent Modules. The surface module is a lander that provides power and communication to the descent modules. The lightweight descent modules are climbing robots with Ice Screw End Effectors on their limbs, allowing them to anchor on icy walls. The climbing speed of the descent modules is 5.5 m hr^{-1}.

The Ice Screw End Effectors serve as anchor points for the climbing robots and can integrate sample collection tools [12]. Tests have shown that the holding force and weight required for insertion depend on ice quality and density. While the screws can support loads over 350 N in good-quality ice, they failed to support any load in hoarfrost ice. This raises concerns for situations where ice density can not be guaranteed.

The descent modules are connected via a tether for power and communication. Different types of descent modules are proposed: scout modules for identifying routes, in-situ science modules for measurements, and sampling modules for storing samples. Refer to figure 2.7 for an illustration of these modules.

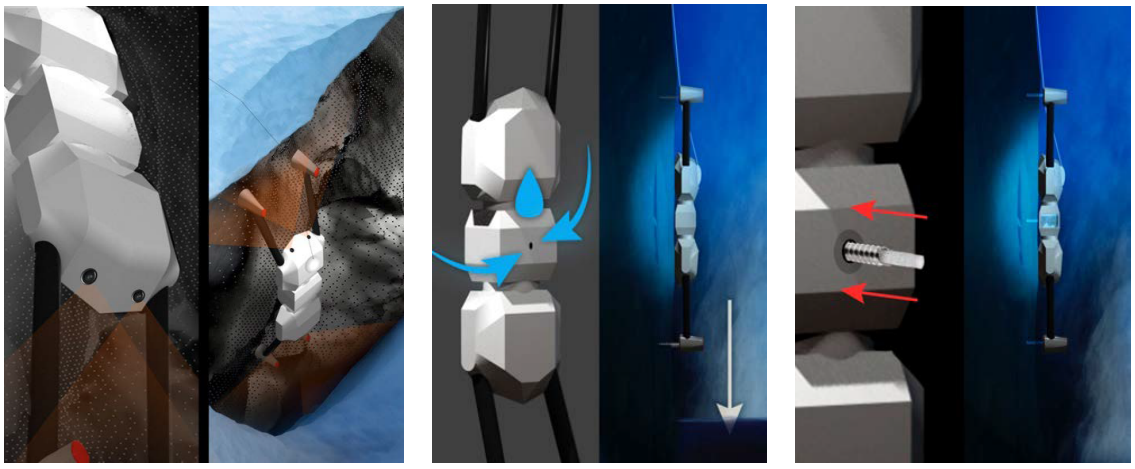

(a) Scout module equipped with mapping devices to create detailed 3D maps of the geyser system.

(b) In-situ science module equipped with miniaturized science instruments such as a microscopic imager and microfluidics chips for bio-signature detection.

(c) Sample return module that is equipped with an additional ice screw in its core section, this ice screw can collect samples, which are returned to the surface module.

Figure 2.7: Three different descent modules to scout Enceladus' crevasses. Images from [56]

2.2.2. Exobiology Extant Life Surveyor (EELS)

NASA's Jet Propulsion Laboratory developed a different approach to reach Enceladus' subsurface ocean, dubbed Exobiology Extant Life Surveyor (EELS) [7]. This radical design is inspired by screw propelled vehicles formerly implemented in amphibious and icy environments, but here the screw propulsion acts as the 'active skin' of the adaptable snake-like robot. The idea of an archimedean screw propulsion skin first explored by Richter et al. [65] (albeit funded by NASA Jet Propulsion Laboratory), who developed a modular system with scalability in mind, such that the system can be extended to an arbitrary number of linked segments. Each segment is linked via actively controlled 2-DOF U-joints, creating a hyperredundant robotic system that requires appropriate control allocation and communication between the agents (segments). The prototype in [65] was constructed with four of these segments, creating a 9-DOF robot, as shown in figure 2.8. This prototype which was proven to be effective in terms of locomotion in different environments, and also functioned as proof of concept for the EELS project.

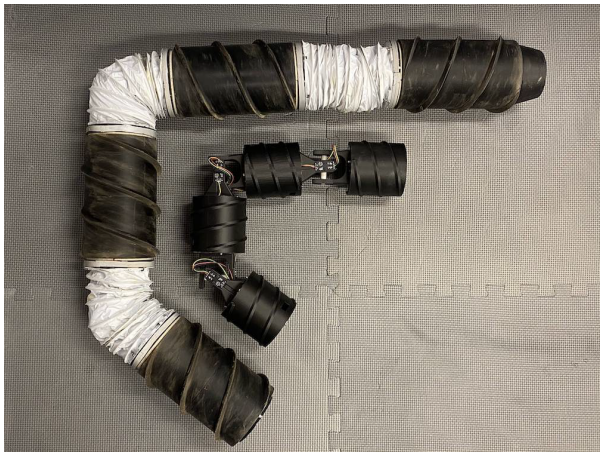

Figure 2.8: ARCSnake together with smaller 'Voodoo Doll', used to control ARCSnake. Image from [65]

2.2.3. IceMole

Instead of conquering the challenging crevasses to reach the subsurface ocean, Dachwald et al. [14] developed a steerable ice melting probe that has been successfully tested in 2010 and 2012 on glaciers in Iceland and Switzerland. This melting probe could be used to probe liquid water in the fissures by following an inclined trajectory from the surface to the fissure. Alternatively, this probe could melt straight down to reach the subsurface ocean, which would take significantly longer. The melting probe currently knows three iterations, IceMole I, II and the latest revision is the EnEx-IceMole probe, as part of the Enceladus Explorer mission [36]. The EnEx-IceMole probe, as shown in figure 2.9, has a 15×15 cm rectangular cross sectional shape, while the overall length of the robot depends on the payload dimensions and required maneuverability. The melting head is equipped with an ice screw to ensure contact with the ice, even on low gravity environments such as Enceladus. The torque generated by the ice screw is supported by the rectangular body of the probe. Additionally, a hollow, retractable needle is fitted inside the ice screw that is used to gather samples. Furthermore, differential heating of the head can drive the probe into a curved trajectory, as the probe is subjected to a torque perpendicular to the longitudinal axis of the robot. Consequently, the melting probe is not limited to trajectories in favor of gravity, but is capable of melting horizontally or upwards as well, which is confirmed by field tests.

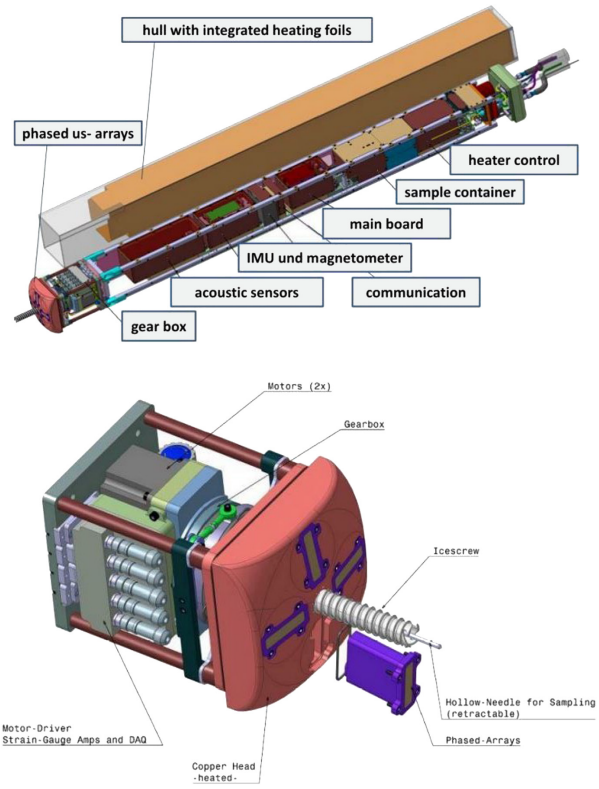

Figure 2.9: Detailed drawings of the latest EnEx-IceMole hull (top) and melting head (bottom). Image from [36]

The required energy to melt through the ice depends heavily on the temperature and desired melting speed; for a melting rate of 1 m hour^{-1}, ice temperature of 150 K, cylindrical probe 1 m in length and 0.1 m in diameter, the estimated required input power is 5 kW [36], also considering the conductive heat losses. A nuclear power system is proposed to supply the high power demand of the probe, as solar power generation is infeasible due to the low solar irradiance on Enceladus and chemical energy (e.g. batteries) are not sufficient to supply the required power over significant timescales. The nuclear power plant would be stationed on the surface, where the generated heat is converted to electrical power through thermoelectric heat exchangers or Stirling converters.

2.2.4. Hybrid Thermo-Mechanical Ice Probe

The simplicity of ice melting probes comes with high power demands. To address this, Wilcox et al. [86] proposed a hybrid mechanical ice probe (Figure 2.10a). It features a circular saw blade that cuts the ice and a rotating dome to chip away the ice evenly. The crushed ice is melted by a heat source, and the melt water is collected and ejected by rotary pumps. This hybrid probe is more efficient than melting probes due to reduced conductive heat losses and can transfer samples to the surface for analysis.

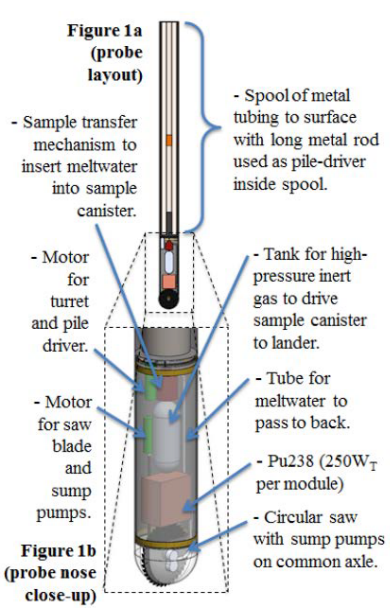

(a) Key features of the mechanical ice probe. Image from[86]

(b) 'SLUSH' hybrid thermo-mechanical probe[91]

Figure 2.10: Two thermo-mechanical ice probes.

Another hybrid thermo-mechanical probe, called 'SLUSH,' is being developed by Honeybee Robotics and NASA Jet Propulsion Laboratory for exploring Europa [91]. 'SLUSH' (Figure 2.10b) is designed for the unique conditions on Europa and features a heated percussive drill bit and a rotating auger to transport the resulting slush-like ice. It utilizes a thermal approach to melt through the subsurface ice. The probe is powered by NASA's Kilopower fissure reactor and incorporates detachable sections for wireless communication with the surface module.

While purely mechanical drilling is theoretically efficient [15], handling removed ice and compaction present challenges. Pure melting systems are less complex, but also less efficient. Hybrid systems offer a potential solution by combining the strengths of both approaches, albeit with higher complexity.

2.3. Ice Climbing Robots

There is only one record of a developed ice climbing robot: JPL's IceWorm robot [13]. This system moves according to the inchworm movement and uses alpinist ice screws that are attached at either end of the robot for anchoring to icy surfaces, as shown in figure 2.11. These ice screws are alternately inserted and retracted, making sure that one screw is anchored at all times. The body consists of two rigid segments connected via a 1-DOF (Degree of Freedom) active joint, the Ice Screw End Effectors also are attached to the segments with 1-DOF joints. This robot is tested successfully tested in glacier caves of Mt St Helen; tests in firn caves were unsuccessful due to low anchoring forces in low density hoarfrost ice.

Figure 2.11: IceWorm robot climbing on ice. Image from[13]

2.4. Ice Grippers

The concept of employing the adhesive properties of ice as a positive effect is not completely novel. Thus far, the concept has been researched for manipulating textile products [81] or micro-objects such as tiny optical or electrical components [35, 42, 69, 90, 89].

Cryo-Gripper

The cryo-gripper was developed for handling textile products as existing gripper designs lack flexibility in terms of handling tasks and textile type compatibility. This gripper uses a peltier element to form the material adhesion. By spraying the textile materials with small droplets of water, the gripper can cool the liquid to establish an adhesive connection without any damage to the textile. This adhesive connection is reversible by reversing current flow through the peltier element, and a burst of compressed air speeds up the release. The hot side of the peltier is cooled with low temperature compressed air. A schematic overview of this concept is illustrated in figure 2.12. First prototypes were able to create adhesive bonds up to 8 N/cm^2.

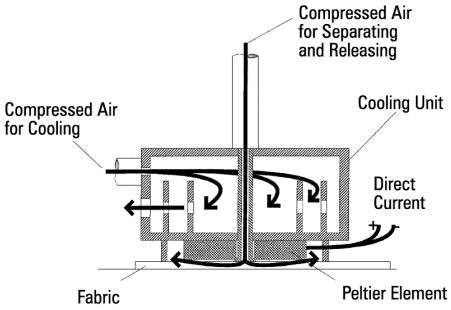

Figure 2.12: Conceptual design of the Cryo-Gripper. Image from: [81]

Ice Tweezer

The Ice Tweezer is a novel tool for manipulating mini/micro objects and employs the freezing force of a small volume of nucleotide ice. Essentially, this tool has a small tip that can be cooled to freezing temperatures, such that small objects in aqueous state can be adhered and manipulated. Alternatively, a small droplet of liquid water can act as the adhesive agent between the tip and object. This concept is developed using various phase change technologies. First project to develop this ice adhesion microgripper was the Eureka Microgrip project, which uses a small peltier element covered with a thin film of water to seize and handle small optical, electrical and mechanical components 0.1 to 5 mm in size [35]. Tests have shown grip strength of approximately 1 N/mm^2, roughly 12.5 times higher than the Cryo-Gripper.

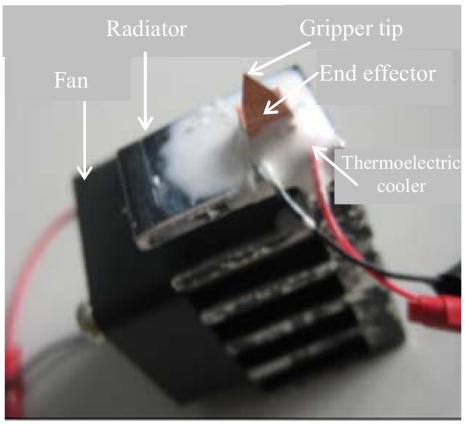

(a) Thermoelectric ice gripper. Image from [69]

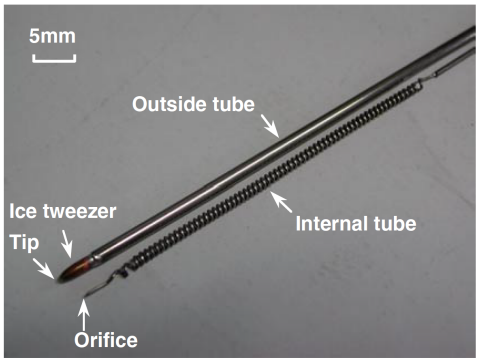

(b) Parts of the Joule-Thomson based Freeze Tweezer. Image from: [42]

Figure 2.13: Two ice grippers for manipulating micro sized objects in aqueous state.

The ice gripper with a 100 µm copper tip, developed by Ru et al. [69] also employs the thermoelectric effect in a 5-DOF robotic manipulator, this gripper is shown in 2.13a Then, the Freeze Tweezer developed by Liu et al. [42] was first developed using the Joule-Thomson throttling effect. Where the expansion of high pressure nitrogen caused immediate cooling of a small copper tip. In later projects, the Freeze Tweezer was adapted to a convective cooling method [90], that allowed to further miniaturize the tweezer tip down to 20 µm. In this case, the tip is cooled by ventilating low temperature gas to the copper tweezer tip.

2.5. Phase Change Technologies

The intrinsic properties of water can help to identify possible methods to effectuate the phase change of water. The phase diagram of pure water is illustrated in figure 2.14. The red, horizontal line represents a temperature change at constant ambient air pressures (1 atm), the leftmost point indicates the melting/freezing point, the rightmost point indicates the boiling/condensation point. Moving horizontally along this line in the diagram represents temperature change at constant pressure. Additionally, this diagram also indicates that changing the pressure of water can induce phase change, i.e. moving vertically in the phase diagram, this pressure induced melting of ice and refreezing when pressure is relieved, is known as regelation [77]. However, pressure-induced melting requires pressures in the order of tens to hundreds of MPa, making it impractical for small robotic systems. To illustate this, the blue line represents water at a constant temperature op -5°C. Starting at ambient pressure (1 atm), the pressure would have to be increased locally to approximately 17 MPa to reach the melting point with constant temperature. These pressures can exceed the compressive strength of ice (5 - 25 MPa), and reaction forces involved in applying such pressures need to be considered. Pressure induced phase change will therefore not be considered. Instead, temperature induced phase change methods will be the focus of this research.

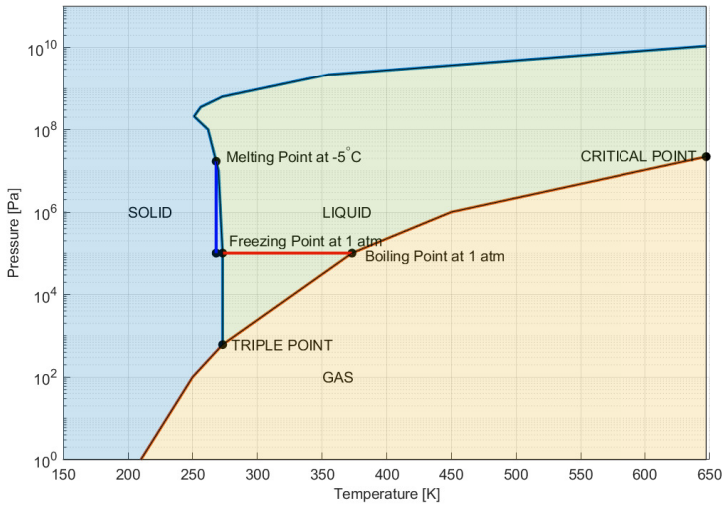

Figure 2.14: Phase diagram of pure water. Data from: [11]

2.5.1. Joule-Thomson Throttling

Methods for heating are often less complex than for cooling, because there are many irreversible processes that can generate heat. The entropy of a closed system is always increasing, and internal energy of the system can be dissipated as heat. However, to achieve cooling, work must be done to reduce the systems entropy. A common method to achieve cooling of a system is the Joule-Thomson throttling effect. This method is used in the refrigeration cycle to lower the pressure and temperature of a fluid. In the refrigeration cycle, this fluid is then evaporated, absorbing heat energy from the surroundings. The Joule-Thomson throttling effect is illustrated in figure 2.15, this process is isenthalpic. Fluid on the left side of the porous plug with pressure P_1 and temperature T_1 is forced to expand adiabatically through the porous plug. This adiabatic expansion from a high-pressure to low-pressure region causes a drop in temperature so that $P_1 > P_2$ and $T_1 > T_2$, while the volume increases $V_1 < V_2$. The nature of the gas, as well as the initial pressure and temperature determines whether the effect produces cooling (positive Joule-Thomson effect), or heating (negative Joule-Thomson effect).

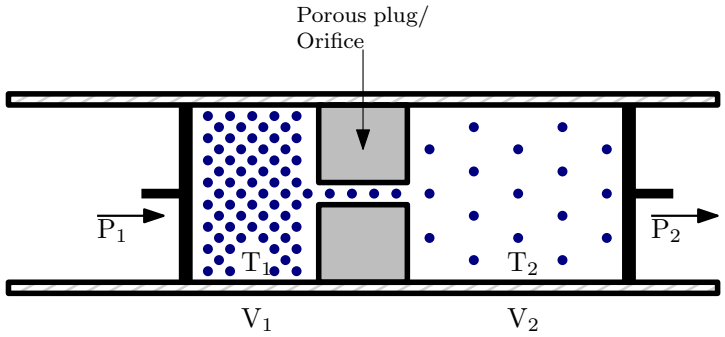

Figure 2.15: Diagram of Joule-Thomson throttling.

In a refrigeration cycle, the fluid is circulated in a closed loop. This closed loop system consists of four main components: a compressor, condenser, expansion device (Joule-Thomson effect) and a evaporator. The size and weight of the combined components make it unsuitable for small scale robotic systems. However, the Joule-Thomson effect can also be employed individually to create the cooling effect, making miniaturization more feasible. This is implemented in the 'Freeze Tweezer' developed by Liu et al. for manipulating mini/micro objects in an aqueous state [42]. The Joule-Thomson effect is used to rapidly cool a metallic tip by expanding high pressure gas through a small orifice located within the tip, as shown in figure 2.16. Objects must be in aqueous state to be manipulated by the Freeze Tweezer, so that an ice ball can form between the tip of the Freeze Tweezer and object.

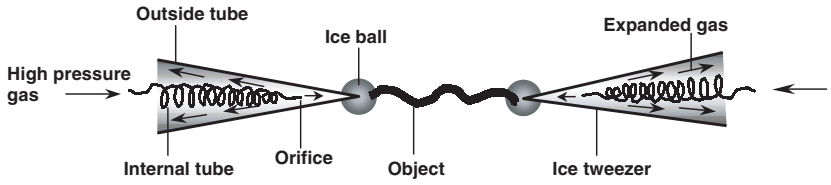

Figure 2.16: Schematic overview of the Freeze Tweezer employing the Joule-Thomson effect. Image from:[42]

This miniaturized Joule-Thomson device uses high pressure nitrogen gas to cool. The nitrogen gas is supplied with a pressure of 10 MPa. Storing, and carrying high pressure gas tanks on small scale robotic systems is a complicated task. And in addition, high pressure systems carry safety risks and are most applicable in controlled environments, such as industrial settings.

2.5.2. Thermoelectric Effect

Another approach is to implement the thermoelectric effect, which can generally be categorized in the following principles: the Seebeck and Peltier Effects. The Peltier effect is commonly used for small-scale localized cooling in electronics [83], while the Seebeck effect is used for temperature measurements (e.g. thermocouples) and power generation. In fact, the Seebeck effect has proven to be indispensable for space applications, such as NASA's Cassini and Voyager missions, both using radioactive thermoelectric generators to power the onboard electronics over the course of the mission. Because the thermoelectric effect relies on the coupling between electrical and thermal currents in materials, suitable materials conduct both heat and electricity [72].

Peltier Effect: Working Principle

Peltier devices (also known as peltier modules, elements or chips), are constructed with P- and N-type doped semiconductors that are connected via a 'junction', which is a metallic conductor. P-type semiconductors have electron 'holes' in the crystal structures, caused by the addition of a trivalent impurity during the manufacturing process. Contrarily, N-type semiconductors are created by the addition of a pentavalent impurity, therefore increasing the number of electrons for conduction in the crystal structure. A simplified, schematic overview of a single thermoelectric couple with P- and N-type semiconductors in refrigeration mode (Peltier) is shown in figure 2.17a. Peltier modules are generally constructed with many P- and N-type semiconductors connected in series via junctions, sandwiched between a dielectric material, such as ceramic, to achieve solid-state refrigeration. The construction of a typical peltier device is shown in figure 2.17b

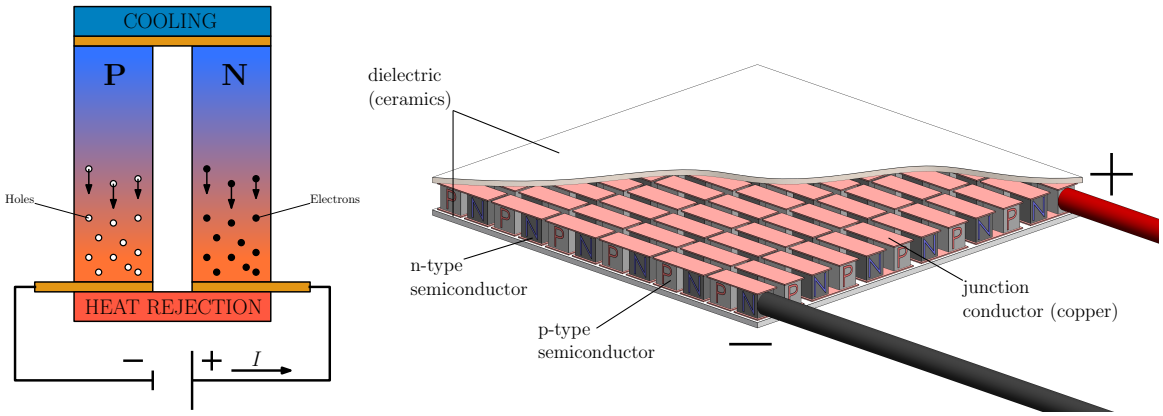

(a) Schematic overview of the peltier effect.

(b) Typical construction of peltier devices

Figure 2.17: Schematic overview of the peltier effect and construction of peltier elements.

Since the conductance and valence band do not overlap in semiconductors, as opposed to conductors, there is an energy gap that the electrons/holes need to overcome at the metal-semiconductor junction. The holes and electrons use thermal energy to jump the energy gap between the bands, absorbing heat (cooling) while being forced away from the cold end of the semiconductors by the applied voltage; imposing a temperature difference between both ends of the semiconductors. In this case, the direction of the current determines whether the junction absorbs or rejects heat. This effect can also be used in reverse, i.e. imposing a temperature difference on the semiconductors, to obtain a voltage difference and therefore, generate power (Seebeck effect). This reversibility is no coincidence, the Seebeck and Peltier effect are in fact closely related, given by equation 2.1.

$$\Pi = ST \tag{2.1}$$

Here Π denotes the Peltier coefficient, S the Seebeck coefficient and T is the temperature in Kelvin. The Seebeck coefficient is related to the ratio of voltage developed and temperature gradient $\frac{\Delta V}{\Delta T}$ and is expressed in $\mu V K^{-1}$.

The heat absorbed or generated at the junction is given by:

$$\dot{Q} = SIT \tag{2.2}$$

with, I the current passing through the semiconductor. This indicates that the heat flow is proportional to the current applied to the semiconductor. Connecting two (P- and N-type) semiconducters in series via a junction, the heat flow is expressed using the Peltier coefficient of both materials, as follows:

$$\dot{Q} = (\Pi_p - \Pi_n)I \tag{2.3}$$

Considering the thermal conductivity K of the couple, which influences the heat flow in the materials, together with the electrical resistivity R of the material, causing Joule heating (also known as I^2R losses/heating), the coefficient of performance (COP) of a Peltier couple can be constructed. The COP is the ratio between net heat pumping rate Q_c and input power W[83]:

$$COP = \frac{Q_c}{W} = \frac{(S_p - S_n)IT_c - K\Delta T - \frac{1}{2}I^2R}{I[(S_p - S_n)\Delta T + IR]} \tag{2.4}$$

Here subscript c references to the cold side of the peltier, and ΔT denotes the temperature difference between the cold and hot side of the module.

Good thermoelectric materials should have a high Seedbeck coefficient, high electrical conductivity and low thermal conductivity. To evaluate and compare materials, the dimensionless figure of merit ZT is commonly used [66].

$$ZT = S^2\sigma T/k \tag{2.5}$$

The highest recorded ZT value found in highly specialized materials is 3.0; the best commercially available peltier modules have materials with a ZT value of around 1.0. For comparison, a ZT value of 1.0 equates to 10% of Carnot efficiency. To obtain similar efficiency as found in home refrigeration (around 30% Carnot efficiency), a device with a ZT value of 4 is required [93].

Temperature and Peltier Types

The maximum temperature difference between the hot and cold side of a single peltier couple, or array can achieve at the present is 91K [85], this difference however, is dependent on the working temperature of the device. Additionally, commercially available modules have a max ΔT of roughly 70K. Higher temperature differences can be achieved by arranging multiple devices in parallel, also known as 'multi-stage' or 'cascading' peltier devices. The simplicity and lack of moving components make peltier devices highly customizable, therefore they can take many different forms, as illustrated by figure 2.18.

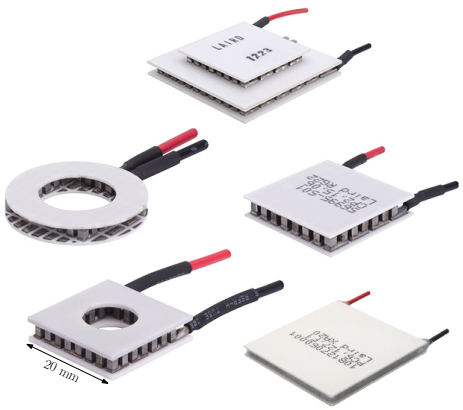

Figure 2.18: Peltier modules with different configurations. Image from: Laird Thermal Systems [82]

Heat Dissipation

Apart from performing as a solid-state heat 'pumps', the internal resistance of peltier modules create additional I^2R heat that needs to be dissipated as well, as indicated by equation 2.4. Heat accumulates at the hot side of the module. If this heat is not properly dissipated to the surroundings, the temperature difference will shift to higher temperatures and the cold side temperature of the peltier will rise as well. Completely failing to dissipate the heat from the hot side of the peltier can cause the solder joints in the module to melt, or breakdown of the semiconductor materials. Proper heat dissipation measures (i.e. heatsinks) are therefore essential for obtaining desired performance from the peltier modules. Common heat dissipation methods include: natural convection, forced air convection and liquid heat exchangers, illustrated in figure 2.19. A review on thermoelectric cooling systems by Riffat and Ma, 2004 [66] shows the typical temperature difference between hot side temperature and ambient of the three methods:

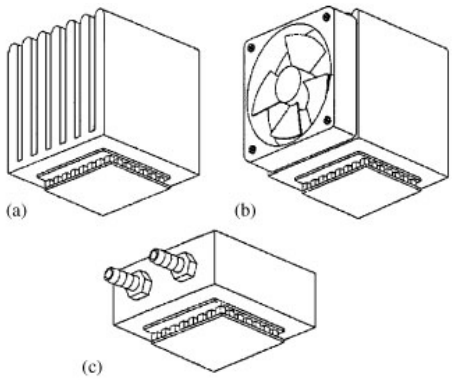

Figure 2.19: Common heat dissipation methods: (a) natural convection, (b) forced air convection, (c) liquid exchangers, Image from: [66]

- Natural Convection: 20-40 K
- Forced Air Convection: 10-15 K
- Liquid Exchangers 2-5 K (above liquid temperature)

Indicating that liquid heat dissipation methods are most effective in keeping the hot side temperature close to the ambient, or in this case the temperature of the liquid.

2.5.3. Selection of technology

For this project, the thermoelectric effect is selected to be used as the phase change technology in the switchable ice adhesion effector. This approach has some advantages over the Joule-Thomson throttling effect. For example, the thermoelectric effect does not have any moving parts or high pressure gases. Similarly, the peltier elements are very compact and are more easily controlled, as they operate on electrical power. The heating or cooling operation of the element is simply enabled by reversing the electrical polarity. Peltier elements are commercially available, as 'off-the-shelf' components, facilitating prototyping process.

2.6. Ice Adhesion Mechanics

The mitigation of ice accretion and minimizing adhesion strength of ice is the main focus of studies in the subject of ice adhesion. In fact, ice adhesion is a wide spread issue in all sorts of industries; in the aerospace industry it has led to a large number of casualties and is a very costly issue. Ice adhesion has therefore been an increasingly popular research topic, with more than 60 publications in the year 2019 [67]. Early investigations report ice adhesion strength of metallic substrate materials surpassing the cohesive strength of ice, resulting in cohesive fractures [1]. In spite of the abundance of available research, the vast majority of studies focus on developing materials or surface coating to minimize adhesion strength, with the exception of an ice adhesion inspired, reversible adhesive material [43]. The development of so called 'icephobic' materials is subdivided in the following categories [94]: the ability of a surface to repel incoming water droplets in cold environments, the ability of a surface to delay or prevent ice nucleation and/or the reduction of adhesion strength. For the application of a ice adhesion actuator, it is desired to maximize adhesion strength between substrate (adhesion pad) and adhesive (ice). Nevertheless, the available studies can still be useful to provide the important intrinsic and extrinsic material properties for ice adhesion.

The adhesive properties of ice -adhesive- to a surface -substrate- can be accredited to multiple factors including, intermolecular contributions such as, electrostatic forces, hydrogen bonding and van der Waals forces [94, 71]. Additionally, the mechanical interlocking effect is also a large contributor to ice adhesion strength [94, 8, 95], although the effect can also occur on a larger scale than prior mentioned effects. These effects are illustrated in figure 2.20. Atomistic or nanoscale modeling is performed in more recent studies [88] in an attempt to better understand ice adhesion and develop icephobic materials. While studies inspecting ice adhesion on continuum scale determined essential relationships between ice adhesion strength and surface (free) energy, initial crack size and elastic modulus [8, 55, 95]. Other important variables are ice type, purity and temperature [31, 1, 68].

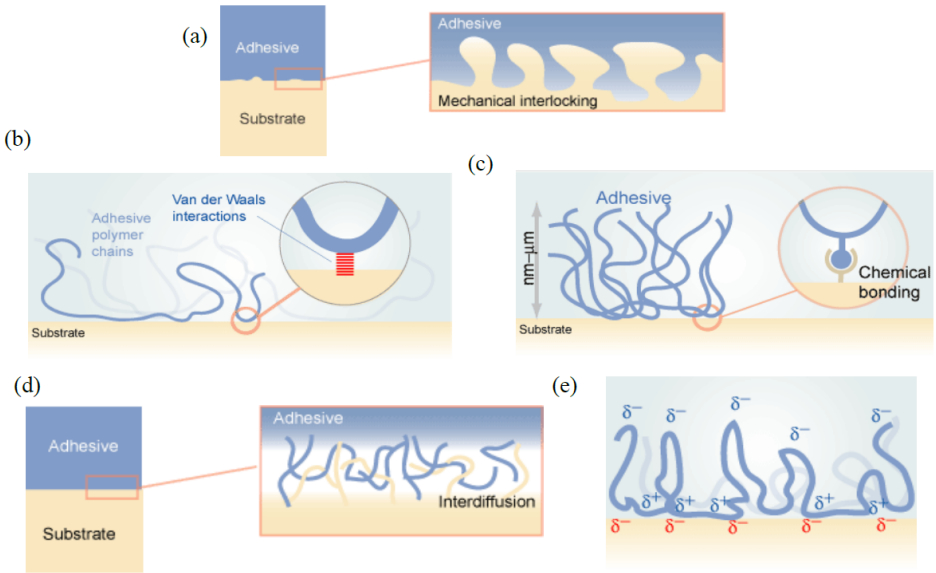

Figure 2.20: Five types of adhesion: (a) mechanical, (b) dispersive, (c) chemical, (d) diffusion and (e) electrostatic. Image from [75]

2.6.1. Surface Energy

'Surface energy' can be used to describe the surplus energy of a material at the surface in comparison to the bulk of the material. At the bulk of a material, molecules are surrounded by identical or similar molecules, creating a zero-net force on the molecules, thus they are in equilibrium. However, when a new surface is created, this equilibrium of intermolecular bonds is disrupted, and the work done by creating this new surface is quantified as surface energy in N/m, equivalent to J/m^2; comparable to surface tension of liquids. It is impossible to directly measure surface free energy, but it is closely related to wettability. While typical approaches include water contact angle measurements, surface energy is a quantitative property of a material and describes the intermolecular forces at the surface, and is therefore, not dependent on the liquid used. Additionally, water contact angle or wettability is highly dependent of the surface roughness of a material [38]. The most used model of surface energy is the OWRK model [32], this model identifies two components: dispersive and polar interactions. Dispersive interactions include van der Waals forces, while polar interactions are dipole-dipole interactions and hydrogen bonding.

In 2012, Makkonen described the relation between water contact angle, surface energy and ice adhesion [45]. This theory considers a drop of liquid water (w), on a solid substrate (s) with a corresponding interface (w,s), surface energies γ and water contact angle θ, illustrated in figure 2.21. Then, Young's equation is used to describe the relationship between contact angle and surface energies:

$$\gamma_{w,s} + \gamma_w cos\theta = \gamma_s \tag{2.6}$$

Now, consider the drop of liquid water in figure 2.21 is frozen into ice (i) onto the (same) solid (s). The thermodynamic work W_a to break the bond at the interface (i,s) without deformations and form two new surfaces (i) and (s) is given by:

$$W_a = \gamma_s + \gamma_i - \gamma_{i,s} \tag{2.7}$$

Combining equation 2.6 and 2.7 gives:

$$W_a = \gamma_i + \gamma_w cos\theta + (\gamma_{w,s} - \gamma i, s) \tag{2.8}$$

This can be simplified, considering that the surface energies of liquid water and solid water (ice) are nearly identical:

$$W_a \approx \gamma_w (1 + cos\theta) \tag{2.9}$$

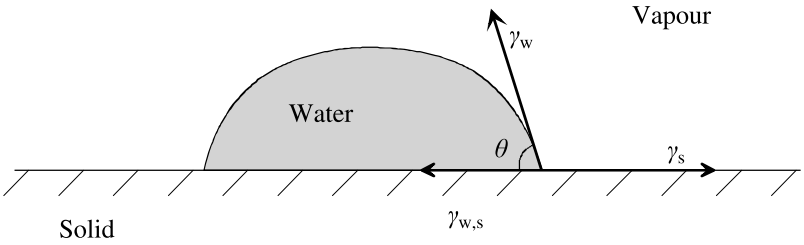

Figure 2.21: Water drop on a solid surface with contact angle θ. Image credit: Makkonen, 2012 [45]

The work in separating ice from a solid at an interface is a result from a force $F(x)$ working over a distance δx:

$$W_s = \int_0^{\delta x} F(x)\, dx \tag{2.10}$$

The distance δx is the required distance for the surfaces to be separated. For ideal conditions, i.e. perfectly rigid materials and surfaces, these distances are on molecular scale.

This theory leads to a deterministic and reversible (if δx is small enough) relationship between the work required to break the adhesion and contact angle, but experiments have shown that this relationship is incomplete and underestimates the required energy to break the ice-solid interface [45]. For example, macro-scale experiments of an ice-steel interface indicate a fracture energy of 1.1 J/m^2, while the relation given by equation 2.7 results in 0.09 J/m^2 for the same conditions [45]. This can be accredited to various factors. First of all, perfectly rigid materials do not exist and upon adhesional failure, real

materials and ice are deformed. Ice in particular has an elastic module that is susceptible to temperature, causing either ductile or brittle deformations and/or fractures [45]. Furthermore, non-planar failures and the formation of micro-cracks also increase the total measured work. Makkonen suggests that the additional, dissipative energy required to separate the surfaces *is* in fact caused by the intermolecular interactions described, and a strong relationship between W_a (equation 2.7) and total work required W_s is still expected.

For the application of an ice adhesion actuator, the adhesion strength and therefore W_a should be maximized, so materials with high surface energies are preferred. Metals are materials with high surface energy, typically in the range 500-2500 mJ/m^2, whereas polymers have much lower surface energy; between 15 - 50 mJ/m^2. However, it is possible to alter the surface energy using treatments, such as coatings, plasma treatment or modifying the roughness of a surface.

2.6.2. Ice Temperature

Elastic Modulus

Ice temperature can greatly influence the adhesion strength of ice, this can be accredited to two factors. First of all, with decreasing ice temperatures, the strength of ice in both tensile (0.7$\sim$3.1 MPa) and compression (5$\sim$25 MPa) increases, with a factor of 1.3 and 4 over a temperature range of 0°C to -40°C, respectively [58]. Ice close to the melting point is more ductile and is less likely to fracture when subjected to high strain rates, in contrary to brittle (colder) ice. However, the fracture toughness of ice shows little dependency on temperature, but shows a small negative relationship with grain size of ice [58]. The connection between the adhesive (ice) and substrate can fail in various modes, the adhesion can break at the ice-substrate interface (adhesion failure), or the connection can fail cohesionally within the ice material (cohesion failure). Additionally, the substrate can fail, these modes are illustrated in figure 2.22. A combination of the described modes are also possible. Once the ice adhesion strength surpasses the cohesion strength of ice, which also depends on the type of loading (tensile, compression or bending), the limiting factor becomes the strength of the ice, and therefore temperature of the ice is an important factor.

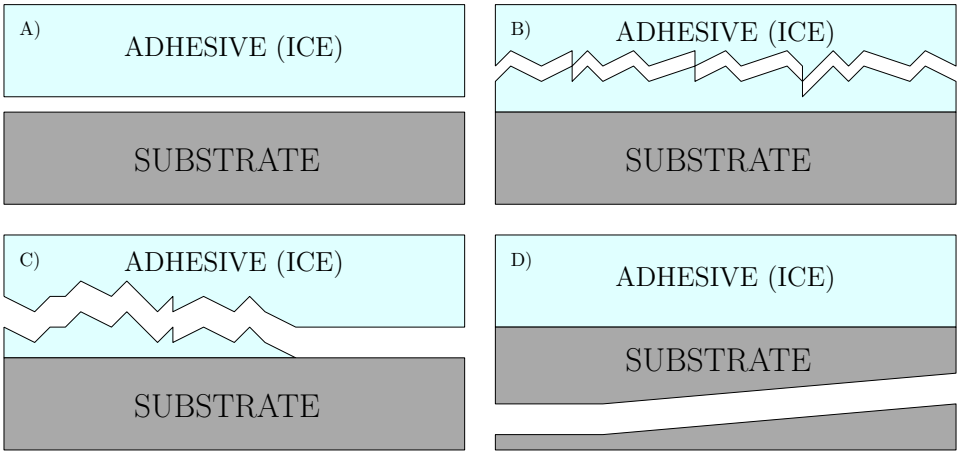

Figure 2.22: Different connection failure modes. A) Adhesive failure. B) Cohesive failure. C) Combination of adhesive and cohesive failure. D) Substrate failure.

Thermal Expansion
Secondly, ice adhesion strength is influenced by the temperature of the ice (and substrate) due to the difference in thermal expansion coefficients [45], for reference, water ice has a thermal expansion coefficient between 53 $\mu strain K^{-1}$ - 49 $\mu strain K^{-1}$ between 0°C and -30°C, respectively. Consider a drop of liquid water on a solid surface, similar to figure 2.21. Both materials have the same initial temperature when the liquid water solidifies to ice. Now with decreasing temperature, both materials will slightly deform, but at different rates given the ice and substrate have different thermal expansion coefficients. This difference will result in an shear force at the ice-substrate interface, effectively reducing the adhesion strength. This is illustrated for various materials in figure 2.23, that shows the adhesion strength as a function of temperature. Here most materials first indicate a slight increase in adhesion strength, followed by a fall in adhesion strength. The exception in this graph is the material Inertia 400, this is a coating that remains elastic even at low(ering) temperatures.

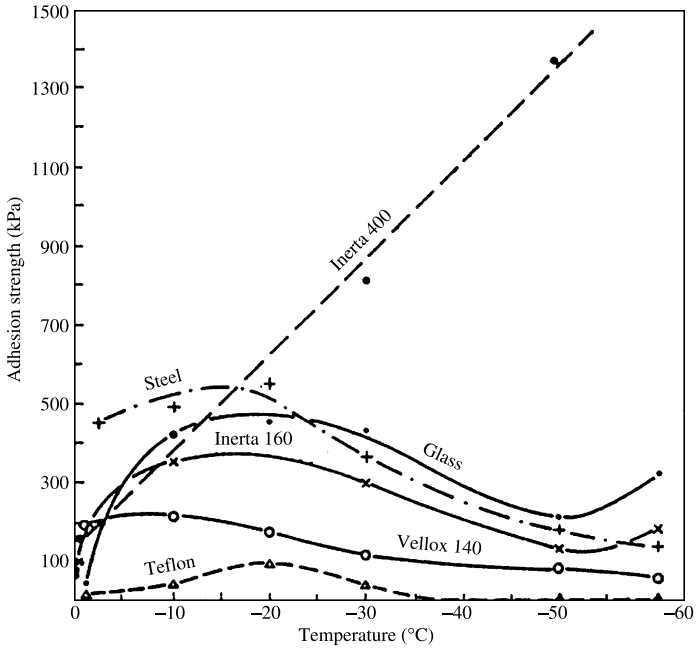

Figure 2.23: Effect of temperature on ice adhesion strength, in shear direction. Image from Makkonen: [45]

2.6.3. Elastic Modulus of Substrate - Deformation (In)compatibility

A well known approach to lowering ice adhesion is to treat surfaces with very soft, silicone like materials; Young's modulus <10 MPa compared to the Young's modulus of ice, 9.7$\sim$11.2 GPa. When subjected to stress, the materials will deform at different rates, creating stress concentrations that can cause local ice detachment from the substrate. If the applied stress is maintained, the detachment can propagate throughout the ice-substrate interface. If the stress applied is an impulse, it is possible for a small pocket of air to form between the ice-substrate interface. These pockets can propagate in the soft material, effectively detaching the ice from the substrate.

2.6.4. Ice Type

RØnneberg et al., 2019 [68] performed experiments to study the effect of ice type on ice adhesion strength. Three different types of ice were used in this study; precipitation ice (hard rime ice), in-cloud ice (impact ice) and bulk water ice (clear ice), illustrated in figure 2.24. The ice adhesion strength to an aluminium substrate was measured using a centrifugal adhesion test at a constant temperature of -10°C. Results indicate highest adhesion strength for precipitation ice (0.78$\pm$0.10 MPa (13.1%)), followed by in-cloud ice (0.53$\pm$0.12 MPa (22.5%)) and lowest adhesion strength for bulk water ice (0.284$\pm$0.083 MPa (28.2%)). It was found that the adhesion strength inversely correlates to the density of the ice. These results support the theory that decreasing grain size increases adhesion strength [58], but other

working mechanisms need to be investigated further.

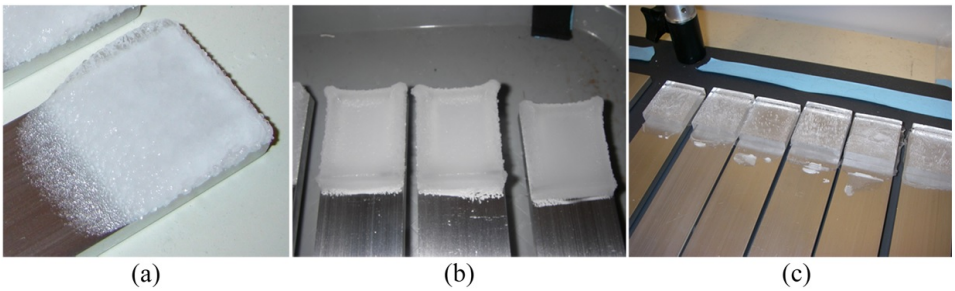

Figure 2.24: Ice types used in [68]. (a) Hard rime ice. (b) Impact Ice. (c) Clear ice. Image credit: Ronneberg et el. 2019 [68]

2.6.5. Surface Roughness - Mechanical Interlocking Effect

Surface roughness is of great significance for ice adhesion strength. Surface texturing is commonly used in combination with low surface energy to impart superhydrophobicity [50], caused by the Cassie-Baxter effect, illustrated in figure 2.25. The effect of (super)hydrophilic and (super)hydrophobic surfaces on ice adhesion strength was studied by Chen et al., 2012 [8]. Four silicon wafer surfaces with groove and pore arrays were created using a photolithographic process. The superhydrophobic and superhydrophilic samples have the same surface topology but are treated with different chemicals to obtain the desired wettability. Smooth surface samples were also created and treated with chemicals to obtain hydrophobic and hydrophilic materials. Results indicate highest adhesion strength for superhydrophilic materials (Wenzel mode), due to the increased surface area and mechanical interlocking effect in the pore structures. Flat and smooth hydrophilic materials show reduced adhesion strength (1/4 of the superhydrophilic material) and lowest adhesion strength was achieved with flat, smooth hydrophobic materials. Superhydrophobic materials, on which water is in Cassie-Baxter state, show similar ice adhesion strengths to superhydrophilic materials. This surprising result is explained by the cooling process of the samples; air trapped in the pockets created by the surface texture is in thermodynamic equilibrium as the liquid water. Lowering temperatures causes condensation and water molecules absorption at the wall of the surface texture, shifting from a Cassie-Baxter mode to more of a Wenzel mode. Water that freezes creates the interlocking effect, increasing the adhesion strength. An important take-away point from this observation is the significant role the interlocking effect plays in the strength of ice adhesion.

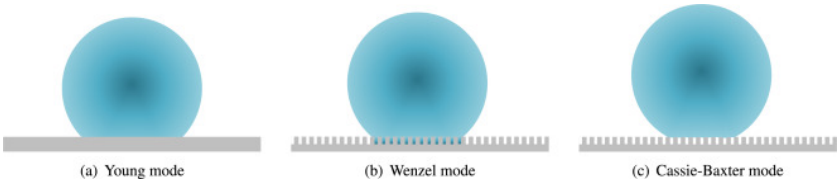

Figure 2.25: Illustrations of different wetting modes of a droplet on flat and rough surfaces: (a) Young mode; (b) Wenzel mode; (c) Cassie–Baxter mode. Image from [16]

2.7. Conclusion

Reviewing the (known) conditions *on* and *in* Enceladus reveals some of the complexities involved with the development of a robotic system capable of exploring the icy moon. However, the abundance of water ice and cold temperatures inspired this project to turn the challenges into opportunities; make use of the environment to enable transportation.

Before any of the proposed mission concepts would be able to reach the liquid water on Enceladus, more information is required about the moon. While there is a wide variety of proposed missions, the systems who wish to exploit the existing cracks in the ice are still in very early development. Researching new methods to scale icy surfaces is therefore most relevant to facilitate those mission.

The relevance of new ice climbing technologies is again confirmed when reviewing the state-of-the-art in ice climbing robots, as there is only one record of such system.

Ice adhesion as a means of manipulating objects or creating reversible connections has been adopted in the development of ice grippers that are capable of seizing and manipulating textile or micro-sized objects in aqueous state. Nevertheless, ice adhesion as a locomotion strategy is an unexplored concept.

Two main methods to effectuate the phase change of water (solid-liquid) have been identified and discussed. From those methods, the thermoelectric effect is selected to be used in this project due to the ease of fabrication, simple structure, lack of moving components, availability and ease of operation.

Lastly, ice adhesion mechanics are discussed, from which important material properties can be derived for the material selection process.

3

Thermoelectric Cooling System & Ice Adhesion Effector

Introduction
This section elaborates on the design considerations and part selection for a thermoelectric cooling an heating system. In particular, the considerations for the thermoelectric cooling system that is used to evaluate the performance of the adhesion effector in terms of adhesion strength and temperature response.

3.1. Peltier Module Selection

Typically, peltier modules are selected using the performance curves of the thermoelectric modules, using the desired temperature difference across the hot and cold side of the module $\Delta T = T_H - T_C$ and required heat flux Q from the object to be cooled. Even with this method, the selection process is not so trivial, since it is difficult to accurately obtain the heat flow to the surroundings.

For the application of a switchable ice adhesion effector, the exact peltier element specifications are less critical, since the required heat flux is close to zero, once the effector is adhered to the icy surface. Therefore, the governing heat flow is the energy that needs to be dissipated from the 'adhesion pad', to reach freezing temperatures. This presents a trade-off; high power peltier elements will cool the adhesion pad more rapidly than low power peltier elements, at the cost of higher energy consumption. Meanwhile, both high and low power peltier elements can reach similar temperatures; the temperature difference ΔT is mostly determined by the input power respective to the maximum input power of the element.

Peltier modules come in all sort of shapes and sizes, but often they are specified by the following format: TEXX-XXXXX. For example: TEC1-12706, where 'TE' indicates Thermo Electric and are always the same, 'C' indicates *cooler* and is sometimes interchanged with 'S' which denotes a smaller size. Next, '1' indicates that it is a single stage module. Furthermore, '127' means there are 127 P- and N-doped semiconductor couples, thus, a total of 254 pellets. Lastly, '06' means the maximum current is 6 A. The TEC1-12706 module is 40 x 40 x 3 mm in size. This is the most common size for modules with 127 semiconductor couples. Elements with these dimensions typically range from 35 to 180 Watts.

Coincidentally, the TEC1-12706 peltier element is selected for the development of the first prototype of the switchable ice adhesion effector. With a maximum heat flux of 66 W, the power requirements are easily met with the power supply units that are available. This element is selected because heat flux is not prioritized, and it can be easily interfaced with off-the-shelf computer heat dissipation systems, which are similar in dimension.

3.1.1. Thermal Schematic of Thermoeletric Cooling

To illustrate the heat flow in a thermoelectric cooling system, a thermal schematic can be used. A thermal schematic follows the thermal-electrical analogy, as shown in figure 3.1a. From top to bottom, this figure shows: the ice to which the actuator will adhere, the ice is considered to have constant temperature T_∞. The adhesion pad adhered to the ice, since liquid water will eliminate all the voids in the ice-adhesion pad interface, the thermal contact conductance is ignored. The thermal resistivity of the adhesion pad is given by $R_{th,AdhesionPad} = L_1 k_1^{-1} A^{-1}$. The surfaces of the adhesion pad and peltier device are not in direct contact with one another, since this would introduce a thermal contact resistance, as a result from microscopic surface irregularities. Instead, a thermal interface material (TIM) should be used to increase the thermal coupling between materials. Examples of TIMs are (but not limited to): thermal paste, thermal adhesive, thermally conductive pads or phase change materials. The thermal resistivity of the TIM is constructed in similar analogy to the thermal resistivity of the adhesion pad. While the peltier module is simplified and shown as a single, homogeneous material, in reality the peltier is constructed from different layers and materials, as discussed and illustrated in figure 2.17b. An in depth thermoelectric model can be found in the research performed by Ezzahri & Shakouri, 2008 [19]. The peltier module and heatsink are again connected via a TIM. Essentially, the heat sink will dissipate the heat accumulating (pumped and I^2R losses) on the hot side of the peltier module. The performance, or thermal resistivity of the heat sink $R_{th,heatsink}$ depends on the materials used, volume and geometric shape. In turn, the heat sink dissipates the thermal energy to the surroundings; the thermal resistivity of this heat flux is denoted by $R_{th,heatrejector}$, either via a liquid or gas medium.

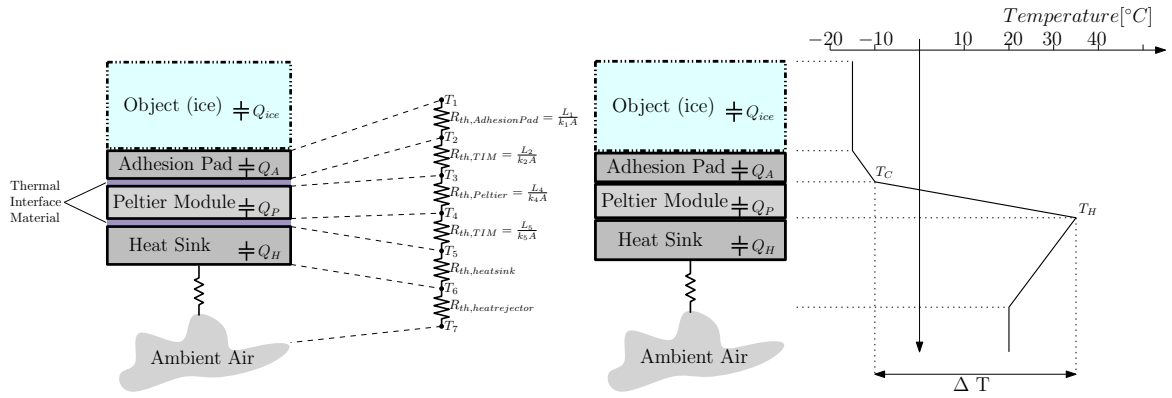

(a) Thermal schematic of thermoelectric cooling and heating system as switchable adhesion actuator (simplified).

(b) Simplified schematic of a thermoelectric cooling and heating system with corresponding temperature diagram.

Figure 3.1: Thermal schematics of the peltier element implementation.

To illustrate the heat flow in the system, the system is further simplified to the resulting schematic shown in figure 3.1b. The estimated corresponding temperature of in the system is shown in the right diagram. The thermal interface materials are removed from this schematic, considering that the thickness of the TIMs are in micrometer scale; their contribution is neglected. This figure depicts the a thermoelectric setup that is actively cooling the adhesion pad, with the ice having a constant temperature. It is important to note that the ΔT of the peltier module is between the cold side T_C and hot side T_H of the peltier, and that T_H is higher than the ambient temperature. To reach, and sustain sufficient sub-zero temperatures on the cold side of the peltier module, it is important to choose an appropriate heat sink, considering that ΔT is limited to 70 K for most commercially available peltier modules, in ideal conditions. In reality, a more realistic temperature difference is around 50 K, since the performance of peltier modules decreases with decreasing temperatures.

3.1.2. Peltier Perfomance Curves

The performance curves of the TEC1-12706 module are shown in figure 3.2, the charts are obtained from the information supplied by the manufacturer: Tru Components. This graph shows the performance curves in two scenarios, on the left the performance curves are shown for a peltier hot side temperature of 27°C. The right graphs show the same performance curves but in scenarios where the hot side temperature is 50°C. The top graphs shows the heat flow rate from the cold side $\dot{Q}_C$ in Watts, as a function of ΔT in °C, at constant input currents as indicated in the graph legend. In these graphs, it is clear that the rate of heat flow $\dot{Q}_C$ is highest for $\Delta T = 0$, this means that the heat load (object to be cooled), is equal to the heat absorbed by the peltier module. Since the heat flow rate is negatively proportional to the ΔT, the heat absorption $\dot{Q}_C$ is zero for maximum ΔT. The middle graphs show the voltage over the peltier module as a function of ΔT, at constant current. This graph could be used to find the operating voltage when designing a thermoelectric cooler with constant voltage supply as a control system. Additionally this graph shows that the voltage increases with increasing ΔT at constant voltage, subsequently, the total power consumption increases while the absorbed heat flow rate $\dot{Q}_C$ decreases. This effect is also visible in the bottom graphs, which shows the absorbed heat flow rate $\dot{Q}_C$ as a function of the voltage, at constant ΔT.

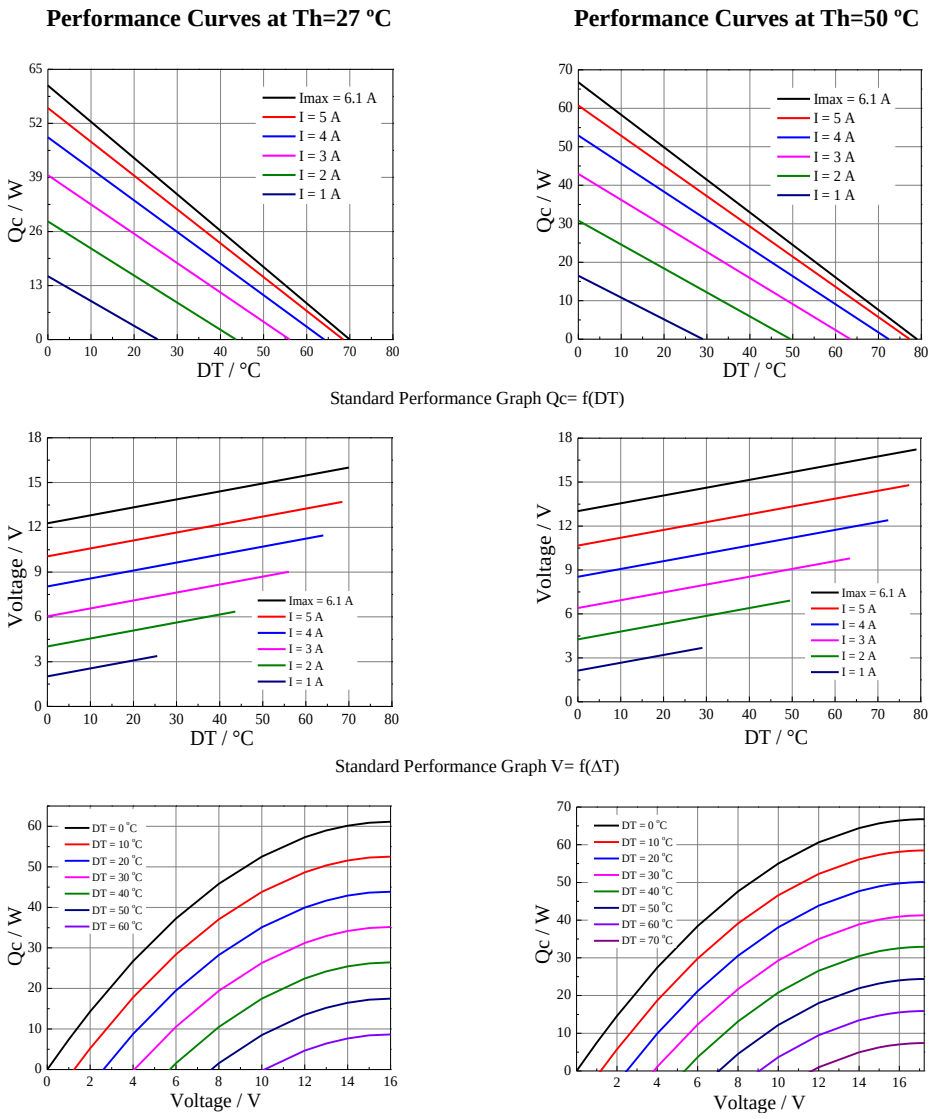

Figure 3.2: Performance curves of a TEC1-12706 peltier module. From datasheet of manufacturer: *Tru Components*

3.1.3. Heat Load

For the application of a switchable ice adhesion effector, the peltier element is used for thermal cycling; switching between between heating *and* cooling, rather than constant cooling. The heat load can be estimated from the thermal capacity of the adhesion substrate (adhesion pad), considering that the ice is already at constant, sub-zero temperature. Using this thermal capacity and desired time-to-adhere, a heat load can be estimated. However, this approach requires the specific heat capacity of the adhesion pad material. For now, aluminium is taken as design choice, chapter 4 elaborates on the material selection procedure for ice adhesion substrate materials. The energy required to change the temperature of a solid aluminum (density $\rho = 2710kgm^{-1}$, specific heat capacity $c_p = 913Jkg^{-1}K^{-1}$) block 40x40x10 mm in size in size from 20°C to -15°C, a temperature difference ΔT_A of -35 K, is given by:

$$Q_{freeze} = V\rho c_p \Delta T_A \tag{3.1}$$

Here, V denotes the volume of the block. It then follows that the energy required is equal to -989 J. The top left graph of figure 3.2 can be used to find the cooling rate of the peltier in these conditions, these graphs represent a constant hot side temperature of 27°C. The maximum amperage of 6.1 A is used in this example to determine the time required to cool the aluminium solid. Starting at a room temperature of 20°C, the temperature difference ΔT between T_H and T_C is 7°C, considering a constant hot side temperature T_H of 27°C. The temperature difference when the adhesion pad is at a desired temperature of -15°C, is 42°C. The corresponding cooling capacities derived from the top left graph of figure 3.2 are 55 W and 24 W, respectively. The average cooling capacity of this linear regression is therefore $0.5(55 + 24) = 39.5W$. Then using this average cooling capacity, the time required for this peltier module to chill the aluminium block down to -15°C is equal to $989/39.5 = 25s$. This however, is in ideal conditions, where the aluminium block is perfectly insulated from the outside, and not effected by any convective or radiative heat transfers. Additionally, it assumes a constant hot side temperature of the peltier T_H of 27°C. The importance of a proper heat sink is becomes apparent when a hot side temperature of the peltier T_H of 50°C is used (from the top right graph in figure 3.2), in similar analogy to previous example, the time required to chill the aluminium block becomes 38 s. Important to realize is that in these examples, the heat flow from aluminium block to the icy surface is neglected. Since the ice is already at a sub-zero temperature, it will extract a portion of the heat from the aluminium block, reducing the time required to reach the desired temperature significantly.

3.2. Power Supply and Control

Power Supply

Since a current proportional heat flow leads to a temperature difference, peltier modules are most easily controlled using a constant current (CC) power source. Constant voltage (CV) sources are also suitable solutions. For accurate control, a feedback system with temperature sensors is advised. Driving a peltier module with a PWM voltage is not recommended, as the peltier efficiency will dramatically decrease, making it unable to reach large temperature differences ΔT and the life span shortened. For this project, a Delta Elektronika ES 030-5 power supply unit (PSU) is used. This PSU can supply a voltage between 0-30 V with a current between 0-5 A, and can be controlled via analog input at the front of the device. Alternatively, external interface modules can be connected that allows full control of the device via external software.

Controlling Melt and Freeze Time

Since the cooling/heating surface of peltier modules are easily reversed by switching the polarity of the power supply, a basic control system can be designed to enforce the desired melt and freeze times during the ice adhesion experiments described in chapter 5. This control system is made up from electro-mechanical relays that are wired in an H-bridge configuration. An H-bridge is an electrical circuit that can change the direction of current passing through a load by switching its polarity, as illustrated in figure 3.3, commonly used to control the direction of rotation of electric motors. While there is a wide variety of H-bridge circuits, from dedicated integrated circuits (IC), to mechanical switches; electro-mechanical relays are selected to build the H-bridge circuit. These relays are cost effective, easily controlled and capable of handling the loads applied to the peltier (max 15V, 5A), but do not provide the most compact solution, however.

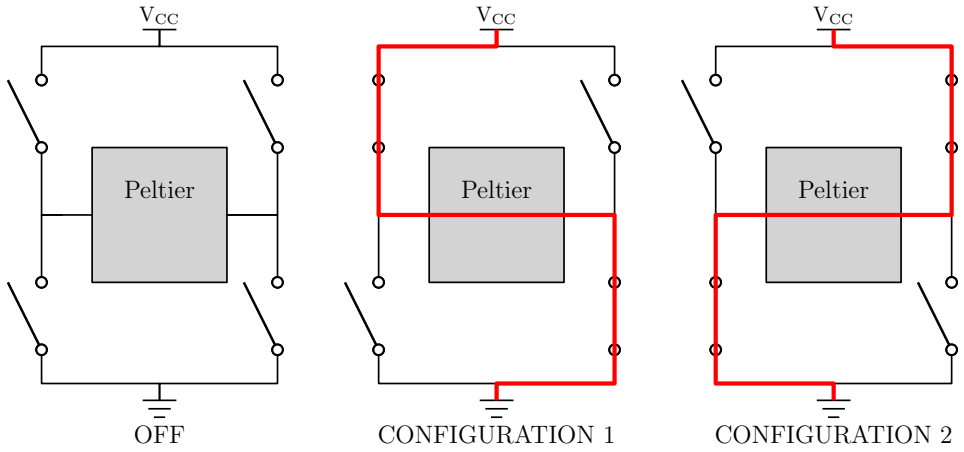

Figure 3.3: Schematic overview of H-Bridge circuits.

An Arduino Nano microntrollerboard is programmed to switch the H-Bridge circuit according to a pre-defined timer sequence. Before activating the sequence, the 'normal' state of the controller is the cooling configuration. This is to ensure the same adhesion pad starting temperature before the sequence is initiated, and allows the adhesion pad to contact the ice before the experiment is started, since both the substrate and adhesive are at sub-zero temperatures; no melting will occur. Once activated, the sequence is as follows:

1. Rest for 10 s, no power to peltier
2. Heat for 25 s
3. Rest for 10 s, no power to peltier
4. Cool indefinitely; buzzer sounds after 80 s to initiate test

Rest periods are added in the sequence to avoid rapid switching of the peltier module, which can cause damage. The components are fitted in a small enclosure manufactured using the Elegoo Saturn mSLA printer, see figure 3.4. The toggle switch on the enclosure sets the actions performed by the controller; 'cooling', 'off', and 'test sequence'. The momentary switch can manually activate the heating configuration when depressed, given that the toggle switch is in the 'off' position. When the 'test sequence' is selected, the peltier will be switched to the cooling configuration, until the sequence is initiated. In fact, the controller is signalled by the temperature logger; initiating the data logging to SD card will signal the peltier controller to start the sequence.

Figure 3.4: H-bridge peltier controller box.

3.3. Heat Dissipation System

The heat sink is an critical element of the thermo-electric cooling setup, as it dictates the temperature difference the peltier modules can obtain. The purpose of the heat sink is to dissipate the heat that accumulates at the hot side of the peltier module; heat flow from the cold side to the hot side, and internal I^2R losses of the peltier. Heat sinks can (generally) be divided into two categories, passive or active cooling. Passive heat sink systems rely on natural convection while active heat sink systems make use of forced convection. This project selects the method of an active, liquid heat exchanger as they prove to be most effective in cooling the hot side of the peltier element, as mentioned in the work by Riffat [66]. TEC1-12706 peltier elements have a 40 x 40 mm contact area, which is similar to desktop computer processor chips (CPUs). The heat outputs of CPUs are compareable to peltier elements (50-150 W) and like peltier elements, proper cooling of CPU chips is essential to avoid performance degradation. Thus, off the shelf CPU cooling components are used in this project to construct the heat dissipation for the thermo-electric cooling setup. Figure 3.5b shows a schematic overview of the liquid cooling components and fittings. Then, the actual system is shown in figure 3.5b

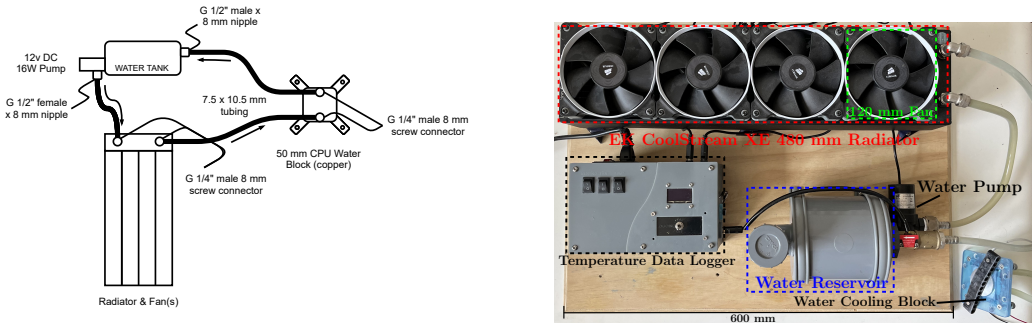

(a) Schematic overview of the water cooling loop.

(b) Water cooling loop for cooling the peltier module.

Figure 3.5: Liquid cooling system used to dissipate heat generated by the peltier element.

This system works as follows: water in the reservoir is pumped through the water radiator. Warm water dissipates heat to the thin, copper fins in the radiator, heating the air between the fins through radiative and convective heat transfer. Electric fans are placed on top of the radiator, these fans displace air between the copper fins. Consequently, water passing through the radiator is cooled towards ambient temperatures. Cooled water then flows to the water cooling block. The water cooling block is mounted to the hot side of the peltier; absorbing the waste heat and transferring the heat to the water flowing through the water cooling block. Water passing the water cooling block is therefore heated and flows back into the reservoir, completing the loop.

Radiator Cooling Capacity

Cooling capacity of a water cooling radiator is determined by multiple factors: thermal properties of the radiator (material type, fin density, flow restriction, etc.), water flow rate, air flow rate (dependent on fan speed), temperature difference between liquid and ambient air. Quantifying the cooling capacity therefore is difficult. In the setup presented here, an EK-CoolStream XE 480 radiator is used in combination with four 120 mm fans, this radiator is commonly used in systems with heat outputs up to 1000 W; providing plentiful cooling capacity for a single TEC1-12706 peltier element with a rated output of 65 W. This radiator is used since it was already available, but can provide a robust heat dissipation solution for future work.

3.3.1. Recording Temperature Data

Temperature measurements are crucial to evaluate the performance of the thermoelectric cooling setup, and to explore the difference in material properties for ice adhesion substrate materials at later stages of the research. The digital Dallas DS18B20 sensor is selected for this purpose for multiple reasons. First of all, the temperature range of this sensor is -55°C to 125°C, making it a suitable choice to measure temperatures in the same temperature range of peltier modules. Unlike thermocouples, which require additional amplifiers to convert a voltage, these sensors do not

require any external components to function and can connected to a microcontroller or other device to record temperatures via a single wire. The sensor's resolution can be set to 9,10,11 or 12 bits (12 bit resolution has a precision of 0.0625°C), the accuracy of these sensors is ±0.5°C and can be powered from an external power supply with a voltage between 3.0 to 5.5 V. The 1-Wire interface means that multiple sensors can be connected to only one port pin for communication. To read and collect the temperature measurements, an Arduino Nano is programmed to read the connected sensors and display the data on a small lcd screen. The addition of a SD card module allows the measurements to be stored. These components are fitted in a 3D printed enclosure. This enclosure houses additional components for the thermoelectric cooling setup; a 240 to 12V AC/DC power supply to provide power to the Arduino, water pump and fans, two buck-boost (step up-down) DC-DC converters that allow the pump and fan speed to be adjusted, and a SD-card module. As well as some additional components such as switches, LCD screen for reading the measured temperatures, cooling fan for heat dissipation, and some connectors to connect the sensors. This enclosure is shown in figure 3.6 and is part of the thermo-electric cooling setup shown in figure 3.5b. As seen in figure 3.6, up to five sensors can be connected to the data logger with standard 3.5 mm jack connectors.

Figure 3.6: Temperature data logger. Part of the thermo-electric cooling setup shown in figure 3.5b.

3.4. Ice Adhesion Effector

The ice adhesion effector essentially combines all components described in this chapter to create an apparatus that can be used to test the temperature response of various substrate materials and most importantly, the ice adhesion strength. Figure 3.7 shows the cad model of the effector. This model

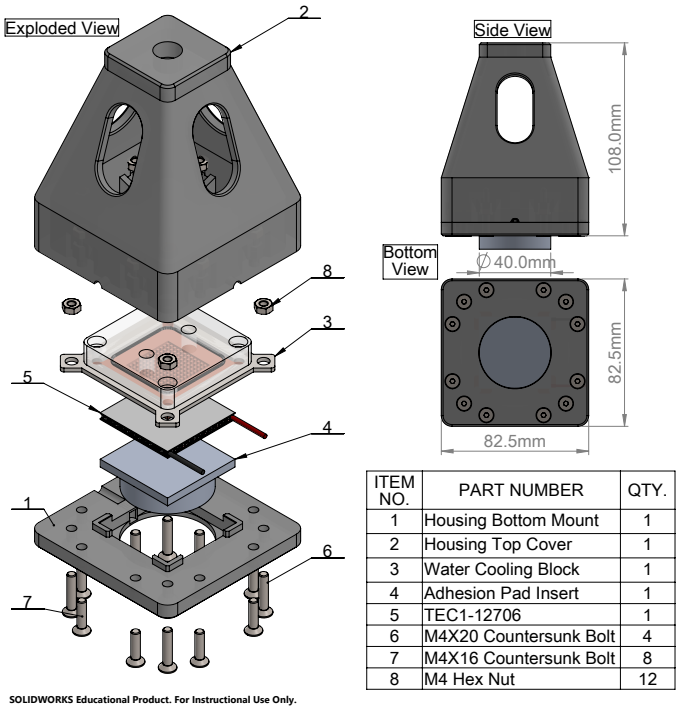

ITEM NO.	PART NUMBER	QTY.
1	Housing Bottom Mount	1
2	Housing Top Cover	1
3	Water Cooling Block	1
4	Adhesion Pad Insert	1
5	TEC1-12706	1
6	M4X20 Countersunk Bolt	4
7	M4X16 Countersunk Bolt	8
8	M4 Hex Nut	12

Figure 3.7: CAD Model of the ice adhesion effector assembly.

introduces three parts that need to be fabricated; the 'effector bottom mount', 'effector top cover' and the 'adhesion pad insert'. The effector bottom mount functions as a mounting plate for the adhesion pad, on which the peltier module is sandwiched by the water cooling block. The water cooling block is secured to the effector bottom mount with bolts and can be tensioned with springs; see figure 3.8.

The effector top cover is also secured to the effector bottom mount using eight M4 countersunk screws. The effector top cover has a large hole in the top that accepts a bolt (M10-M12) to mount the effector in testing equipment, the body of this cover will transfer the loads from the tensile pull-off testing machine to the effector bottom mount, in which the adhesion pad is seated.

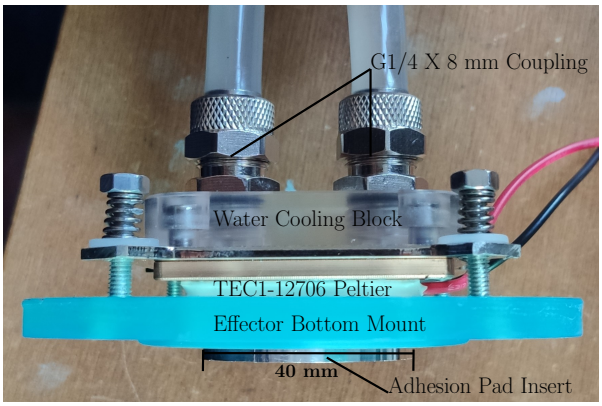

Figure 3.8: Effector bottom mount assembly with water cooling block, TEC1-12706 peltier element and adhesion pad insert

Adhesion Pad

The adhesion pad is cooled or heated by the TEC1-12706 peltier elements. To make optimal use of the cooling capacity of the element, the surface area and contour of the adhesion pad match that of the peltier module. The TEC1-12706 modules are 40x40x3.8 mm in size, so the adhesion pad insert has a matching 40x40 mm square surface contacting the peltier element. The surface contacting the ice should be free of sharp corners to avoid stress concentrations during the pull-off tests, causing high variability in results [87].

Additionally, since the peltier modules are constructed from two ceramic plates, sandwiching the semiconductor pairs, applying loads on the ceramic plates should be avoided, as they are sensitive to brittle fractures. Therefore the load required for the pull-off tensile adhesion test should be applied solely to the adhesion pads, thus the pads require features to which these forces can be applied. When choosing to create a circular contour for the surface contacting the ice, stress concentrations are avoided. Adding a sharp transition from round to square, while the diameter of the circle matches the overall dimension of the square (d = 40 mm), creates four 'shoulders' which can be used to apply the load during the tests; preventing the testing load being applied on the peltier module. This creates a very minimalistic design that can be produced with basic mill and lathe operation, the CAD model of the adhesion pads is shown in figure 3.9.

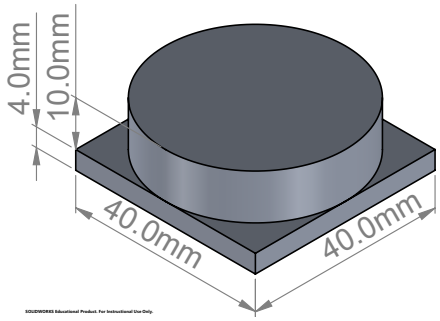

Figure 3.9: CAD model of the adhesion pad insert.

The height dimensions of the adhesion pad is set to ensure the adhesion pad protrudes 6.5 mm below the adhesion effector bottom mount. This creates adequate clearance between the ice and adhesion effector bottom mount, and prevents any liquid water from contacting the bottom mount (preparatory ice adhesion strength tests suggested that this should be avoided, more information in appendix A.

Materials and production
Both the effector bottom mount and top cover are complex parts, which are difficult to produce using subtractive manufacturing processes, but are well suited for additive manufacturing processes (3D printing). These parts are produced with a modified Elegoo Saturn 4K MSLA (masked stereolithography) printer, these printers employ the photopolymerization process to selectively harden resin, creating very thin layers that build up the desired shape. Siraya Tech Blu-Tough resin material is used to produce the effector bottom mount and effector top cover. The materials used for the adhesion pad inserts is discussed in chapter 4.

3.5. Experiments

The experiments described in this section are performed to test the thermo-electric cooling system, and see if the system is capable of reaching the temperatures required for establishing ice adhesion between a substrate material and ice. Additionally, effects such as peltier element quality, input current, heat dissipation methods and water flow are tested. The results of these tests can aid in the development of robotic systems.

3.5.1. Peltier quality

The experiments shown in this section illustrate the difference in peltier element quality, comparing generic to name-brand elements in terms of temperature response, temperature range and power consumption. Two elements are generic (no brand) TEC1-12706 elements, the third module is also a TEC1-12706 module, but instead manufactured by Tru Components. The hot side of the peltier modules are interfaced with the copper water cooling block with ProlimaTech PK-2 thermal compound. A temperature sensors is placed and secured on the ceramic, cold side of the peltier, as shown in figure 3.10.

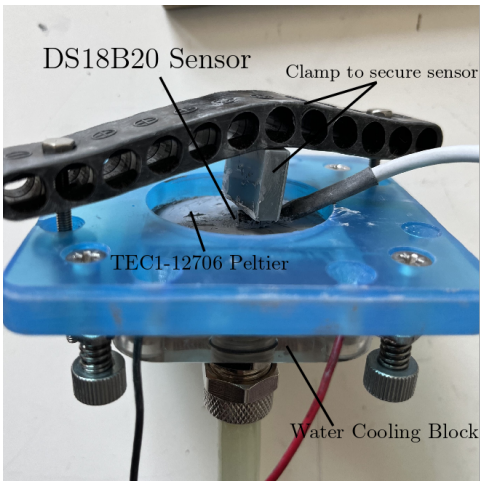

Figure 3.10: DS18B20 sensors placed on a TEC1-12706 peltier module.

A constant current of 3 A is applied to all peltier modules, in an environment with ambient air temperature of 18°C. The left chart of figure 3.11 shows peltier cold side temperature for during the test for a total duration of 120 seconds. All peltier modules are at room temperature with no power supplied to the module before the test. Power is supplied to the modules at t = 0 s, and the power consumption during the test is recorded, shown in the right chart of figure 3.11.

Indeed, the difference between the peltier modules is significant for both the temperature and power consumption. The TRU COMPONENTS peltier module is able to reach a temperature of -25°C at the end of the test, while the power consumption is the lowest of all tested peltier modules (24 W). Power consumption of 'generic-2 TEC1-12706' is similar, yet higher than the name brand peltier module. In conclusion, the TRU COMPONENTS TEC1-12706 is used throughout the course of this research.

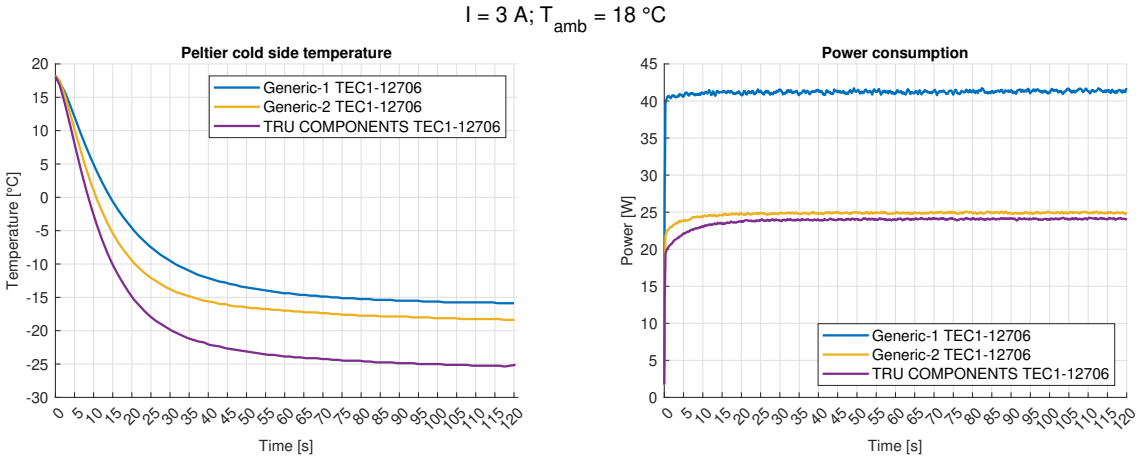

Figure 3.11: Peltier cold side temperature response (left) and power consumption (right) for three TEC1-12706 peltier modules

3.5.2. Input current

The effect of input current is evaluated by measuring the peltier cold side temperature and power consumption at different input currents. Here, the current is increased from 1 A to 5 A with 1 A increments. While the peltier has a maximum input current of 6.1 A, the peltier is only tested with a maximum input current of 5 A, due to power supply limitations (5 A). The cold side temperature is shown in the left chart of 3.12, the right chart shows the corresponding power consumption.

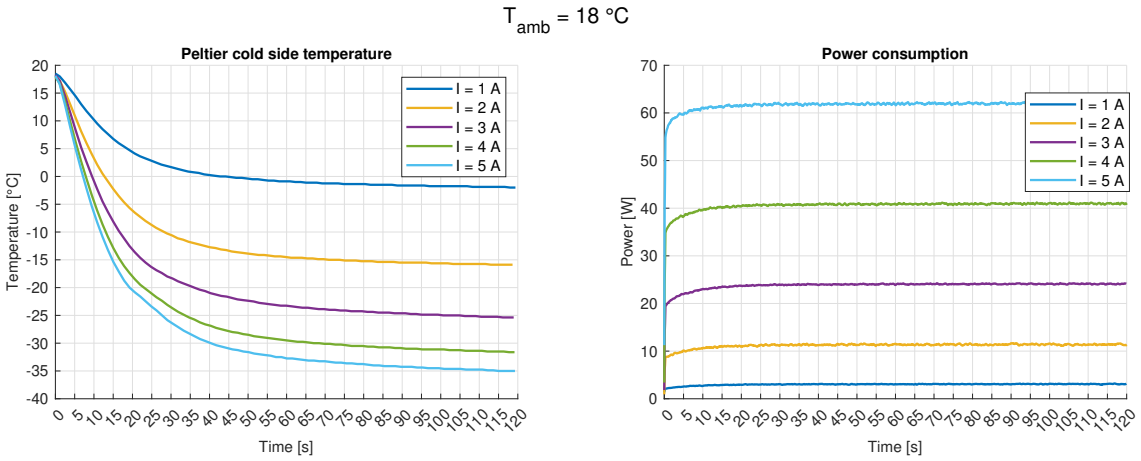

Figure 3.12: Peltier cold side temperature response (left) and power consumption (right) for different input currents.

As expected, the lowest temperature (-35°C) is obtained with the highest input current I = 5 A. However, the minimum temperatures do not appear to show a proportional relation to the input current; the difference in temperatures decreases for increasing input current. This effect is expected, since the performance curves in figure 3.2 do not indicate a proportional relation between input current and maximum temperature difference ΔT: 25°C, 43°C, 55°C, 64°C and 67°C for input currents 1-5 A with 1 A increments, respectively. This is an effect of the increased I^2R losses at higher currents. Consequently, the difference in power consumption increases for increasing input currents. This illustrates the effect of the internal I^2R heat generation; the *ratio* of heat pumped from the cold side and heat from internal resistance, combined making up the total heat rejected at the hot side of the peltier, becomes smaller. So while the total heat rejected at the hot side of the peltier increases, the increase in cooling performance is only marginal for higher input currents.

3.5.3. Effect of water flow

So far, the tests have been performed with the water pump operating at full capacity, providing a water flow of roughly 2 l/min to the water cooling block, which dissipates the heat from the hot side of the peltier module. Until now, the measurements of the peltier module were performed without any heat load; the temperature sensor was attached directly to the cold side of the peltier module. Here, a small 'heat load' is added to this surface in the form of a aluminium block. This aluminium block is 15 x 20 x 6 mm in dimension and made from 6061 aluminium. This heat load is selected per design choice, and only acts as a small heat load to evaluate the cooling capacity at different water flow rates through the water cooling block; material properties and dimensions of the heat load are not critical. The temperature sensor is now placed on the outer surface of the heat load. Here, five tests are performed with a constant current of 3 A supplied to the peltier module at t = 0 s, ambient temperature is 18°C for all tests. The tested water flow rates are: 0, 0.1, 0.5, 1.0 and 2.0 l/min, the water flow is verified by measuring the volume of water pumped in two minutes, before each test. The measured temperature of the aluminium block at different water flow rates is shown in figure 3.13.

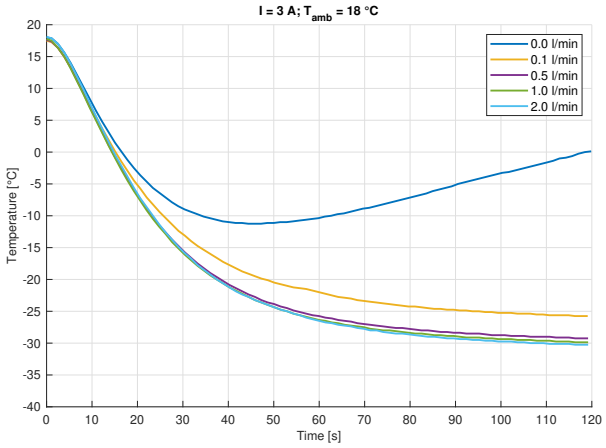

Figure 3.13: Effect of water flow on cooling capacity of peltier module.

Interestingly, the temperatures follow a similar trajectory for the first 10 seconds, then the test with no water flow (0.0 l/min) is cooling at a lower rate then the other tests. After 45 seconds, the temperature of the no-flow test starts to climb and reaches 0°C at the end of the test. The thermal mass of the water cooling block and water in the block allows the peltier to cool the heat load to sub-zero temperature initially. Only after the water cooling block is saturated with heat, the hot side of the peltier rises to the point where it is impossible to sustain sub-zero temperatures at the cold side of the peltier. Now, providing only a very limited water flow to the water cooling block (0.1 l/min), it is possible to cool, and sustain cold temperatures of the aluminium block. Further increasing the water flow improves the cooling capacity of the system, but increasing water flow above 0.5 l/min does not show a significant difference.

3.5.4. Active vs. passive heat dissipation

The water cooling loop provides a reliable method to dissipate heat from the hot side of the peltier module and thus enables the peltier to reach temperatures well below the freezing point. However, for the proposed application of small scale robotic systems, temperatures down to -35°C might not be required. Therefore the options of compact, passive heat sinks is briefly explored and tested. In this test, the peltier hot side is cooled with three different methods. First, the water cooling loop as designed in this chapter. For the second test, the water cooling block is replaced with a passive aluminium heat sink, as shown in figure 3.14. Lastly, a 60 mm 12 VDC fan is positioned on top of the passive heatsink, creating a forced air convective heat transfer from the heat sink fins to the surroundings. The test is initially performed with a constant input current of 1.5 A, with an ambient air temperature of 18°C. Again, the small heat load is added on the cold side of the peltier module. The left charts of 3.15 show the

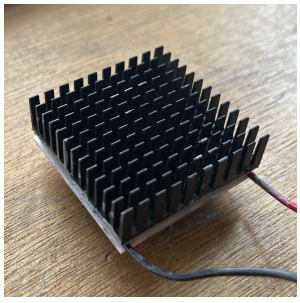

Figure 3.14: Peltier with passive heatsink.

measured temperature (top) of the aluminium block acting as heat load, the bottom left chart shows the corresponding power consumption. The tests are repeated with an input current of 3 A, as shown in the two right charts of 3.15. The passive heat sink is not tested here to prevent overheating of the peltier module.

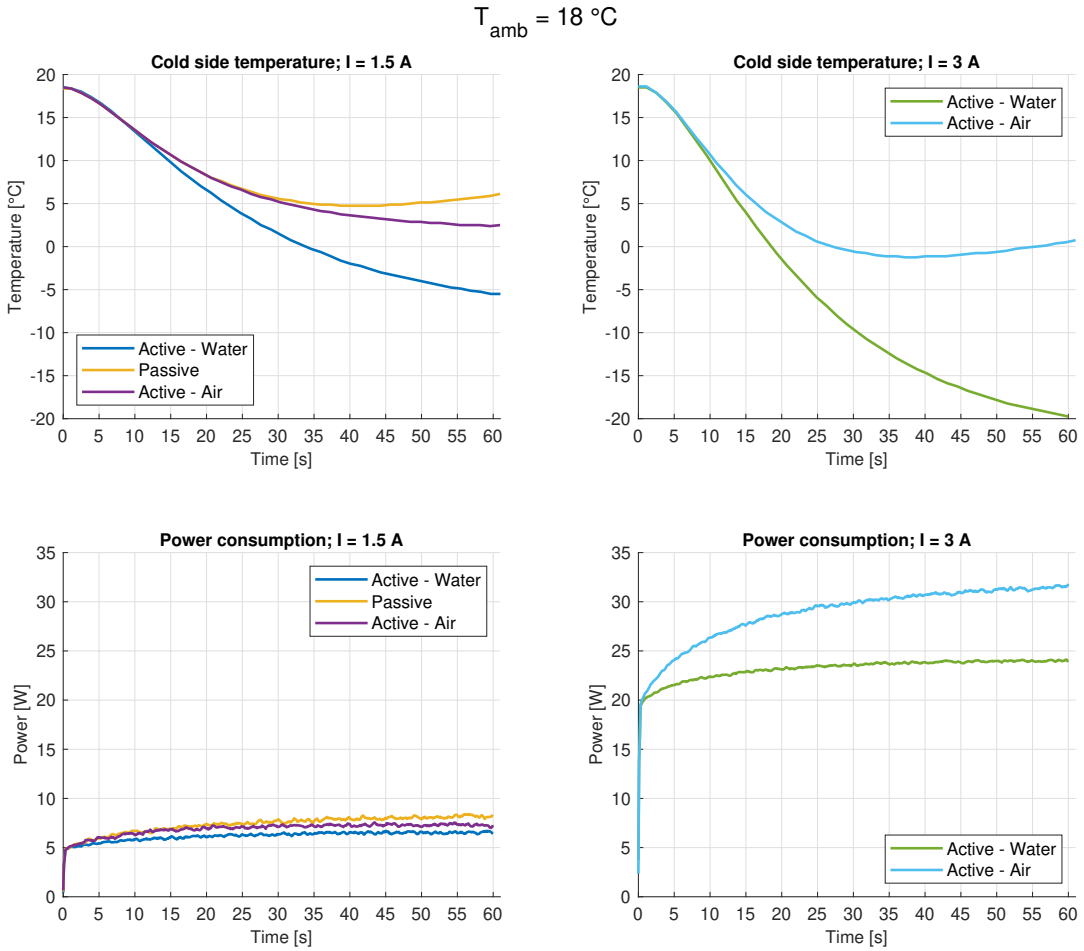

Figure 3.15: Peltier cold side temperature response (top) and power consumption (bottom) for different heat dissipation methods.

During the tests performed here, only the water cooling loop is able to provide sufficient cooling to the peltier module to sustain sub-zero temperatures. Inspecting the power consumption shows that the liquid cooling system requires the least amount of power. During the test with I = 1.5 A, the *Active - Air* graph shows a power increase of $\sim$%14 over the *Active - Water*. Meanwhile, the *Passive* curve shows an increase of $\sim$29% in power. The differences in power consumption become more apparent when inspecting the graph for I = 3 A; here the *Active - Air* curve shows an increase of $\sim$30% compared to the *Active - Water* curve. Conclusively, these tests confirm that a liquid cooling system is the preferred method for dissipating heat from the peltier element in the ice adhesion effector, as this method results in the lowest temperature at the cold side of the peltier, with highest reliability.

3.6. Conclusion

In this chapter, a thermo-electric heating and cooling system is developed. In combination with the adhesion effector, this system will be used to quantify the ice adhesion strength of various materials and surface treatments. The materials and surface treatments will be selected in the next chapter 4.

Demonstrations of the thermo-electric heating and cooling system have shown that the system is able to quickly change temperature and reach temperatures well below zero. Proving that the thermo-electric effect is a suitable method for a switchable ice adhesion effector. It is also found that the quality of peltier elements can vary widely.

4

Substrate Material Selection for Ice Adhesion Effector

4.1. Introduction

This chapter describes the material selection process for the ice adhesion substrate material. Material properties from the literature review on ice adhesion mechanics are used in combination with additional properties described here. Materials selected in this process are used to produce the adhesion pad inserts described in chapter 3, these adhesion pad inserts receive three different surface treatments and are used in the ice adhesion strength experiments described in chapter 5.

4.2. Substrate Material Properties

This section lists, and briefly describes the material properties used in the material selection procedure.

4.2.1. Properties for Ice Adhesion Strength

Section 2.6 of chapter 2 describes the ice adhesion mechanics. Substrate material properties that impact the ice adhesion strength can be derived from the ice adhesion mechanics. These properties are *briefly* discussed in this section.

Surface Energy

The surface free energy quantifies the energy needed to disrupt these intermolecular forces and create new surface area. It is usually expressed in units of energy per unit area, such as joules per square meter (J/m^2), dynes per centimeter (dyn/cm) or Newton per meter (N/m). A strong relationship between surface energy and adhesion strength is expected [45]. Substrate materials with high surface energy are therefore preferred, these materials often include metals or ceramics. Plastics are typically considered low surface energy materials.

Elastic Modulus

Materials with high stiffness (Young's modulus E often expressed in MPa) are preferred since these exhibit little deformation when subjected to high loads. Substrate material seized to ice that have high strain rates will create stress concentrations at the substrate-ice interface, which is detrimental for the strength of the adhesive connection.

Thermal Expansion Coefficient

Pure water ice has a thermal expansion coefficient between 53 $\mu strain K^{-1}$ - 49 $\mu strain K^{-1}$ between 0°C and -30°C, respectively. Substrate materials with similar thermal expansion coefficients are favored, as it limits the interfacial stresses resulting from the difference in strain rates at decreasing temperatures.

4.2.2. Thermal Properties

The adhesion pad substrate material will be heated and cooled by the peltier element and thus experiences frequent thermal cycling. By selecting materials with desirable thermal properties, the required energy and time for changing the temperature of the adhesion pad can be minimized. These thermal properties are described in this section.

Thermal Conductivity

Thermal conductivity is a physical property that measures a material's ability to conduct heat. It is defined as the rate at which heat is transferred through a material per unit distance per unit temperature gradient. The SI unit of thermal conductivity is W/(m K), and is often depicted with k. The thermal conductivity of a material depends on various factors such as temperature, pressure, and the material's physical properties, such as density and chemical composition. Materials with high thermal conductivity can conduct heat more efficiently and quickly, making them ideal for applications where heat transfer is important. Suitable substrate materials should therefore have high thermal conductivity.

Specific Heat Capacity

Additionally, specific heat capacity is another physical property that measures the amount of heat required to raise the temperature of a unit mass of a substance by one Kelvin. It is a measure of the intrinsic ability of a substance to store thermal energy, and is expressed in J/(kg K), often depicted by c_p. The specific heat capacity of a material can vary depending on factors such as temperature, pressure, and the presence of impurities. Generally, materials with high specific heat capacity require more heat to be added or removed in order to change their temperature, making them effective at storing and releasing thermal energy. Considering that the amount of energy required to change the temperature of the substrate, materials with low specific heat capacity should be selected.

Thermal Diffusivity

Combining the thermal conductivity and specific heat capacity with the density of a material can be used to define the material property *thermal diffusivity* $\alpha = k/\rho c_p$, a measure of how quickly heat can be transferred through a material from the hot side to the cold side. It is defined as the ratio of the material's thermal conductivity to its heat capacity per unit volume (m^2/s). This material specific quantity describes how quickly a material can respond to a sudden change in temperature.

Importance of Thermal Properties

The importance of these thermal properties can be illustrated by cooling blocks of different materials, and plotting the temperature response of the material. Polymers are known to be thermal insulators, while metals, such as aluminium are good thermal conductors. Two blocks of the same volume (15 x 20 x 6 mm), made from 6061 aluminium and photopolymer (3D printing resin: FEPshop Resin Tough), are shown in figure 4.1. These blocks are placed on the peltier module with a thermal interface material (Prolimatech PK-2) and the temperature of the opposing surface is measured using a DS18B20 sensor. This experiment was conducted in an ambient temperature of 18°C, with a constant current of 4 A applied to the TEC1-12706 peltier module. The peltier was cooled using the setup described in chapter 3. The temperature response of both materials is shown in figure 4.2. In this figure, the time required to cool the surface temperature of the block from room temperature (18°C) down to 0°C is also noted. The aluminium surface responds quickly and reaches freezing temperatures in 15 seconds, and reaches a steady state temperature of -31.62°C. Meanwhile the photopolymer takes 165 seconds to reach freezing temperatures and the lowest temperature obtained during this experiment is -6°C.

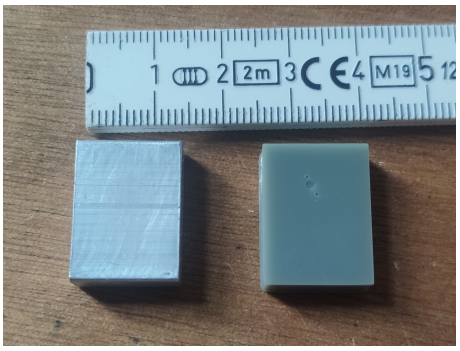

Figure 4.1: 6061 Aluminium (left), photopolymer (right)

This shows that for applications where the time required to adhere to ice is critical, thermal properties play a significant role and should be considered in the material selection procedure.

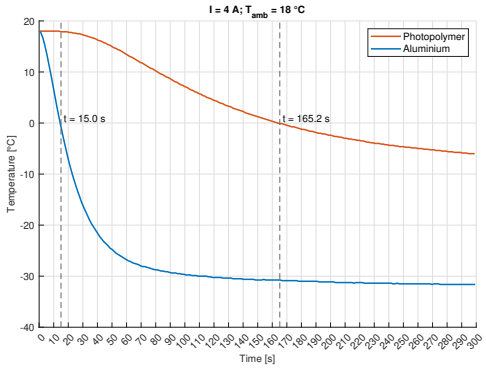

Figure 4.2: Temperature response of aluminium and photopolymer

4.2.3. General Properties

Apart from material characteristics important for adhesion strength and energy consumption, some additional properties can be considered as well.

Density

Low density (kg/m^3) substrate materials is preferred for two reasons. First of all, it is beneficial since the heat capacity of a volume is a function of specific heat capacity and density, combined they are the volumetric heat capacity. This dictates the energy required to change the temperature of a material per unit volume. Secondly, the low density materials are preferred for applications where low mass components are favored.

Corrosion Resistance

Since the substrate material is in frequent contact with liquid water, the material should have high durability in aqueous solutions to prevent corrosion.

4.3. Material Selection Process

For the selection procedure, the material database Ansys Granta EduPack 2021 R2 is used. This database provides an extensive overview of the material 'kingdom', which contains the families of Ceramics, Polymers, Metals, Natural Materials, Foams and Composites. The families are subdivided by classes, which are filled with members, each with their own attributes; intrinsic material properties. This allows for a structured overview and comparison between materials, and a material selection procedure based on a set design problem, with the help of Ashby plots. For this procedure material constraints and material indices need to be constructed, which can be made with the desired material properties described in the previous section.

Although surface energy is a crucial material property for intrinsic ice adhesion strength, the unavailability of sufficient data on material surface energies renders it inappropriate for the initial material selection process. Therefore materials are initially selected based on the thermal properties, for those candidates the surface energy is retrieved from literature.

4.3.1. Design Brief

A design brief is constructed and shown in table 4.1. This design brief describes the *function* of the material, secondly it contains the *objective* of the selection process; what is to be minimized or maximized? Then additional *constraints* are applied to the selection, these constraints can help simplify the material index or can be used to filter out unsuitable materials.

Table 4.1: Substrate material design brief: thermal properties

Function	Adhesion pad substrate material (cyclic heating and cooling)
Objective	Minimize energy required for temperature cycle
	Minimize temperature cycle time
Constraints	Volume is specified
	Operating temperature -30 to 100°C
	High durability in aqueous solutions

Material Index

Now, the general heat conduction equation for isotropic materials is (Fourier-Biot equation) is used to find the appropriate material index:

$$\frac{\partial}{\partial x}\left(k\frac{\partial T}{\partial x}\right)+\frac{\partial}{\partial y}\left(k\frac{\partial T}{\partial y}\right)+\frac{\partial}{\partial z}\left(k\frac{\partial T}{\partial z}\right)+q_v=\rho c_p\frac{\partial T}{\partial t} \tag{4.1}$$

where T is the temperature of the material (K), k the material's thermal conductivity (W/(m K)), q_v the internal heat generation/sink rate per unit volume (W/m^3), ρ the density of the material (kg/m^3), c_p is specific heat capacity of the material (J/(kg K)) and t is the time (s). With no internal heat generation/sink this becomes the transient (diffusion) equation, considering an isotropic material ($k_x=k_y=k_z=k$), in vector format:

$$k\left(\nabla^2 T\right)=\rho c_p\frac{\partial T}{\partial t} \tag{4.2}$$

considering diffusivity is $\alpha=k/\rho c_p$, and substituting:

$$\alpha\left(\nabla^2 T\right)=\frac{\partial T}{\partial t} \tag{4.3}$$

The time is minimized by choosing materials with a high value of thermal diffusivity α. Similarly, the energy Q required to change the temperature of the block is governed by the specific heat capacity and density, considering that the volume and temperature difference are not free variables:

$$Q=\rho V c_p\Delta T \tag{4.4}$$

In this equation, V denotes the volume of the block. Thus, finding materials with high material index:

$$M_1=\alpha=\frac{k}{\rho C_p} \tag{4.5}$$

will ensure that selected materials for the adhesion pad will quickly respond to applied temperature changes from the peltier module without storing large amounts of heat.

4.3.2. Material Selection Chart: Ashby Plot

Figure 4.3 shows the chart constructed in Granta EduPack 2021 R2, this chart shows materials from different families and are arranged according to thermal diffusivity on the x-axis and thermal conductivity on the y-axis, as a result, the contour lines indicate constant volume specific heat ($J/(m^3K)$). The best performing materials according to the described material index M_1 are found in the right side of the chart (increasing thermal diffusivity). Note that in this case, the thermal conductivity is included in the material index M_1 and could therefore be left out of the chart as the y-axis property.

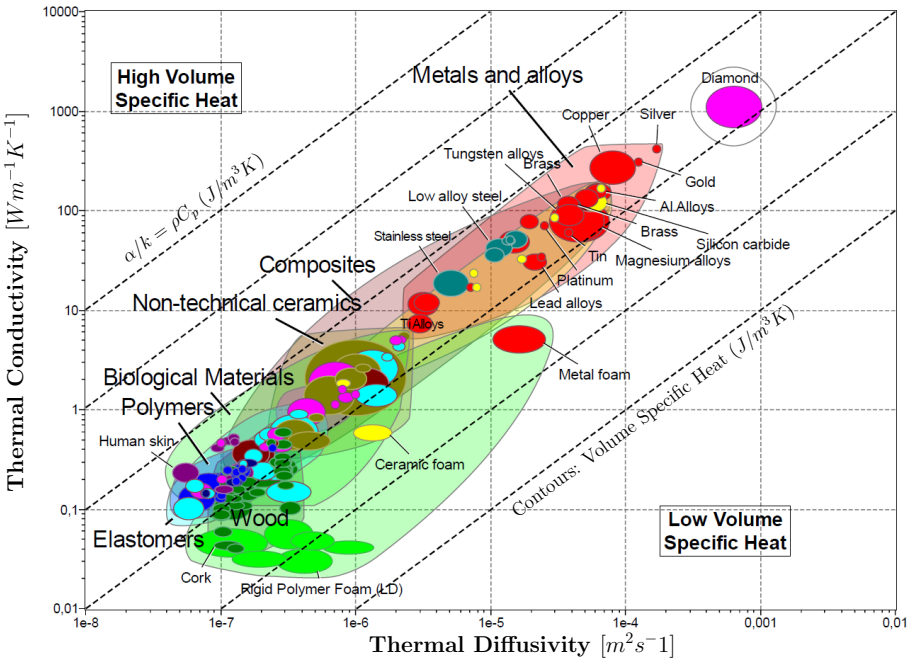

Figure 4.3: Thermal conductivity plotted against thermal diffusivity. Contour lines indicate volume specific heat. Materials performing well for material index $M_1 = \alpha$ are found in the right side of the chart. Images used courtesy of ANSYS, Inc.

Selection Filters

Selection stage filters are used to exclude materials that have low durability in aqueous solutions (fresh and salt), since the adhesion pad will be in frequent contact of liquid and solid water. Additionally, the material will be cooled and heated frequently and should therefore be able to handle sub-zero temperatures (-30 °C) and temperatures up to 100 °C, to match the operating range of the thermo-electric cooling setup. Then, materials with the highest thermal diffusivity are selected and listed in 4.2.

4.3.3. Material Selection: Table

Materials with the highest thermal diffusivity and passing the selection filters are listed in table 4.2.

Table 4.2: Selection of materials with corresponding properties. Material properties sourced from Granta Edupack R2, unless cited otherwise.

Material	Thermal Diffusivity (mm^2s^{-1})	Density (kgm^{-3})	Surface Energy (Jm^{-2})	Young's Modulus (GPa)	Thermal Expansion $\mu strain K^{-1}$
Diamond	500 - 1200	3500	0.6 [92] - 9.1 [76]	1050 - 1210	0.8 - 1.2
Graphite	50 - 150	2260	0.2 - 0.34 [23]	9 - 18	1.84 - 2.05
Silver	166 - 174	10500	1.12	70 - 74	18.5 - 20
Gold	119 - 130	19300	1.39	76 - 81	13.5 - 14.5
Copper	54 - 116	8960	1.72	120 - 140	16.8 - 18.9
Aluminium Alloys	51 - 73	2640 - 2810	0.5 - 0.9 [4]; Al: 1.08	68 - 76	22.7 - 24.6
Magnesium Alloys	27 - 69	1750 - 1870	0.6 - 0.8 [96]	42 - 47	24.6 - 28
Brass (Copper alloy)	35 - 55	8230 - 8800	N.A.[1]	93 - 120	16.5 - 20.6
Tungsten Alloys	31 - 44	16900 - 18600	N.A.; W: 2.64	310 - 370	4.26 - 5.7

Material Discussion: Diamond

Diamond is the clear winner in terms of thermal diffusivity, as visible in table 4.2 as well as the chart 4.3. Reduction in production cost of polycrystalline diamond makes it slowly more accessible for various industries; polycrystalline diamond heat sinks are already used in applications where heat dissipation and weight constraints are key issues [73]. The discrepancy between the reported surface energy can be accredited to different means of measurement [76] or estimation [92], as particle size and number of atoms in diamond nano-crystals influence the surface free energy [76]. While high surface energy is preferred for intrinsic adhesive properties, and surface energies above 0.5 J/m^2 can be considered high, surface treatments can also increase surface energy. In terms of thermal expansion, diamond is an inferior choice to other materials listed, while having the lowest thermal expansion coefficient, it is least compatible with the thermal expansion coefficient of water ice (49-53 $\mu strain K^{-1}$). Nevertheless, the primary reason diamond is not selected as an adhesion pad material candidate is the high material cost, and difficulties involved with manufacturing/processing the material to desired shape.

Material Discussion: Graphite

Graphite is another carbon-based candidate with high thermal diffusivity. While monolayer carbon nanosheets or nanotubes (graphene) would outrank diamond in terms of thermal diffusivity, they are excluded as the material shapes are limited to sheets and tubes with a thickness of a single atom. Graphite is essentially made up from many layers of graphene and has a more practical form factor for the application of ice adhesion pads. Thermal diffusivity and conductivity is excellent, but highly influenced by the anisotropy of the graphite structure. Graphite conducts heat well in a direction parallel to the hexagonal rings of carbon the material consists of, while the heat conduction perpendicular to these planes is poor; it acts as a thermal insulator. Although diamond and graphite are both made from exclusively carbon atoms, the tetrahedron atom structure of diamond makes it a very hard material with high strength. Graphite on the other hand, has weak intermolecular forces acting between the layers, causing easy separation or sliding between the layers, making graphite much softer. Graphite's Young's modulus of elasticity changes by up to two orders of magnitude depending on the direction of loading. The brittle nature of graphite decreases the durability, frequent contact with hard surfaces make it susceptible to chipping and fracturing. Due to the low durability, high material cost and anisotropic mechanical properties, graphite is not considered to be a suitable material to function as a contact surface for ice adhesion.

[1] Brass is a copper alloy that contains 5-40 wt% zinc and can have trace amount of other elements. The surface energy of copper is 1.72 J m^{-2}; zinc has a surface energy of 0.84 J m^{-2}. Brass is expected to have a surface energy in similar range.

Material Discussion: Silver and Gold
Silver and gold are both precious metals with good thermal characteristics and surface energy. At this time of writing, the material cost is the most obvious disadvantage of either material, since the volume of the adhesion pad is constrained. To illustrate, material cost of a single adhesion pad 40x40x10 mm in size would cost close to €17.000 if made from pure gold, and €140 when choosing silver. Apart from material cost, both materials have relatively high density which is undesirable when selecting materials for small scale robotics systems, where weight should be kept to a minimum.

Material Discussion: Copper
Copper is the most used metal in applications where high thermal and/or electrical conductivity is required. Pure copper has a thermal diffusivity of 116 mm^2/s, accompanied with high surface energy (1.72 J/m^2 and stiffness (130 GPa). Thermal expansion of copper is roughly three times smaller than the thermal expansion of ice. The downside of copper is the relatively high density. Machinability is good; no special tooling required.

Material Discussion: Aluminium
Aluminium alloys are very versatile materials; by varying the composition and heat treatment steps, desirable material properties for widespread applications can be obtained. Aluminium alloys have excellent strength-to-weight ratio and is a good thermal conductor, making it suitable for lightweight and affordable heat sink applications. Alloyed aluminium has a surface energy between 0.5 - 0.9 J/m^2 [4], roughly 50% less than pure copper. Meanwhile the thermal expansion incompatibility between aluminium alloys and water ice is slightly better than that of copper and water ice. The low density of aluminium alloys makes it a suitable material for applications where weight is important. Material cost is lowest of all materials listed. Machinability is excellent.

Material Discussion: Magnesium
Magnesium alloys are comparable to aluminium alloys in many aspects, with similar upper limit to thermal diffusivity. The low density of magnesium alloys makes is an interesting material for low weight solutions for ice adhesion pads. From the materials listed in table 4.2, magnesium alloy have the highest compatibility for thermal expansion with water ice. However, while no specialized tooling is required for machining magnesium alloys, the material causes a metal fire hazard when small chips or dust are produced, which makes it unsuitable for processing with available facilities.

Material Discussion: Brass
Brass is a copper alloy with similar material properties as pure copper. However there are no conspicuous advantages in using brass over copper; most material properties are less desirable with only a marginal decrease in density.

Material Discussion: Tungsten
Tungsten alloys are known for their high density, high temperature resistance and hardness. It is an excellent choice for wear resistant applications, radiation or temperature shielding. But machinability, cost and the density make it a poor choice for the application of ice adhesion contact surface.

4.3.4. Selected Materials: Copper and Aluminium

From this material comparison, copper and aluminium alloys are the most fitting materials to be tested in terms of ice adhesion strength, temperature response time and time-to-adhere. Aluminium alloys can provide low cost and low weight solution, but the surface energy is roughly 50% less than pure copper, depending on the alloy. Aluminium alloys have lower thermal diffusivity, but volumetric heat capacity ($c_v = c_p\rho$), in $J/(m^3\ K)$, is $913 \times 2710 = 2474.2\ kJ/(m^3K)$. When for copper the volumetric heat capacity is, $385 \times 8960 = 3449.6\ kJ/(m^3K)$; copper requires roughly 39% more energy to change the temperature by 1 degree K, compared to a block of aluminium of the same volume. Here the volumetric heat capacity is more useful to compare materials, since the adhesion pad is constant volume, rather than constant mass. Comparing copper and aluminium should also provide insightful information about the effect of surface energy on adhesion strength for an ice adhesion actuator.

4.4. Surface Treatment

To investigate the effect of surface treatment on ice adhesion strength, the adhesion pad inserts will be manufactured with three different surface finishes. In this research, only mechanical treatments are tested, while other common treatments include chemical and electromechanical methods.

Polished Surface

One of the surface treatments is a polishing process that uses abrasives with decreasing roughness or particle size to obtain a flat, smooth and reflective surface without defects. This surface finish should provide more insight in the intrinsic ice adhesion properties of both materials, since there are no features that enable the mechanical interlocking effect. The adhesion pad surfaces are polished using a metallographic sample grinding and polishing machine, the final wet sandpaper grit is K4000. This leaves a smooth and reflective surface, as seen in figure 4.4a.

Grit Blasted Surface

The surface free energy of a surface can be altered by increasing the surface roughness, a practice commonly applied to increase the strength of adhesive joints [70]. To obtain a uniform surface roughness, the adhesion pads are treated with a grit-blasting roughening process, also known as sandblasting, abrasive blasting or media blasting. Figure 4.4b shows the adhesion pads with grit blasted surface.

Grid Pattern Surface

Lastly, the surface of two adhesion pads are machined to create protruding surface features. This should have two effects, first of all, the effective contact area is increased while the overall dimensions of the adhesion pad are equal to the other pads. And secondly, the protruding features should aid the mechanical interlocking effect between the adhesive and substrate. In this research, a basic chequered pattern is created in the adhesion pads using the available facilities. This pattern is milled in the surface of the adhesion pads to a depth of 1 mm using a horizontal milling machine with a 1.5 mm HSS end mill cutter. The grooves created with this process are spaced 3.5 mm apart, and at a 90°angle to create a grid like pattern. This surface has a contact area of 2125.2 mm^2, an increase of $\sim$69% compared to the other two surface treatments (1256.6 mm^2 for reference). The resulting adhesion pads are shown in figure 4.4c.

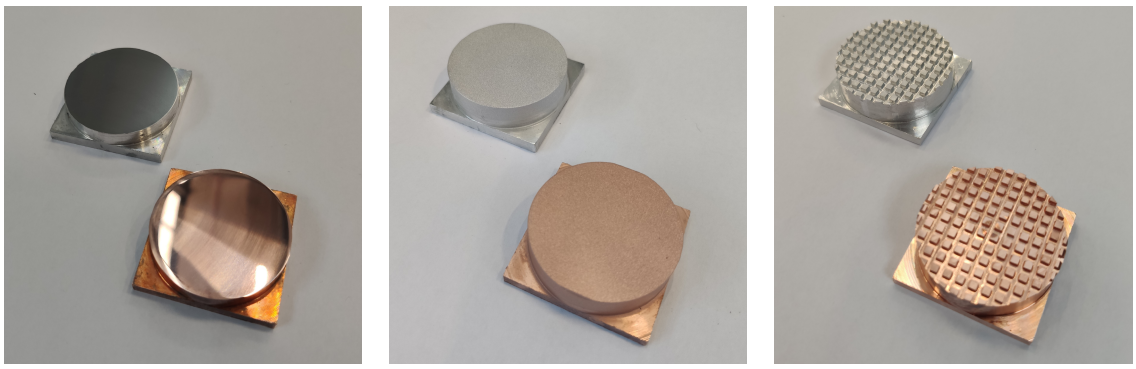

(a) Polished surface finish. **(b)** Grit-blasted surface finish. **(c)** Surface with protruding features.

Figure 4.4: Aluminium and copper adhesion pads with three different surface treatments.

4.5. Experiments: Thermal Properties

Temperature Response

Adhesion pads inserts are manufactured from the materials selected in this chapter. Here the temperature response of the adhesion pad materials fitted to the thermoelectric cooling setup is tested. For this test, the adhesion pad is fitted to the TEC1-12706 peltier module with a thermal interface material (Prolimatech PK-2), and a DS18B20 temperature sensor is attached to the opposite surface. Similarly, this surface is the adhesion surface contacting the ice during the adhesion tests performed in later experiments. Figure 4.5 shows the temperature response of both materials during the test for a duration of 200 s, with an amperage of 3 A.

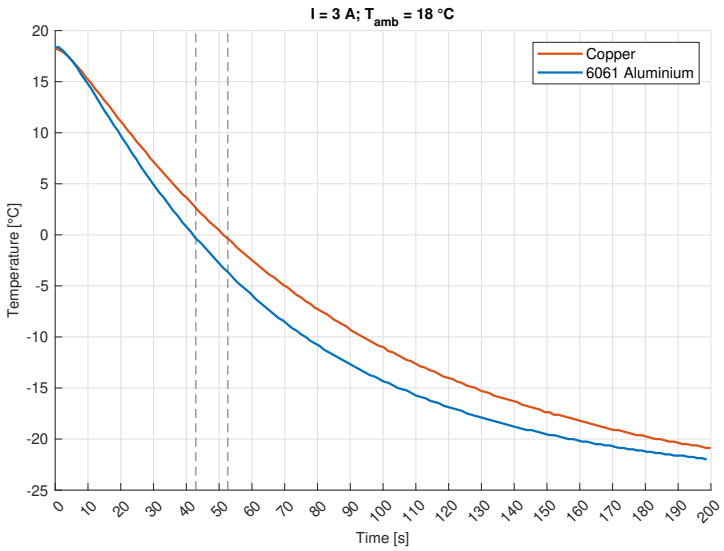

Figure 4.5: Temperature response of the selected adhesion pad materials when fitted to the thermoelectric cooling setup.

This test indicates that the aluminium adhesion pad takes less time to reach sub-zero temperatures compared to the copper adhesion pad in the thermo-electric cooling setup. The temperature of both materials rapidly drop after powering the peltier module, and the time required to reach 0°C is 52.7 s and 42.9 s for the copper and aluminium materials, respectively. Copper takes roughly 23% longer to reach freezing temperatures.

Time-to-Adhere

The temperature response graph shown in figure 4.5 provides information about the substrate material's ability to change temperature when cooled exclusively by the peltier element. In reality, the adhesion pad contacts an icy surface, which absorbs a large portion of the thermal energy of the adhesion pad; greatly reducing the time required to reach the sub-zero temperatures required to adhere the substrate to the ice (time-to-adhere). Therefore, the time-to-adhere is measured for both substrate materials. For this measurement, a block of ice at -10°C is used with an initial adhesion pad temperature of 18°C. As soon as the adhesion pad contacts the ice, the peltier element is powered on and the time required until the adhesion pad seizes the ice:

- Time-to-adhere, copper adhesion pad: $\sim$8.5 seconds
- Time-to-adhere, aluminium adhesion pad: $\sim$6.8 seconds

This shows that the ice certainly absorbs the majority of the thermal energy, drastically reducing the time required to reach sub-zero temperatures. The time-to-adhere of copper is roughly 25% higher than that of aluminium. Indicating that, the difference in time-to-adhere is scaled similar to difference in the time required to reach 0°C in figure 4.5.

4.6. Conclusion

In this chapter, two materials are selected following a selection procedure. Materials were initially selected based on the thermal properties, resulting in a list of 10 materials. Coincidentally, all of these materials also have surface energies that can be considered high. The properties of all 10 materials are discussed, exposing crucial factors that eliminate the material in the selection.

Following this process, copper and aluminium were selected as the most suitable materials to be tested. While both materials have high thermal diffusivity, the surface energy of copper is significantly higher than aluminium. Meanwhile, the density of aluminium is much lower than that of copper, resulting in a lightweight solution. Since surface energy is expected to show a good relationship with ice adhesion strength, testing the ice adhesion strength of both materials should be an interesting comparison. This comparison should indicate whether the high surface energy of copper, outweighs the cost of the high density, compared to aluminium.

Additionally, three surface treatments are proposed to be tested in the ice adhesion strength experiments. These surface treatments are have an increasing surface roughness; polished, grit-blasted and machined grid pattern.

The materials are used to manufacture the adhesion pads that can be interfaced in the ice adhesion effector developed in chapter 3. Demonstrations have shown that the thermoelectic cooling system is capable of cooling the adhesion pads sufficiently to reach the sub-zero temperatures required to establish an adhesive connection between substrate and ice. Comparing the aluminium and copper materials, aluminium shows the best temperature response time. Additionally, measuring the time-to-adhere indicate that an adhesive connection can be established in less than 9 seconds, which could be further decreased if required.

Now with the thermoelectric cooling system and adhesion pads complete, the next step is to test the ice adhesion strength of the system. These experiments are described in chapter 5.

5

Ice Adhesion Strength Experiments

This chapter describes the ice adhesion experiments that are performed to quantify the adhesive strength of the ice adhesion effector with the two substrate materials and three surface treatments selected in chapter 4. The tests are performed at the Material Science and Engineering department in the faculty of Mechanical, Maritime and Materials Engineering of Delft University of Technology.

5.1. Experimental Setup

This section describes the materials used in the experimental setup, which is shown in figure 5.1.

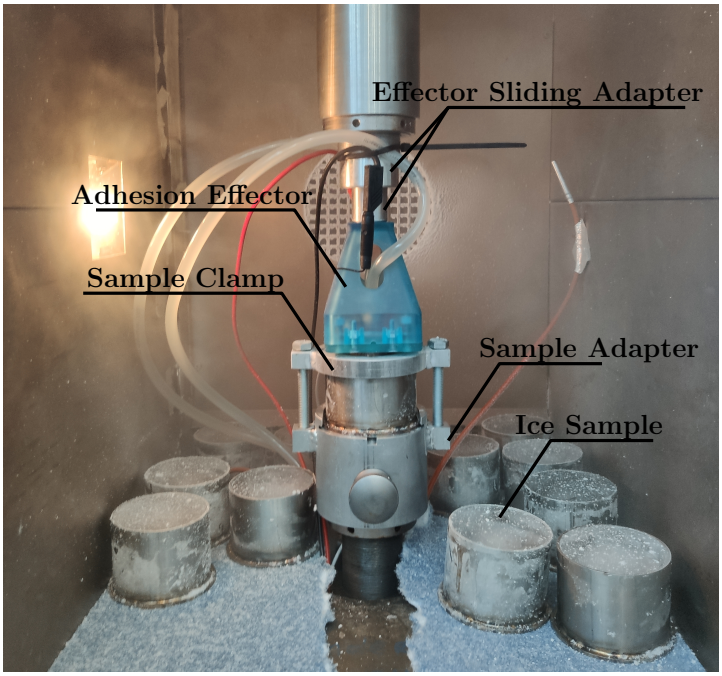

Figure 5.1: Experimental setup in temperature chamber

5.1.1. Testing Apparatus

Tensile Testing Machine

The testing machine used to perform the tensile pull-off tests is a Zwick Roell Z100 AllroundLine Universal testing machine. This machine has a test speed range from 0.00005-100 mm/min, travel resolution of 0.484 µm, repetitional position accuracy of $\pm$2 µm. Data is acquired with a rate of 400 kHz with 24 bit resolution and transferred to the connected computer at 500 Hz. The cross bar is fitted with a 100 kN load cell (Zwick Roell XForce K; 100 kN), this load cell type (XForce K) has a typical accuracy (maximum display deviation) <$\pm$0.25% of the measured value from 0.4% of load cell capacity; from 0.1% of load-cell capacity the accuracy is <1% of measured value. The calibration and accuracy of the load cell is in accordance with ISO 7500-1.

Testing Environment

The tests are performed inside a temperature controlled chamber to warrants a constant environmental and ice temperature throughout the tests. This temperature chamber has a temperature range of -80°C to 250°C and can be fitted to various testing machines. In this case, it is fitted to the Zwick Roell Z100 AllroundLine Universal testing machine. The temperature chamber is electrically heated and requires supplied liquid nitrogen for cooling, therefore an insulated vat with a capacity of 20 liters is filled with liquid nitrogen before each set of experiments.

Ice Adhesion Effector Mounting

The ice adhesion effector described in chapter 3, which can be fitted with the six different adhesion pads described in chapter 4, is mounted to the tensile testing machine using a sliding adapter. By restricting side to side movement of the effector, uneven interfacial stresses between the adhesion pad and ice sample, that can decrease the reliability of the tests, are eliminated. While side to side movement are restricted, the adapted allows the effector to move up once the adhesion pad contacts the ice, this ensures the adhesion pad applies constant pressure on the ice during the melting phase.

5.1.2. Ice Samples

Ice samples are required to test the ice adhesion effector in the tensile pull-off testing machine. As the tests will be executed until either the ice or the adhesion fails, a new sample is used for each test. Therefore a batch of ice samples should be prepared in advance of the experiments. Additionally, the samples should be held securely in the tensile testing machine.

Ice Sample Freeze Technique

Water in contact with air, such as natural water and drinking water, is in equilibrium with gases such as nitrogen, oxygen and carbon dioxide. While the freezing point of fresh water is 0°C, the dissolved gases have much lower freezing temperatures, preventing the gases from freezing in conditions found in most freezers (-20°C). As a result, freezing water in a container causes the concentration of gases in liquid water to increase as the ratio of solid/liquid phase increases. Once this highly concentrated gas solution reaches the stationary concentration at the phase boundary, nucleation will occur and gas bubbles form [41]. These bubbles are inevitably encapsulated by the forming ice, this causes the formed ice to appear 'cloudy', as illustrated in figure 5.2. While the aesthetics are not of concern for these experiments, the

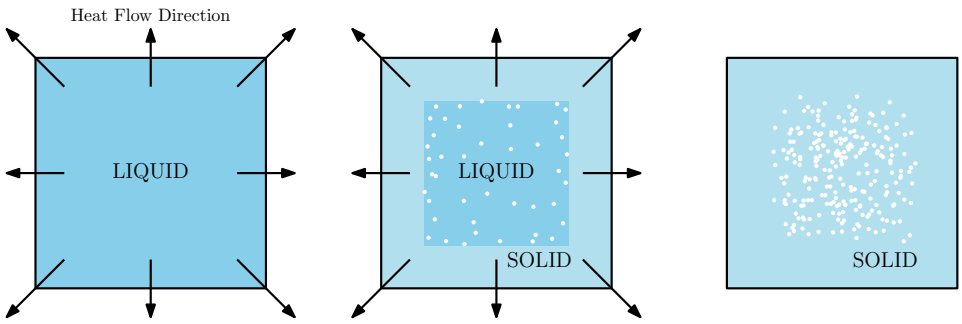

Figure 5.2: 'Regular' freezing of ice; formation of bubbles causing cloudy ice.

inclusion of bubbles in the ice are defects and weaken the block of ice, as they can act as crack initiators

and promotors. Since freezing water under normal circumstances is a natural process, the distribution of these bubbles will be different for each sample, possibly causing high variance in the tensile pull-off results. Using distilled or demineralized water eliminates the formation of solids, such as chalk, but will still contain dissolved gases. While boiling water will drastically reduce the amount of dissolved gases in the water, it will not completely eliminate all gases because by the time the water has cooled down to 0°C, some gases will have dissolved back in to the water. It is therefore impossible to freeze a container of water that is completely void of bubbles. But by using a directional freezing technique, it is possible to force all the bubbles to form in a specific area of the container. This method relies on insulating the sides of the container whilst leaving a single or surface exposed to cold temperatures. This forces the heat to be extracted in a single direction, or similarly, the water to freeze from one direction, as shown in figure 5.3. In the example shown in 5.3, the bubbles form in the bottom of the container, leaving the upper half of the ice clear of any defects. If it is desired to create a block of ice completely void of bubbles, it is possible to stop the freezing process before bubbles are formed and draining the remaining, highly concentrated gas solution, leaving a block of ice smaller than the container. Alternatively, the bottom half containing the bubbles can be melted until desired height.

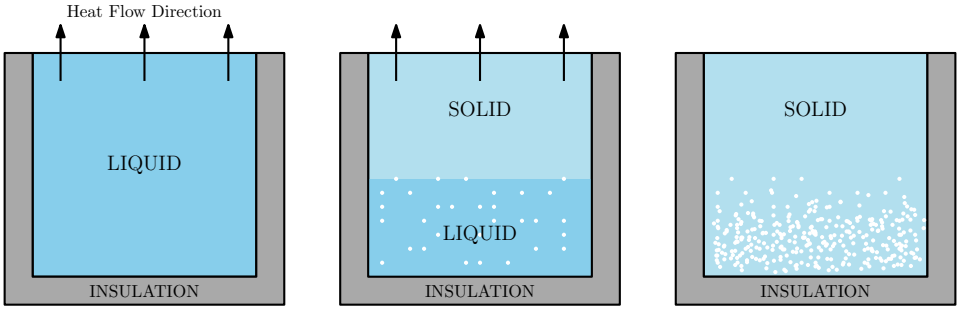

Figure 5.3: Directional freezing; bubbles formed at bottom of container, creating thick clear section near the top.

The ice block resulting from this directional freeze method is shown in figure 5.4a, compared to an ice block frozen without insulation in figure 5.4b.

(a) Ice sample created with directional freeze technique; clear ice.

(b) Ice sample created without directional freezing; regular ice.

Figure 5.4: Comparison of ice samples created with different freezing methods.

The directional freeze technique results in a block of ice where the top half of the volume is void of any defects; the ice is transparent. Meanwhile the regular ice is opaque throughout the volume; air bubbles and cracks are spread in the volume from the freezing process. In order to increase repeatability of the ice adhesion tests and allow a comparison between adhesion strength of the different adhesion pads, the directional freeze technique is applied to generate the ice samples used in testing, to decrease variability in ice sample strength.

Ice Sample Container

The ice sample containers are constructed from 80 mm stainless steel tubing with a wall thickness of 2 mm, this tube is cut to 60 mm lengths and the ends are squared on a manual lathe. A circular, stainless steel disk is welded concentric to the bottom of this tube to create a watertight container. The disk fitted to the bottom has a thickness of 3 mm and diameter of 90 mm. The larger disk diameter creates a lip at the bottom of the container, which acts as the feature to secure the container. A total of 12 containers are fabricated for the experiments, three of which are displayed in figure 5.5. These containers are placed in an styrofoam tray to insulate the sides and bottom, to effectuate the directional freeze method. With this method, a total of 12 ice samples can be prepared in 24 hours.

Figure 5.5: Ice sample container

Ice Sample Adapter and Clamp

The CAD design of the sample adapter is shown in figure 5.6. This sample holder can be attached to the bottom mounting shaft of the Zwick Roell Z100 testing machine with a 30 mm pin and a retaining nut removes any clearance between the parts. The ice sample containers are indexed in the adapter to align vertically with the adhesion effector using the bottom lip of the sample container. Vertical movement is constrained by the sample clamp, eliminating any vertical clearance.

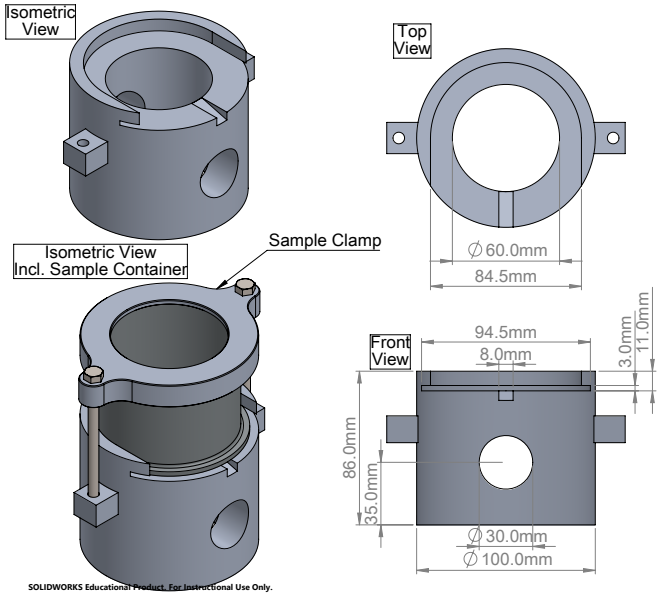

Figure 5.6: CAD design of ice sample holder.

5.1.3. Procedure

The tests are all performed in the temperature chamber set to -15°C. By placing the ice samples in the chamber before the test, the internal ice temperature equalizes to the temperature of the chamber. Additionally, the H-Bridge control box is activated to cool the peltier module, so that the adhesion pad is at sub-zero temperature before the test begins. Then, the following procedure is repeated:

1. Ice sample is placed in the sample holder and secured by the sample clamp.
2. Cross bar is lowered to the pre-defined starting height, such that the adhesion pad rests on the ice with only the weight of the adhesion effector.
3. The temperature data logger is activated, this also initializes the heating-cooling cycle of the H-Bridge control box.
4. A buzzer sounds when the heating-cooling cycle is complete, the adhesion pad is now connected to the ice. Tensile pull-off test is initialized on the PC, raising the cross-bar until a pre-load of 20 N is measured; eliminating any clearance in the effector sliding adapter.
5. Tensile test machine moves the cross bar up with a test speed of 100 µm/s, recording the measured force of the load cell until a break is detected.
6. After a break is detected, the cross bar is raised manually and the sample is removed.
7. Any residual ice on the adhesion pad is manually removed. The failure mode of the ice sample is inspected and documented together with the force at break.

5.2. Results

The two substrate materials selected in chapter 4 are both tested with three different surface textures, resulting in a total of six different adhesion pads. The tensile pull-off adhesion strength of each adhesion pad is tested with six ice samples, resulting in a total of 36 measurements.

Recorded Tensile Pull-Off Force

The results of all 36 measurements are displayed in figure 5.7, the markers here indicate the maximum force recorded during the tensile pull-off tests.

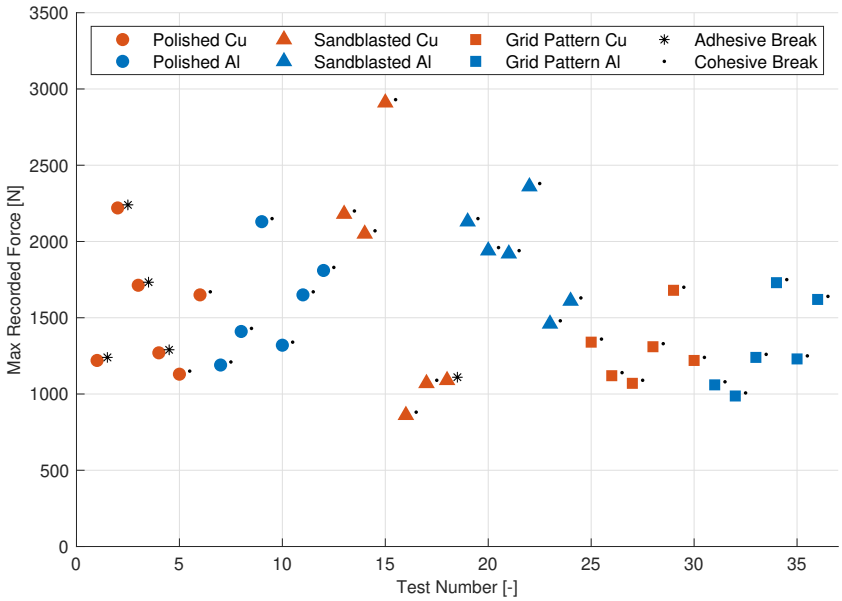

Figure 5.7: Test results of the tensile pull-off tests for the six adhesion pads.

Adhesion Strength

Table 5.1 lists the measured adhesion strength of the six adhesion pads using the projected area of the pads. In this case, the projected area is used rather than the actual contact area. The projected area of the adhesion pad is the two dimensional measurement of the adhesion pad, and does not include any additional area resulting from surface alterations. For example, the projected surface area of all the adhesion pads is: $\pi \times 20^2 = 1256.6$ mm^2, while the actual surface area of the grid pattern adhesion pads contacting the ice, derived from the 3D CAD model, is 2125.2 mm^2. The projected area is used in this research in order to evaluate the adhesive/grip strength of the effector as a whole, and to determine if the added contact area of the adhesion pad with grid patterns translate to an increase in adhesive strength, while the overall dimensions are equal to the other adhesion pads.

Table 5.1: Mean ice adhesion strength for the six adhesion pads, including standard deviation.

Surface Type	Material	Mean adhesion strength [MPa]	Standard deviation [MPa (%)]
Polished K4000	Copper	1.220	±0.299 (24.5%)
	Aluminium	1.261	±0.253 (20.1%)
Sandblasted	Copper	1.348	±0.589 (43.7%)
	Aluminium	1.515	±0.239 (15.8%)
Grid Pattern	Copper	1.026	±0.158 (15.4%)
	Aluminium	1.043	±0.218 (20.1%)

Failure Mode

After a break is detected, the sample is removed from the setup and the failure mode is inspected. Ice remnant on the adhesion pad is an indicator of a cohesive break, meanwhile a surface is void of any ice is an indicator of an adhesive break. Similarly, the surface of the ice sample is inspected for damage in a similar fashion to the inspection of the adhesion pad. Photographs of the ice samples are taken in addition to the visual inspection. Figures 5.8a and 5.8b illustrate the differences to what is considered a 100% adhesive and 100% cohesive break, respectively. Indeed, a combination of the two failure modes is also possible; figure 5.8c shows an example of what is considered a 60% cohesive break.

(a) Ice sample with 100% adhesive failure mode.

(b) Ice sample with 100% adhesive failure mode.

(c) Ice sample with 60% cohesive failure mode.

Figure 5.8: Examples of ice samples after testing, displaying different failure modes.

While it is difficult to determine the exact failure mode ratio by visual inspection only, the governing failure mode is observable. That is, whether the failure was *mostly* adhesive or cohesive. The governing failure mode is noted for every test and is also indicated in figure 5.7.

Temperatures During Testing

The internal ice sample temperature during the experiments is recorded and the average temperature during a set of six tests for each adhesion pad is shown in the right graph of figure 5.9. The left graph of figure 5.9 shows the average temperature in the test chamber for each adhesion pad.

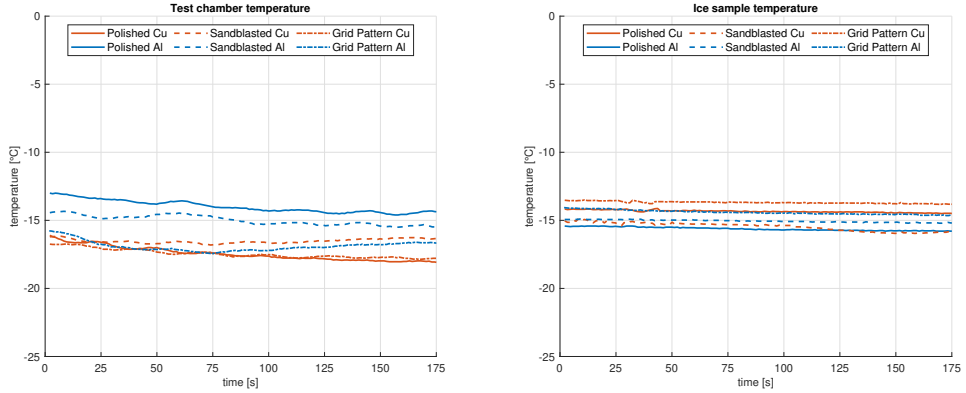

Figure 5.9: Average ice sample temperature (right) and test chamber temperature (left) during the experiments.

5.3. Discussion & Conclusion

These ice adhesion experiments mark the end of the development of the switchable ice adhesion effector in *this* research. With the tensile ice adhesion strength quantified, as well as some key design considerations, the implementation of ice adhesion methods in robotics for climbing on icy surfaces is no longer an abstract idea.

Adhesion Strength

An in depth comparative study between the adhesion pads in terms of adhesion strength and testing procedure can be found in appendix B. The tensile pull-off tests indicate that the aluminium adhesion pad insert with a grit-blasted surface treatment results in the highest measured ice adhesion strength. In fact, the aluminium material shows a higher adhesion strength compared to copper for all surface treatments; the difference in surface energy of the materials (aluminium having roughly %50 lower surface energy), showed to have no negative effect on the adhesion strength.

Results indicate that the ice adhesion strength of the ice adhesion effector surpasses the cohesive strength of ice in most of the tests. Even the lowest measured force of the final set of experiments (861 N) would be able to support the weight of an average human weighing 75 kg, off a disk 40 mm in diameter. This is a promising prospect for the feasibility to integrate this effector small scale robotic systems, as will be explored in the following chapter 6.

Time-to-Adhere, Mass and Costs

Aluminium is a better material choice for the application of robotic system employing ice adhesion methods in terms of adhesion strength. Additionally, the time-to-adhere measured in section 4.5 is also in favor of the aluminium substrate material. The same conclusions are drawn when comparing the density and material costs; aluminium is the superior material choice for the application of a switchable adhesion effector. Therefore, grit-blased aluminium adhesion pads are used in the robotic system developed in 6.

6

Ice Climbing Robot

This chapter miniaturizes the ice adhesion effector and heat dissipation system, that enables the integration of these components in a robotic system. The robotic system presented here, FLICK (Freeze Locomotion Integrated Chain Kinematics), is the very first prototype that adopts an ice adhesion strategy. Thus, the system will be a proof-of-concept, that displays *one* of many possible embodiments of ice adhesion climbing robots, and hopefully instigates future research.

6.1. Design Requirements

For the first prototype of the ice climbing robot, there are few design requirements. First of all, the mass of the robot should be limited to a maximum of 5 kg. This ensures the system remains of small-scale and thus reduces the required resources. Secondly, the heat dissipation system, or in this case, the liquid cooling system, should be integrated in the payload of the robotic system. It has proven to be an essential part of the ice adhesion effector, and the feasibility of a robotic system that adapts the ice adhesion locomotion strategy enabled by the thermo-electric effect can only be assessed if the heat dissipation system can be miniaturized. Additionally, the robot should be able to support its own weight, including the heat dissipation system through the integrated ice adhesion effectors. Lastly, the robotic system will operate in temperatures down to -15°C.

6.2. Robotic System

Concept

Tracked locomotion, with its extensive contact area on the ground, is especially well-suited for navigating soft, flexible, and uneven terrains. However, it is slower and less energy-efficient compared to wheeled locomotion, and it has lower ability to climb obstacles compared to legged locomotion. The ability to slip on soft, granular surfaces aids in the mobility of tracked locomotion. While this does not translate well to hard icy surfaces where ice adhesion anchor points prevent slip, tracked locomotion has multiple characteristics that make it a suitable choice for an ice adhesion robot. First of all, the movement of tracked locomotion relies on zero-velocity contact points with the surface, but unlike wheeled locomotion, there is no rotation around this point of contact. This allows the main body of the vehicle to move with respect to this stationary anchor point. Secondly, a modular track type allows multiple small adhesion effectors to be integrated in the links; creating multiple anchor points during operation. The track consists of multiple links connected with a 1-DOF passive joint, and is typically driven by one sprocket. Carriers or idle wheels support the track along the body or frame. While motion of a single track is limited to 1-DOF, and the track is constructed from a considerable amount of links, driving and controlling the track is reasonably straightforward.

The proposed concept is a single tracked robotic system, with adhesion effectors integrated in the track links of the track. Then. by controlling the individual track links fitted with the adhesion effector, rigid anchor point should allow the robot to climb on icy surfaces. This concept is illustrated in figure 6.1.

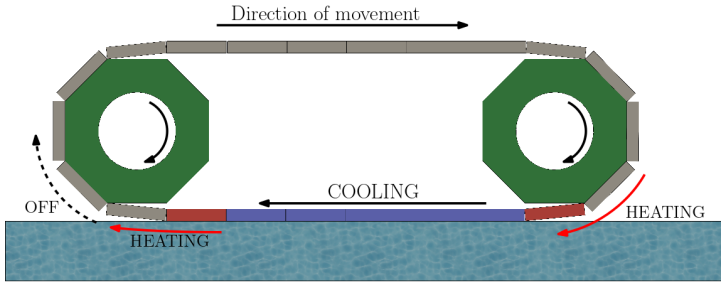

Figure 6.1: Concept of tracked ice adhesion locomotion.

Developed Robotic System
An overview of the complete robotic system is shown in figure 6.2, all major components of the robots are discussed in the following sections.

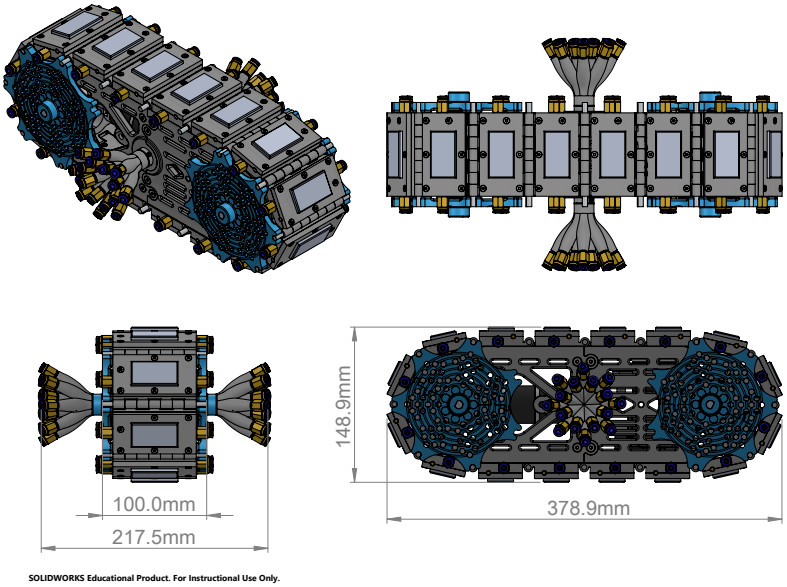

Figure 6.2: 3D CAD Model views of the tracked locomotion ice adhesion robot.

A total of 16 track links make up the whole track, supported by four sprockets. Two sprockets drive the track, while the other two sprockets tension the track. The track moves around a central frame, this frame houses all the components required for driving, controlling and cooling the links. The combined mass of the robot, including the volume of water inside the water cooling loop is 4.2 kg. A 3D view of the model can be explored using the interactive figure 6.3:

Figure 6.3: Interactive 3D CAD view of the robot.

6.2.1. Frame Design and Features

The main body of the robot, as shown in figure 6.4 is dimensioned to accommodate a track with 16 links. The middle section height of the frame matches the track link trajectory, such that the links are supported on the frame. Elongated slots are placed along the sides of the frame to mount the cam track in a adjustable manner. The cam track ensures the track links are switched to *heat, cool* or *off* at the correct position along the frame, explained in detail in section 6.2.3. The underside of the frame features a *track guide rail*, this rail interacts with the carriers fitted to the track links and thus ensures the track links remain close to the frame even at steep incline traveling angles.

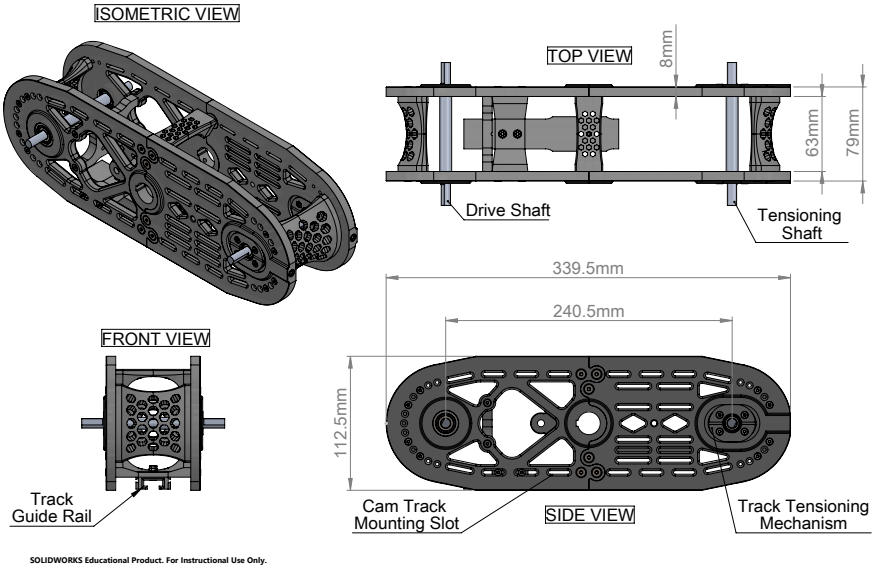

Figure 6.4: CAD Model of the robot frame - Multiple Views

Materials

The structural parts of the frame are made using additive manufacturing techniques. In particular a masked stereolithography apparatus (mSLA) printing technique. The photosensitive resin, or 3D printing material used for the frame is a mixture of two materials; a ratio of 85% SirayaTech Blu V3 and 15% SirayaTech Build with the addition of dark pigment was found to be effective for producing the parts with sufficient tolerances and durability. The drive- and tensioning shaft are produced from 6061 aluminium using basic lathe and mill operations.

Exploded View and Parts

The main body of the robot is constructed from multiple parts, as the exploded view in figure 6.5 illustrates. Since the frame is not a single, solid body, the components building up the frame can be replaced with new iterations without the need of producing a completely new frame.

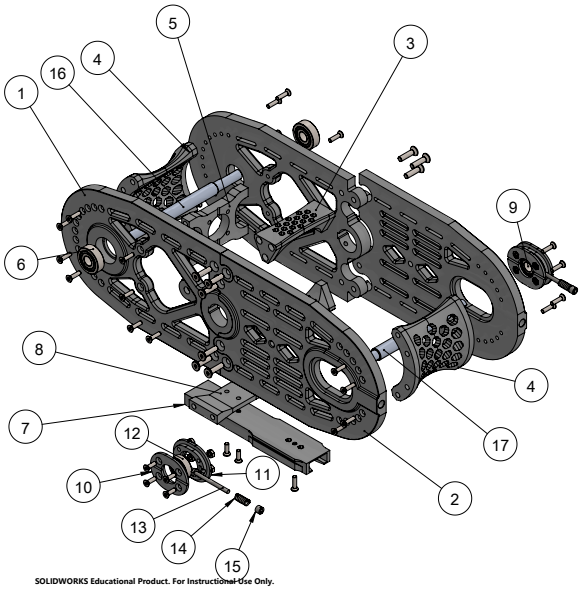

Robot Frame and Parts
Exploded View

ITEM NO.	PART NUMBER	QTY.
1	Frame Side Wall - Driven	2
2	Frame Side Wall - Non Driven	2
3	Frame Center Support	2
4	Frame Outer Support	2
5	Motor Mount Crossmember	1
6	Driveshaft Bearing 608 2RS	2
7	Track Guide Rail	1
8	Guide Rail Cross Member	1
9	Track Tensioning Assembly	2
10	Bearing Housing - 1	2
11	Bearing Housing - 2	2
12	Shaft Bearing 698 2RS	2
13	Track Tensioning Bolt - M3 x 30 HEX	2
14	Track-Tensioning-Spring	2
15	Track Tensioning Nut	2
16	Shaft - Driven	1
17	Shaft - non-Driven	1

Figure 6.5: CAD model of robot frame and parts - Exploded View

Track Tensioning

The track tensioning mechanism (Item No. 9 in figure 6.5) ensures constant tension on the track and is fitted to the non-driven side of the frame. A two part bearing housing (10,11) contains a shaft bearing (12) is able to slide within the elongated slot of the frame, and are tensioned with a compression spring (14). The spring tension can be adjusted with a small adjusting nut (15) on the tensioning bolt (13). This mechanism is illustrated in figure 6.6. At the driven side of the frame, the drive-shaft bearings (6) are pressed directly in the frame side walls.

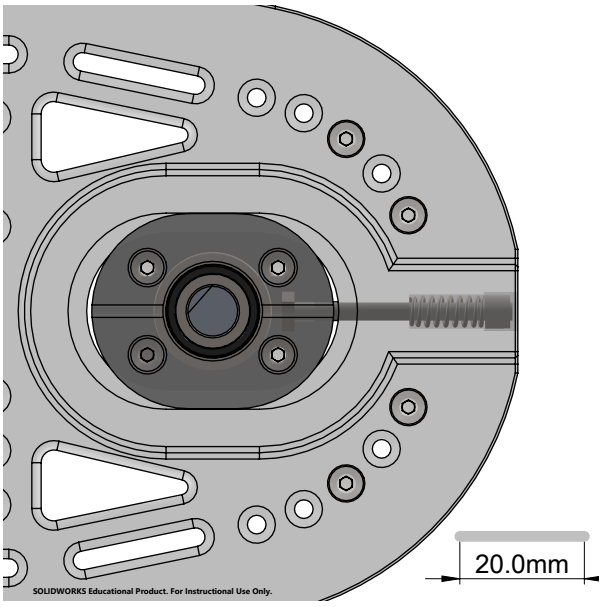

Figure 6.6: Detailed view of the track tensioning mechanism.

6.2.2. Track Link Design and Features

Each link capable of creating adhesive connections with the surface needs multiple integrated parts. First of all, a peltier module is required in order to control the temperature of the adhesion pad. Consequently, a heat sink is required to dissipate the heat rejected at the hot side of the peltier. Similar to the heat dissipation system used in the tensile pull-off adhesive experiments, a water cooling method is selected to dissipate the absorbed heat in the heat sink to the surroundings. Therefore, each track link is required to be part of the closed water cooling loop. Not only do the links require a supply of cool water, the peltier modules need to be connected to a power source as well. The design of the track link to accommodate all the components consists of two parts, the 'track link bottom' and 'track link top' that secure the stack of components, as shown in figure 6.7.

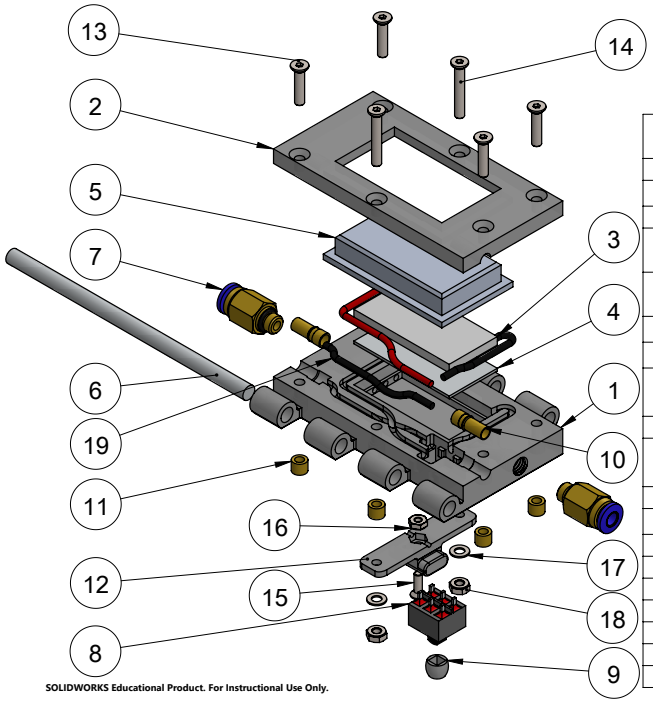

Track Link and Parts
Isometric exploded view

ITEM NO.	PART NUMBER	QTY.
1	Track Link Bottom	1
2	Track Link Top	1
3	TEC1-06308 20x40x3 mm	1
4	Heatsink aluminium 40x20x1.0 mm	1
5	Aluminium Adhesion Pad - Grit Blasted	1
6	Link connecting rod 5x100 mm	1
7	Push in fitting PC-04-M6	2
8	DPDT 28V DC 5A Sliding switch	1
9	Switch Dome Cover	1
10	Female plug 3.5 mm - banana style	2
11	Brass insert M3 - 4.0 mm	6
12	Track Sliding Guide	1
13	M3 x 14 mm Countersunk Bolt	4
14	M3 x 20 mm Countersunk Bolt	2
15	M2.5 x 8 mm Countersunk Bolt	1
16	M2.5 Hex Nut	1
17	M3 Washer	2
18	M3 Hex Nut	2
19	16 AWG Power Wire	1

Figure 6.7: Exploded CAD view of the track link and components.

Part (12) in figure 6.7 indicates the carrier that interacts with the track guide rail mounted in the frame of the robot. This carries slides in the track guide rail and prevents the track to be separated from the frame when loaded, for example when the robot is hanging upside-down.

The adhesion pad in the track link is made from aluminium and has a grit-blasted surface treatment, as this was found to provide the highest ice adhesion strength during the ice adhesion experiments in chapter 5. The pad has a 45x25 mm rectangular surface area. Using the average measured adhesion strength from chapter 5, this pad can support a load of $45\ mm \cdot 25\ mm \cdot 1.515\ MPa\ =\ 1704\ N$ in pure tensile and similar conditions to the ice adhesion strength tests (e.g. ice quality and temperature).

Track Link Bottom

A detailed view of the track bottom link design is shown in figure 6.8. M6 threads on either side of the part allow standard pneumatic push-in fittings to be connected. These pneumatic fittings are also suitable to be used with water, and so flexible tubing can be connected to supply cooling water. Internally formed channels redirect the supplied water to flow underneath the heat sink. The heat sink is an aluminium plate 40x20x1 mm in size, to match the TEC1-06308 peltier module dimensions (40x20x3 mm). Similar to the frame of the robot, the track link bottom and top are created with an mSLA printer, the materials used to print the parts is a ratio of 85% SirayaTech Blu V3 and 15% SirayaTech Build resin.

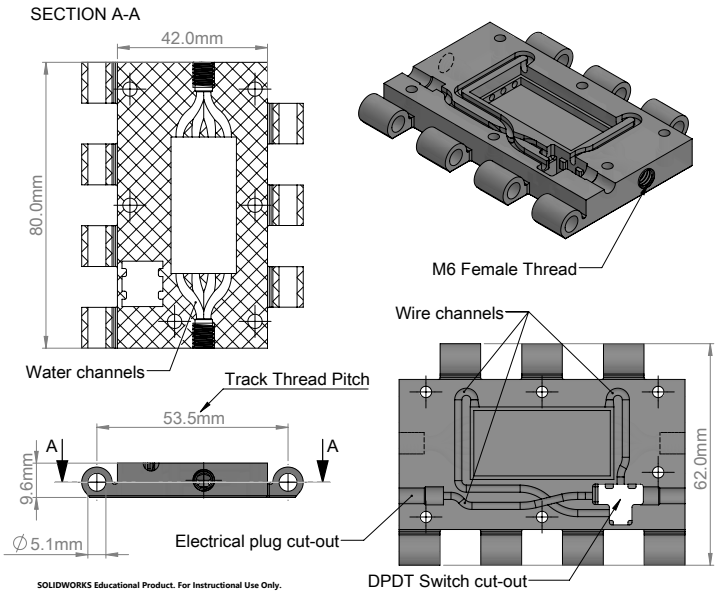

Figure 6.8: Track link bottom CAD design.

The track link bottom features channels through which the peltier wires are routed to the DPDT sliding switch. This switch is located at the underside of the track bottom. A cut-out in the track link bottom allows the wires from the connectors and peltier to be soldered to the switch.

By designing the overall shape of track link as a rectangle, the width is significantly smaller than the length. This way the track can consist of more links (compared to a square shape), and in turn helps to limit the overall height of the robot, as the track thread pitch also determines the drive sprocket diameter. Additionally, more individual track links help to create a redundancy in attachment points; in case one adhesion fails, the other links will still support the robot.

Complete Track Link

A complete and assembled track link is shown in figure 6.9.

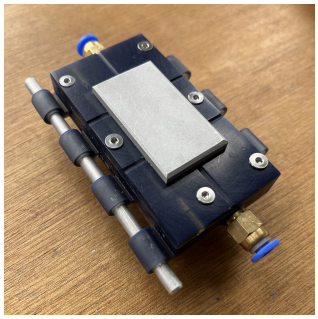

(a) Assembled adhesion pad: top.

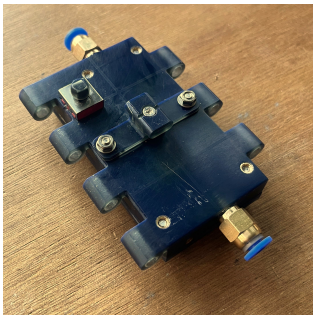

(b) Assembled adhesion pad: bottom.

Figure 6.9: Track link with integrated adhesion effector.

6.2.3. Control System

Motion Control

Controlling the movement of a single tracked vehicle is relatively straightforward because movement is limited to one direction; forward or backward. Movement speed is controlled by adjusting the rotational velocity of the motor driving the track. The rotational speed of the brushless DC motor is controlled via PWM input to the motor control board (integrated in the motor). The PWM signal has a frequency of 10 kHz at 5 V DC, and is generated by a Arduino Nano microcontroller. This microcontroller translates the input of a 10k Ohm potentiometer to the duty cycle of the PWM signal. Rotational speed is ramped up and down to the set speed to avoid rapid accelerations or jerk. A toggle switch controls the direction.

Heating and Cooling

Controlling the melt and freeze timing of each individual track link is difficult, considering the track is continuously rotating around the main body of the robot. Track links that are coming in contact with the ice should briefly melt the ice, and then be activated to cool the adhesion pad to establish an adhesive connection. Then, near the end of the track run, the connection is released by heating the adhesion pad. This sequence is illustrated in figure 6.1. By controlling the current flow direction through the peltier, either heating or cooling is established. Digitally controlling the individual links is rather complex, since the location of each individual link with respect to the robotic frame should be monitored in order to correctly time the melting-freezing-melting sequence. Such a centralized control system then also requires a means to control the current flow direction of each individual link, possibly in the form of an integrated H-bridge circuit composed of transistors or MOSFETs. Moreover, power delivery from a centralized controller further increases the complexity of such control system. While electrical slip rings are capable of transferring power through a rotating body, it is not a feasible option for systems with many track links.

Inspiration for controlling the individual track links came from an unusual source; agricultural machinery. In particular, the rotary hay rakes that are used to collect the dried hay or straw and combine them into windrows, for efficient collection by the combine or baler. As the name suggests, these machines are basically rakes moving in a circular motion, usually powered and pulled behind a tractor, as shown in figure 6.10b. While there are numerous individual rakes on a rotor, each rake is controlled individually to lift off the ground in order to deposit the collected hay at the correct position. The mechanism responsible for lifting the rake is illustrated in figure 6.10a. Essentially, the rotor is driven by the power take off shaft and rotates around the central hub, each rotor arm is fitted with a guide bearing that follows a cam track. This causes the rotor arm to rotate and lift the rake off the ground.

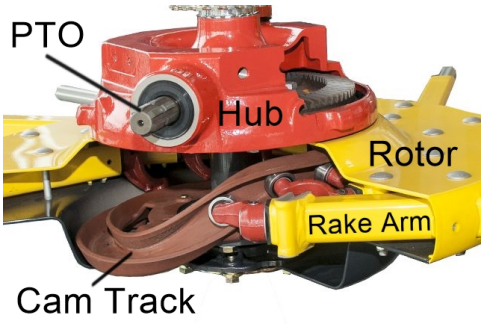

(a) Cam track mechanism of an hay rake used in agricultural settings. Image adapted from:[64]

(b) Agricultural hay rake in operation. Image from:[64]

Figure 6.10: Agricultural equipment as an inspiration source.

The movement of the ice climbing robot track is similar to the movement of the rotor, both rotate or move with respect to a central body. Each link of the track follows the same trajectory, so the location at which the track links are controlled can be defined as stationary points along this trajectory. Then, adapting the cam track follower mechanism from the hay rake to the tracked robot results in a mechanical control system that does not require any digital input. In fact, simple switches can be modified and integrated in the track links to function as H-Bridge circuits that control the current flow direction through the peltier. Figure 6.11 shows how *double pole double throw* (DPDT) switches can be wired to function as h-bridge circuits.

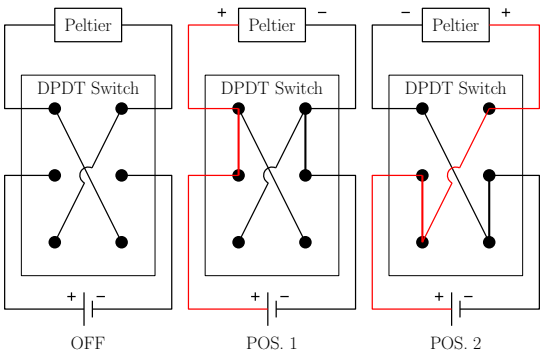

Figure 6.11: Double Pole Double Throw switch configured as H-Bridge.

Integrating these switches in the track links, and adding a cam track in the frame of the robots actuates the switch lever, will ensure the track links are activated at the correct position. The working principle is illustrated in figure 6.12a. Adjusting the position of the cam track will change the timing of the control system accordingly.

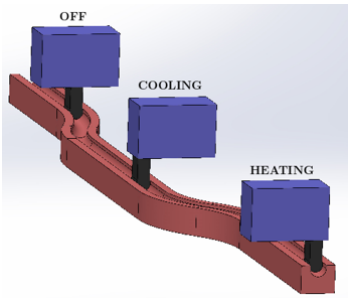

(a) Mechanical control system based on a cam follower track system.

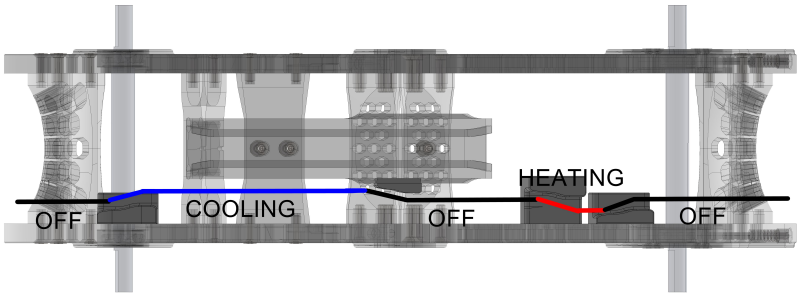

(b) Switch cam position in robot frame.

Figure 6.12: Cam track control system.

The cam track can be simplified and reduced to single points of switching, resulting in the system shown in figure 6.12b.

6.2.4. Heat Dissipation

Concept

Supplying a continuous flow of cooling water to the individual tracks is just as essential as it is complex. Similar to the challenges for controlling the individual track links, the challenge lies in the fact that the track is rotating around the body of the vehicle. Since the integration of a water cooling system in the payload of the robot was set as a design requirement, the cooling water has to be supplied from a central point in the robot.

Water Cooling and Pump

Similar to the thermoelectric cooling setup introduced in chapter 3 and used in the experiments in chapter 5, a water radiator, fan and pump are fitted inside the frame of the robot. The Laing DDC-pump 12V DDC-1T is capable of providing a water flow rate up to 10 l/min, so that all 16 track links are supplied with a flow rate of 0.625 l/min. A small 60 mm water radiator and corresponding 60 mm cooling fan are also fitted in the frame of the robot as shown in figure 6.13 Cooling rate of water cooling radiators is dependent on multiple factors such as: water flow rate, temperature difference and air flow rate.

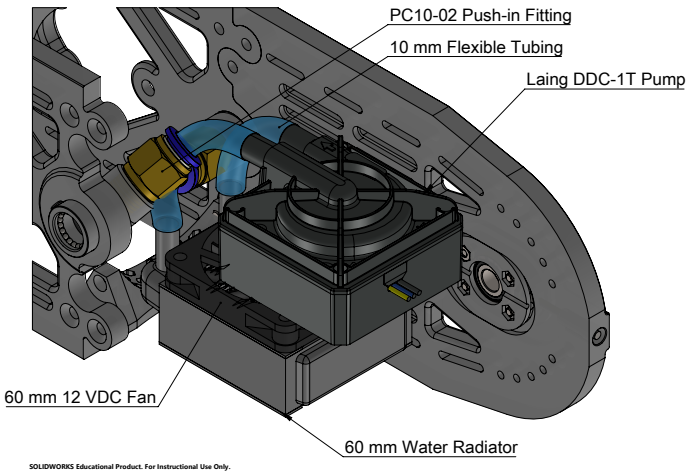

Figure 6.13: Water cooling components inside the robot frame.

Rotating Water Manifold

A water manifold can be designed to split the water flow and distribute the water to the track links. However, this water manifold should be rotate with respect to the frame of the robot in order to allow the tracks to rotate continuously. In rotating high pressure hydraulic systems this is achieved with the use of live swivels. The working principle of live swivels is integrated in the design of a water manifold. This manifold provides a water outlet for each track link, and allows the manifold to rotate with the movement of the track. Figure 6.14 shows a CAD model of the water manifold swivel. In this figure, detail *B* provides an enlarged view of the parts that enable the manifold to rotate. A rubber O-ring provides a waterproof seal between the two parts of the manifold. Small, 2 mm ball bearing can be inserted in the assembly and are held captive in the bearing race between the two parts, an M3 set screw prevents the ball bearing from falling out. These ball bearing allow the parts to rotate with respect to each other, while preventing axial movement of the parts.

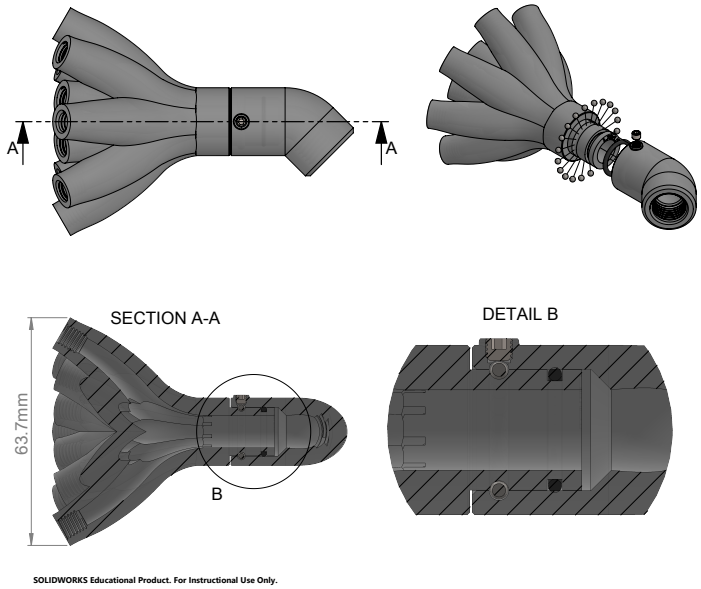

Figure 6.14: Water manifold with multiple water outlets capable of rotating.

6.2.5. Drive and Energy System

Motor Torque

The forward and backward movement of the robot is driven by a single planetary gear brushless DC motor. By considering the robot travelling in vertical direction, the motor torque required to overcome gravitational forces can be derived using the mass of the robot and radius of the drive sprocket. In equilibrium, the starting or locked rotor torque is given by: $\tau = m_{robot} g r_{sprocket}$. Where g is the gravitational acceleration, m the mass of the robot and $r_{sprocket}$ is the radius of the drive sprocket. Then, since the mass of the robot also depends on the mass of the motor, the torque is calculated for a total mass range between 3 and 6 kg. The radius of the drive sprocket is not a free parameter, but a function of the number of teeth N_{teeth} and track linkage pitch P_{link}, given by: $r_{sprocket} = \frac{P_{link}}{2\sin(\pi/N_{teeth})}$. Number of sprocket teeth is a design choice, and presents a trade-off as higher teeth numbers approach a more circular sprocket, resulting in a smoother rotation of the track. Meanwhile the radius of the sprocket also increases for higher teeth numbers at constant track linkage pitch; increasing the overall height of the robot as well. Here, a sprocket with seven teeth is chosen. Track thread link pitch is 53.5 mm, from figure 6.8. Then the torque in vertical robot orientation is calculated for a mass between 3 to 6 kg: T = 1.8 - 3.6 Nm, this is the torque acting on the shaft driving the track sprockets, any additional gear ratios between motor and drive shaft influences the torque acting on the motor.

Motor RPM

High travelling speeds is not a priority for this robotic system. Instead, the time required to establish an adhesive connection (time-to-adhere) between track link and ice is the limiting factor. Time-to-adhere is dependent on multiple factors, in no particular order: ice temperature, peltier hot side temperature (cooling water temperature and thus temperature of the environment), temperature of the adhesion pad before contacting the ice, adhesion pad material properties and power supplied to the peltier module. Optimizing these parameters would enable faster travelling speeds, but is not the priority here. Here the upper limit of the track velocity relative to the robotic frame, is approximated by setting the distance-to-adhesion, i.e. the distance the adhesion pad travels on the ice before an adhesion is established equal to the track thread length (53.5 mm), in combination with a time-to-adhere of 4 seconds, resulting in a track velocity of 13.4 mm/s. Angular velocity of the drive sprocket is then determined with $\omega_{sprocket} = v_{track}/r_{sprocket}$ and can be converted to revolutions per minute for convenience ($RPM = (\omega/2\pi) * 60$), as most motor specifications are given in revolutions per minute. Resulting in an upper limit sprocket RPM of 2.1 rev/min. The required power is given by $P = \omega * v = 0.8W$.

Motor Selection and Reduction Gear
A 12 VDC, 6.5 W, 36mm DC planetary geared Motor with an internal gear reduction of 721:1; Model NFP-GA36Y-3525 is selected for driving the track. This is a brushless dc motor with integrated control board. The motor has a rated torque of 2.75 Nm (stall torque: 9.8 Nm) at a rated speed of 6 rev/min (no load speed: 8 rev/min). The addition of a 1:3 bevel and pinion gear (15:45 teeth, module 1.0 gear) reduction is used to reduce the output speed, whilst increasing the torque. Figure 6.15 shows illustrated the drive-train assembly inside the robot.

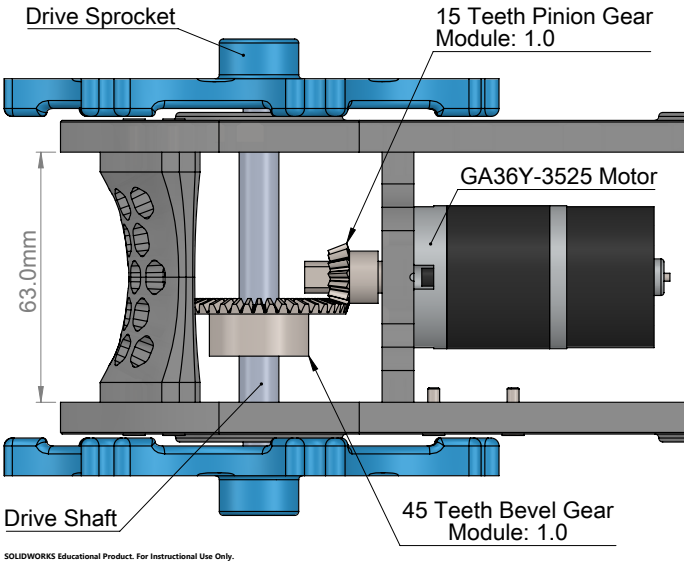

Figure 6.15: Drive system of the tracked robot.

Power Supply
The water pump, fan and motor all operate at 12 VDC, and are powered using a 3S 11.1 V 1300 mAh lithium polymer battery pack, the capacity of this battery pack is 14.4 Wh and has a mass of 115 grams. The combined power consumption of the components is 18 + 1.2 + 6 = 25.2 W, thus the battery pack is capable of powering the robotic system's drivetrain and heat dissipation system for approximately 60*(25.2/14.2)= 34 minutes.

The TEC1-6308 peltier modules are powered using a 1S2P 8800 mAh 3.8 V LiHV battery pack, with a total capacity of 33.4 Wh. This battery pack has a maximum discharge rate of 120C, making it a suitable battery for high current applications. By selecting batteries with high discharge rates, the voltage drop is limited when loads are attached. LiHV battery packs have a nominal cell voltage of 3.8 V, and a charged (100%) voltage of 4.35 V. The TEC1-6308 peltier chips draw a current of 4.5 A at a voltage of 4.35 V; power consumption of around 20 W per module. Considering a maximum of five elements are turned on simultaneously (in reality this number is lower, but five is used to increase safety), the battery pack is capable of powering the peltier elements for approximately 20 minutes.

6.2.6. Production Methods

When designing such intricate mechanical parts, it is crucial to consider production methods from the early stages of the design process. The complex geometry, scale and tolerances of the parts introduced here are particularly difficult, if not impossible, to manufacture using conventional subtractive manufacturing processes. While additive manufacturing techniques are better suited for for the production of such parts, limitations in tolerances or resolution, material type, surface finish and printer characteristics (e.g. print orientation, model support) should be considered. For these parts, an Elegoo Saturn mSLA 3D printer is modified with custom firmware and retrofitted with a small heater in order to increase print quality, specifically for the production of these parts. By creating a mixture of two different photosensitive resin materials, a trade-off between material strength and print accuracy is established. A mixing ratio of 85% SirayaTech Blu V3 and 15% SirayaTech Build with the addition of dark pigment was found to be effective for producing the parts with sufficient tolerances and durability. SirayaTech Blu V3 is suitable

for functional parts subjected to stress and deformation, but has poor dimensional accuracy as it is highly susceptible to cross-layer curing. Like most 3D printing resins, the brittle nature of SirayaTech Build makes it less suitable for functional parts. However, the dimensional accuracy and printing properties are excellent; cross-layer curing is non existent and the low viscosity reduces print deformations caused by high stresses on the printer frame.

6.3. Demonstration

The robotic system is tested on a sheet of ice 60x40x5 cm in size, this block of ice is placed in a freezer and cooled to -15°C. This block is placed at different angles to test the robot's ability to scale inclined ice surfaces. So far, the robot is able to climb the sheet of ice at a 60°incline, as depicted in figure 6.16. At steeper angles, the oncoming track links fail to make proper contact with the ice, as the weight of the robot causes the robot to tilt backwards slightly.

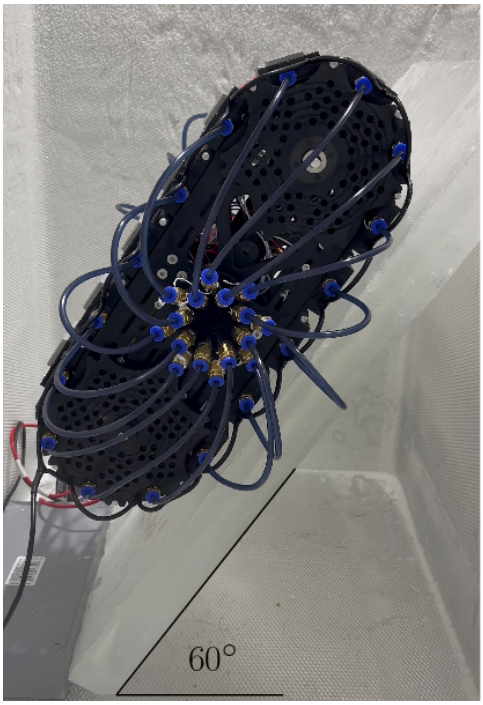

Figure 6.16: Robot climbing a sheet of ice with 60°incline.

Additional tests show that once the robot has established adhesive contact points with the ice, the robot can be inverted, and hang upside-down from the sheet of ice, as illustrated in figure 6.17.

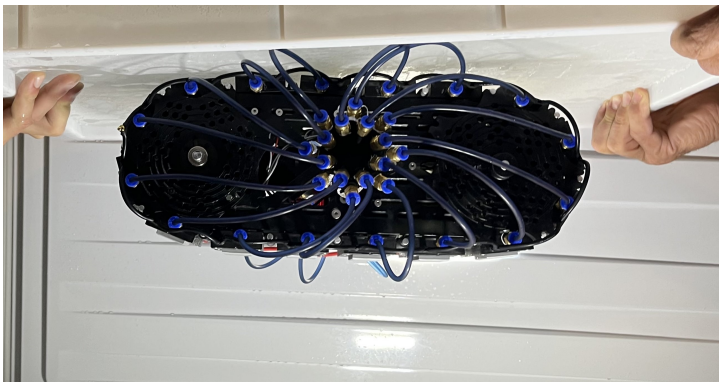

Figure 6.17: Robot inverted and anchored to a sheet of ice.

6.4. Discussion & Conclusion

In conclusion, this chapter presented the development of a robotic system with integrated ice adhesion effectors and a heat dissipation system. The robotic system serves as a proof-of-concept, showcasing one of the many possible embodiments of ice adhesion climbing robots. The design requirements, including a maximum mass of 5 kg, integration of the heat dissipation system, ability to support itself, and operation in temperatures down to -15°C, were successfully met.

The proposed robotic system utilizes tracked locomotion; the modular track design allows for the integration of multiple adhesion effectors, creating rigid anchor points for climbing on icy surfaces. The robotic system's frame design accommodates the track and provides features such as adjustable cam tracks and a track guide rail.

The track links of the robotic system are designed to incorporate various components, including peltier modules for cooling and heating, heat sinks for heat dissipation, water cooling channels, and modified DPDT switches for the mechanical control system.

The rotational speed of the motor driving the track is controlled via PWM input, allowing for adjustable forward or backward movement. The timing of melting and freezing of the adhesion pads is coordinated with the rotation of the track through an adjustable cam track mechanism, ensuring proper adhesion timing and release.

Demonstrations have shown that the robot is capable of climbing inclined icy surfaces angled up to 60°. This result represents a significant step towards realizing ice adhesion climbing robots and provides a foundation for further research and development. Thus far, the robot has been tested on a small sheet of ice, and a dedicated test site in a controlled environment is an important step to further evaluate the performance of the robot and components.

7

Conclusion & Recommendation

The call for new technologies that enable the exploration of icy moons was answered with an unexpected source of inspiration; the working principles behind a tongue stuck to a metal pole. This project explored the possibility to use ice adhesion as a benefit, rather than a nuisance. Multiple steps were taken in order to evaluate feasibility of using ice adhesion as a locomotion strategy, these steps are discussed in the following section.

7.1. Summary of Findings

7.1.1. Switchable Ice Adhesion Effector

The first step was the development of a switchable ice adhesion effector that was used to test the ice adhesion strength of various materials, in combination with the effect of melting and re-freezing the ice to the substrate materials. The key component of this effector is the implementation of the peltier effect, that enables the effector to heat and cool the adhesion pad in limited time. Peltier elements are very well suited to be integrated in switchable ice adhesion effectors due to their compact size, light weight construction and lack of moving parts. But proper heat dissipation measures showed to be an essential part for the effectiveness of the peltier elements, with liquid cooling systems being the most effective.

7.1.2. Material Selection for Ice Adhesion

This research identified multiple intrinsic and extrinsic material properties that should be considered when selecting substrate materials for the implementation of a switchable ice adhesion effector. Surface energy, closely related to wettability, aids in the intrinsic ice adhesion strength between substate and adhesive (ice). Highly elastic materials should be avoided, as the adhesion can prematurely fail due to the stress concentrations from the peeling effect. Thermal properties are also found to be important material properties, as the substrate material needs to be able to quickly change temperature to achieve an adhesive connection in the least amount of time. Materials with high thermal diffusivity and low volumetric heat capacity are therefore preferred. Copper and aluminium were selected as suitable material properties. Copper has a higher thermal diffusivity compared to aluminium, but the volumetric heat capacity of aluminium is lower compared to copper. Temperature response tests of both materials indicate that the aluminium adhesion pad reaches sub-zero temperatures $\sim$23% faster than the copper adhesion pad, when cooled with the thermo-electric cooling system. Three surface treatments were proposed to test the influence of surface roughness and contact area in ice adhesion strength: polished, grit-blasted, and a machined grid-pattern surface. The treatments result in surfaces with increasing roughness.

7.1.3. Ice Adhesion Strength Experiments

The switchable ice adhesion effector, in combination with the two substrate materials and three surface treatments was tested in terms of ice adhesion strength in a tensile pull-off experiments. Tests were performed in a temperature controlled environment at -15°C. These tests indicate that an aluminium substrate material with grit-blasted surface treatments results in the highest average adhesion strength (1.515 MPa). Meanwhile, most tests resulted in a predominantly cohesive fracture of the ice; the

adhesive strength of the effector surpassing the cohesive strength of the ice. The lowest average adhesion strength was found using a copper adhesion pad with grid-pattern surface (1.026 MPa). These results indicate that the ice adhesion strategy can provide plentiful anchoring strength for robotic systems that are sized appropriately. The ice adhesion tests are performed in a controlled environment and in pure tensile direction, more experiments that employ different load cases (shear and/or bending) are most relevant for further testing limits of ice adhesion for robotic systems.

7.1.4. Ice Climbing Robot: FLICK

FLICK is the result of a system integration process that combines all crucial components required for an ice adhesion locomotion strategy. The robotic system uses a tracked locomotion principle in combination with ice adhesion effectors integrated in the track links, to enable climbing on icy surfaces at steep angles. The heat dissipation system was succesfully miniaturized and integrated in the payload of the robot. A rotating water manifold ensures the individual track links are continuously supplied with cooling water during operation. The mechanical control system ensures the track links are switched to heating or cooling at certain points on the frame, so that oncoming track links seize the ice at the beginning of the track run, and release the ice at the end of the track run. By making these points adjustable, the timing can be adapted to the working conditions, such as travelling speed and ambient temperature. Tests show that FLICK is capable of climbing on icy surfaces at angles up to 60°. As well as supporting its own weight through ice adhesion using the track links, hanging upside-down from a block of ice.

7.2. Recommendations for Future Research

7.2.1. Ice Adhesion Experiments

Load Cases

The ice adhesion strength experiments in this research determined the ice adhesion strength in pure tensile direction. While this gives a good approximation and comparison of the adhesion strength of various materials and surface treatments, a robotic system would rarely load the adhesive anchor points in pure tensile direction; a combination of tensile, shear and bending can be expected. Testing the adhesion strength for these load cases are therefore most certainly relevant to further quantify the limits of ice adhesion for robotic system. That way, robotic systems can be designed to operate more towards the limits of the ice adhesion effector.

Low Pressure

The developed ice adhesion effector relies heavily on the phase transformation of water between liquid and solid. For terrestrial conditions, or more specifically, in Earth's atmospheric pressure (101 kPa) this transformation is trivial. However, on the surface of Saturn's icy moon Enceladus, the pressure is much lower. In fact, the pressure is near vacuum. Then, heating ice at that pressure would most likely result in sublimation (from solid to gas phase), rather than melting to liquid water. Testing the ice adhesion effector in near vacuum conditions is therefore an important step for the development of ice adhesion strategies on icy moons. Possible solutions for this issue might include using the back pressure from sublimation to locally raise the pressure, such that liquid water can form.

Varying Ice Quality

The ice adhesion strength of the adhesion effector was determined in a highly controlled environment, with good quality ice. But in reality, the ice quality might not always be guaranteed. Tests with varying ice quality are essential to better understand the limits of the ice adhesion effector.

7.2.2. Adhesion Effector

Heat Dissipation Methods

While the liquid heat dissipation system proves to be an effective method to dissipate the waste heat from the peltier elements, supplying the cooling water to the adhesion effector in a robotic system can be difficult. Additionally, the components required to cool the liquid (e.g. radiator, fan and pump) can be difficult to integrate in robotic systems. Further investigation of passive heat dissipation systems can be worthwhile. Solutions might include, but are not limited to: using phase change materials, or using the cold melt water produced when the adhesion pad melts the ice for cooling the peltier.

Adhesion Pad Design
Here, a basic adhesion pad was presented with three different surface treatments. In case these adhesion pads do not provide enough anchoring force in low density hoarfrost ice, adhesion pads that have more penetration in the low density ice might be beneficial.

7.2.3. Robotic System Development

Improve Mobility
FLICK, the single track robotic system developed here was developed as a proof-of-concept for an ice climbing robot that uses the effect of ice adhesion for locomotion. The mobility of this robotic system is limited to 1-DOF. Still, this concept is well suited for modular robotic systems. An advanced example of robotic systems based on tracked locomotion for high mobility climbing capabilities is displayed in figure 7.1.

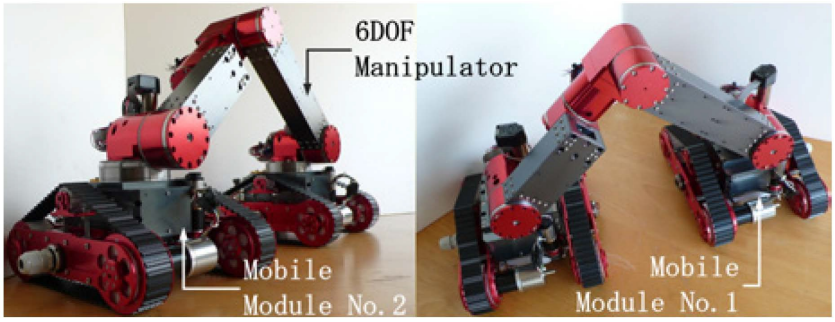

Figure 7.1: Reconfigurable wall climbing robot with 6-DOF manipulator. Image from: [39]

This system is developed by Lee W. [39] and features a 6-DOF manipulator that connects two tracked vehicles to increase mobility and allows the robot to traverse obstacles and sharp transitions.

Alternatively, adapting different locomotion strategies, such as legged locomotion, to an ice adhesion method can produce a systems with higher mobility.

Dedicated Test Location
Testing FLICK was mostly done in a standard freezer, which does not accommodate large blocks of ice very well. A proper test location, such as a walk-in-freezer is important to test the reliability of the robotic system in when travelling longer distances. And should also help evaluate the performance of the miniaturized heat dissipation system.

Test on Location: Glaciers
Similar to a necessity of a dedicated test location, testing future prototypes should also include testing the system in real-world situations, such as glaciers, ice caves and or crevasses.

Payload Design: Instruments to find life
Considering the proposed application of the ice climbing robot: exploring Enceladus' crevasses to detect life, it is important to develop systems that can be integrated in the ice climbing robot that are capable of performing the measurements required to find life. Development of such systems should be simultaneous to the development of the robotic system, so that design requirements of both systems can be adjusted accordingly.

Guidance, Navigation and Control (GNC)
Controlling the robot on remote locations is not always possible. In the case of Enceladus, manual control of an exploration robot is simply impossible. Therefore, systems capable of autonomous operation are a necessity. These systems should also be developed simultaneous to the development of the robotic systems, to ensure that the sensors, control systems and actuators are well integrated.

References

[1] E. H. Andrews and N. A. Lockington. “The cohesive and adhesive strength of ice”. In: *Journal of Materials Science 1983 18:5* 18.5 (May 1983), pp. 1455–1465. ISSN: 1573-4803. DOI: 10.1007/BF01111965. URL: https://link-springer-com.tudelft.idm.oclc.org/article/10.1007/BF01111965.

[2] Takeshi Aoyama et al. “Effect of Surface Roughness on Adhesive Shear Strength between Pure Ice and a Solid Surface”. In: *TRACE* 23.3 (2011), pp. 273–281. URL: https://ui.adsabs.harvard.edu/abs/2011TRACE..23..273A/abstract.

[3] Yosef Ashkenazy. “The surface temperature of Europa”. In: *Heliyon* 5.6 (June 2019), e01908. ISSN: 24058440. DOI: 10.1016/j.heliyon.2019.e01908. URL: https://linkinghub.elsevier.com/retrieve/pii/S2405844018357724.

[4] Ian Frank Bainbridge and John Andrew Taylor. “The surface tension of pure aluminum and aluminum alloys”. In: *Metallurgical and Materials Transactions A: Physical Metallurgy and Materials Science* 44.8 (Aug. 2013), pp. 3901–3909. ISSN: 10735623. DOI: 10.1007/S11661-013-1696-9/TABLES/3. URL: https://link-springer-com.tudelft.idm.oclc.org/article/10.1007/s11661-013-1696-9.

[5] Marie Behounkova et al. “Plume Activity and Tidal Deformation on Enceladus Influenced by Faults and Variable Ice Shell Thickness”. In: *Astrobiology* 17.9 (Sept. 2017), p. 941. ISSN: 15311074. DOI: 10.1089/AST.2016.1629. URL: /pmc/articles/PMC5610426/%20/pmc/articles/PMC5610426/?report=abstract%20https://www-ncbi-nlm-nih-gov.tudelft.idm.oclc.org/pmc/articles/PMC5610426/.

[6] Robert H. Brown et al. “Composition and Physical Properties of Enceladus’ Surface”. In: *Science* 311.5766 (Mar. 2006), pp. 1425–1428. ISSN: 0036-8075. DOI: 10.1126/science.1121031. URL: https://www.science.org/doi/10.1126/science.1121031.

[7] Kalind Carpenter et al. “Exobiology Extant Life Surveyor (EELS)”. In: *Earth and Space 2021*. Reston, VA: American Society of Civil Engineers, Apr. 2021, pp. 328–338. ISBN: 9780784483374. DOI: 10.1061/9780784483374.033. URL: http://ascelibrary.org/doi/10.1061/9780784483374.033.

[8] Jing Chen et al. “Superhydrophobic surfaces cannot reduce ice adhesion”. In: *Applied Physics Letters* 101.11 (Sept. 2012), p. 111603. ISSN: 0003-6951. DOI: 10.1063/1.4752436. URL: https://aip-scitation-org.tudelft.idm.oclc.org/doi/abs/10.1063/1.4752436.

[9] C. F. Chyba and C. B. Phillips. “Possible ecosystems and the search for life on Europa”. In: *Proceedings of the National Academy of Sciences* 98.3 (Jan. 2001), pp. 801–804. ISSN: 0027-8424. DOI: 10.1073/pnas.98.3.801. URL: http://www.pnas.org/cgi/doi/10.1073/pnas.98.3.801.

[10] *Composite Infrared Spectrometer (CIRS) | Cassini Orbiter – NASA Solar System Exploration*. URL: https://solarsystem.nasa.gov/missions/cassini/mission/spacecraft/cassini-orbiter/composite-infrared-spectrometer/.

[11] OriginLab Corporation. *Phase Diagram of Water*. URL: https://www.originlab.com/www/products/GraphGallery.aspx?GID=621.

[12] Aaron Curtis, Matt Martone, and Aaron Parness. “Roving on ice: Field testing an Ice Screw End Effector and sample collection tool”. In: *IEEE Aerospace Conference Proceedings* 2018-March (June 2018), pp. 1–17. ISSN: 1095323X. DOI: 10.1109/AERO.2018.8396715.

[13] Aaron Curtis et al. “IceWorm: Ice Climbing Robots for Glaciology and Beyond”. In: 2018.

[14] Bernd Dachwald et al. “IceMole: a maneuverable probe for clean in situ analysis and sampling of subsurface ice and subglacial aquatic ecosystems”. In: *Annals of Glaciology* 55.65 (Sept. 2014), pp. 14–22. ISSN: 0260-3055. DOI: 10.3189/2014AOG65A004. URL: https://www-cambridge-org.tudelft.idm.oclc.org/core/journals/annals-of-glaciology/article/icemole-a-maneuverable-probe-for-clean-in-situ-analysis-and-sampling-of-subsurface-ice-and-subglacial-aquatic-ecosystems/A5174FD249A0CB4E8DFBE7B1935E1765.

[15] Bernd Dachwald et al. “Key Technologies and Instrumentation for Subsurface Exploration of Ocean Worlds”. In: *Space Science Reviews* 216.5 (Aug. 2020), p. 83. ISSN: 0038-6308. DOI: 10.1007/s11214-020-00707-5. URL: https://link.springer.com/10.1007/s11214-020-00707-5.

[16] Yongbo Deng et al. “Inversely designed micro-textures for robust Cassie–Baxter mode of superhydrophobicity”. In: *Computer Methods in Applied Mechanics and Engineering* 341 (Nov. 2018), pp. 113–132. ISSN: 0045-7825. DOI: 10.1016/J.CMA.2018.06.034.

[17] Y. Dong, T. W. Hill, and S.-Y. Ye. “Characteristics of ice grains in the Enceladus plume from Cassini observations”. In: *Journal of Geophysical Research: Space Physics* 120.2 (Feb. 2015), pp. 915–937. ISSN: 21699380. DOI: 10.1002/2014JA020288. URL: http://doi.wiley.com/10.1002/2014JA020288.

[18] M. K. Dougherty et al. “Identification of a dynamic atmosphere at Enceladus with the Cassini magnetometer”. In: *Science (New York, N.Y.)* 311.5766 (Mar. 2006), pp. 1406–1409. ISSN: 1095-9203. DOI: 10.1126/SCIENCE.1120985. URL: https://pubmed-ncbi-nlm-nih-gov.tudelft.idm.oclc.org/16527966/.

[19] Younes Ezzahri and Ali Shakouri. “Solid-state microrefrigeration in conjonction with liquid cooling”. In: *2008 2nd International Conference on Thermal Issues in Emerging Technologies, ThETA 2008* (2008), pp. 15–24. DOI: 10.1109/THETA.2008.5167156.

[20] B Giese et al. “The morphology of an active zone near Enceladus’ south pole and implications”. In: *Geophysical Research Abstracts*. 2010. URL: https://elib.dlr.de/64103/.

[21] Frederic Guerin et al. “Analytical model based on experimental data of centrifuge ice adhesion tests with different substrates”. In: *Cold Regions Science and Technology* 121 (Jan. 2016), pp. 93–99. ISSN: 0165-232X. DOI: 10.1016/J.COLDREGIONS.2015.10.011.

[22] P. K. Haff, A. Eviatar, and G. L. Siscoe. “Ring and plasma: The enigmae of Enceladus”. In: *Icarus* 56.3 (Dec. 1983), pp. 426–438. ISSN: 0019-1035. DOI: 10.1016/0019-1035(83)90164-1.

[23] Yong Han et al. “Surface energies, adhesion energies, and exfoliation energies relevant to copper-graphene and copper-graphite systems”. In: *Surface Science* 685 (July 2019), pp. 48–58. ISSN: 0039-6028. DOI: 10.1016/J.SUSC.2019.01.009.

[24] C. J. Hansen et al. “Investigation of diurnal variability of water vapor in Enceladus’ plume by the Cassini ultraviolet imaging spectrograph”. In: *Geophysical Research Letters* 44.2 (Jan. 2017), pp. 672–677. ISSN: 0094-8276. DOI: 10.1002/2016GL071853. URL: https://onlinelibrary.wiley.com/doi/abs/10.1002/2016GL071853.

[25] Candice J. Hansen et al. “Enceladus’ Water Vapor Plume”. In: *Science* 311.5766 (Mar. 2006), pp. 1422–1425. ISSN: 0036-8075. DOI: 10.1126/science.1121254. URL: https://www.science.org/doi/10.1126/science.1121254.

[26] M. M. Hedman et al. “An observed correlation between plume activity and tidal stresses on Enceladus”. In: *Nature* 500.7461 (Aug. 2013), pp. 182–184. ISSN: 0028-0836. DOI: 10.1038/nature12371. URL: http://www.nature.com/articles/nature12371.

[27] C. J. A. Howett et al. “High heat flow from Enceladus’ south polar region measured using 10-600 cm-1 Cassini/CIRS data”. In: *Journal of Geophysical Research* 116.E3 (Mar. 2011), E03003. ISSN: 0148-0227. DOI: 10.1029/2010JE003718. URL: http://doi.wiley.com/10.1029/2010JE003718.

[28] C. J.A. Howett et al. “Thermal inertia and bolometric Bond albedo values for Mimas, Enceladus, Tethys, Dione, Rhea and Iapetus as derived from Cassini/CIRS measurements”. In: *Icarus* 206.2 (Apr. 2010), pp. 573–593. ISSN: 0019-1035. DOI: 10.1016/J.ICARUS.2009.07.016.

[29] *Images of Saturn and All Available Satellites*. URL: https://photojournal.jpl.nasa.gov/targetFamily/Saturn.

[30] Andrew P. Ingersoll and Shawn P. Ewald. “Total particulate mass in Enceladus plumes and mass of Saturn’s E ring inferred from Cassini ISS images”. In: *Icarus* 216.2 (Dec. 2011), pp. 492–506. ISSN: 00191035. DOI: 10.1016/j.icarus.2011.09.018. URL: https://linkinghub.elsevier.com/retrieve/pii/S0019103511003708.

[31] H.H.G Jellinek. “Adhesive properties of ice”. In: *Journal of Colloid Science* 14.3 (June 1959), pp. 268–280. ISSN: 00958522. DOI: 10.1016/0095-8522(59)90051-0. URL: https://linkinghub.elsevier.com/retrieve/pii/0095852259900510.

[32] D. H. Kaelble. “Dispersion-Polar Surface Tension Properties of Organic Solids”. In: *https://doi-org.tudelft.idm.oclc.org/10.1080/0021846708544582* 2.2 (Apr. 2008), pp. 66–81. ISSN: 15455823. DOI: 10.1080/0021846708544582. URL: https://www-tandfonline-com.tudelft.idm.oclc.org/doi/abs/10.1080/0021846708544582.

[33] S. Kempf et al. “Saturn’s Diffuse E Ring and Its Connection with Enceladus”. In: *Enceladus and the Icy Moons of Saturn*. The University of Arizona Press, 2018, p. 195. DOI: 10.2458/azu{_}uapress{_}9780816537075-ch010. URL: https://uapress.arizona.edu/book/enceladus-and-the-icy-moons-of-saturn.

[34] Edwin S. Kite and Allan M. Rubin. “Sustained eruptions on Enceladus explained by turbulent dissipation in tiger stripes”. In: *Proceedings of the National Academy of Sciences* 113.15 (Apr. 2016), pp. 3972–3975. ISSN: 0027-8424. DOI: 10.1073/pnas.1520507113. URL: http://www.pnas.org/lookup/doi/10.1073/pnas.1520507113.

[35] Anna Kochan. “European project develops ”ice” gripper for micro-sized components”. In: *Assembly Automation* 17.2 (1997), pp. 114–115. ISSN: 01445154. DOI: 10.1108/01445159710171310/FULL/PDF.

[36] Konstantinos Konstantinidis et al. “A lander mission to probe subglacial water on Saturns moon Enceladus for life”. In: *Acta Astronautica* 106 (Jan. 2015), pp. 63–89. ISSN: 00945765. DOI: 10.1016/j.actaastro.2014.09.012. URL: https://linkinghub.elsevier.com/retrieve/pii/S0094576514003610.

[37] Kostas Konstantinidis et al. “Simulation of precise and safe landing near a plume source on Enceladus”. In: *IEEE Aerospace Conference Proceedings* 2018-March (June 2018), pp. 1–15. ISSN: 1095323X. DOI: 10.1109/AERO.2018.8396476.

[38] K. J. Kubiak et al. “Wettability versus roughness of engineering surfaces”. In: *Wear* 271.3-4 (June 2011), pp. 523–528. ISSN: 0043-1648. DOI: 10.1016/J.WEAR.2010.03.029.

[39] Woosub Lee. “Proposition of reconfigurable wall climbing robot using 6DOF force torque sensor based on flexible structure for real environment”. In: *2013 13th International Conference on Control, Automation and Systems (ICCAS 2013)*. IEEE, Oct. 2013, pp. 1802–1806. ISBN: 978-89-93215-05-2. DOI: 10.1109/ICCAS.2013.6704232. URL: http://ieeexplore.ieee.org/document/6704232/.

[40] Edwin Jee Yang Ling et al. “Reducing Ice Adhesion on Nonsmooth Metallic Surfaces: Wettability and Topography Effects”. In: *ACS applied materials & interfaces* 8.13 (Apr. 2016), pp. 8789–8800. ISSN: 1944-8252. DOI: 10.1021/ACSAMI.6B00187. URL: https://pubmed-ncbi-nlm-nih-gov.tudelft.idm.oclc.org/26953827/.

[41] G. Lipp et al. “Investigation of the behavior of dissolved gases during freezing”. In: *Cryobiology* 24.6 (Dec. 1987), pp. 489–503. ISSN: 0011-2240. DOI: 10.1016/0011-2240(87)90053-8.

[42] Jing Liu, Yi Xin Zhou, and Tian Hua Yu. “Freeze tweezer to manipulate mini/micro objects”. In: *Journal of Micromechanics and Microengineering* 14.2 (Nov. 2003), p. 269. ISSN: 0960-1317. DOI: 10.1088/0960-1317/14/2/015. URL: https://iopscience-iop-org.tudelft.idm.oclc.org/article/10.1088/0960-1317/14/2/015%20https://iopscience-iop-org.tudelft.idm.oclc.org/article/10.1088/0960-1317/14/2/015/meta.

[43] Lili Liu et al. “A Superstrong and Reversible Ionic Crystal□Based Adhesive Inspired by Ice Adhesion”. In: *Angewandte Chemie* 133.16 (Apr. 2021), pp. 9030–9041. ISSN: 0044-8249. DOI: 10.1002/ange.202100984. URL: https://onlinelibrary.wiley.com/doi/10.1002/ange.202100984.

[44] Shannon M. MacKenzie et al. “The Enceladus Orbilander Mission Concept: Balancing Return and Resources in the Search for Life”. In: *The Planetary Science Journal* 2.2 (Apr. 2021), p. 77. ISSN: 2632-3338. DOI: 10.3847/PSJ/abe4da. URL: https://iopscience.iop.org/article/10.3847/PSJ/abe4da.

[45] Lasse Makkonen. “Ice Adhesion —Theory, Measurements and Countermeasures”. In: *Journal of Adhesion Science and Technology* 26.4-5 (Mar. 2012), pp. 413–445. ISSN: 0169-4243. DOI: 10.1163/016942411X574583. URL: https://www.tandfonline.com/doi/full/10.1163/016942411X574583.

[46] Hilary R. Martens et al. “Spatial distribution of ice blocks on Enceladus and implications for their origin and emplacement”. In: *Icarus* 245 (Jan. 2015), pp. 162–176. ISSN: 0019-1035. DOI: 10.1016/J.ICARUS.2014.09.035.

[47] Dennis L. Matson et al. “Enceladus: A hypothesis for bringing both heat and chemicals to the surface”. In: *Icarus* 221.1 (Sept. 2012), pp. 53–62. ISSN: 0019-1035. DOI: 10.1016/J.ICARUS.2012.05.031.

[48] Dennis L. Matson et al. “Enceladus’ near-surface CO2 gas pockets and surface frost deposits”. In: *Icarus* 302 (Mar. 2018), pp. 18–26. ISSN: 00191035. DOI: 10.1016/j.icarus.2017.10.025. URL: https://linkinghub.elsevier.com/retrieve/pii/S0019103517302506.

[49] Christopher P. McKay et al. “The Possible Origin and Persistence of Life on Enceladus and Detection of Biomarkers in the Plume”. In: *Astrobiology* 8.5 (Oct. 2008), pp. 909–919. ISSN: 1531-1074. DOI: 10.1089/ast.2008.0265. URL: http://www.liebertpub.com/doi/10.1089/ast.2008.0265.

[50] Halar Memon et al. “Intrinsic dependence of ice adhesion strength on surface roughness”. In: *Surface and Coatings Technology* 385 (Mar. 2020), p. 125382. ISSN: 0257-8972. DOI: 10.1016/J.SURFCOAT.2020.125382.

[51] Kiana Mirshahidi et al. “A high throughput tensile ice adhesion measurement system”. In: *HardwareX* 8 (Oct. 2020), e00146. ISSN: 2468-0672. DOI: 10.1016/J.OHX.2020.E00146.

[52] Miki Nakajima and Andrew P. Ingersoll. “Controlled boiling on Enceladus. 1. Model of the vapor-driven jets”. In: *Icarus* 272 (July 2016), pp. 309–318. ISSN: 00191035. DOI: 10.1016/j.icarus.2016.02.027. URL: https://linkinghub.elsevier.com/retrieve/pii/S0019103516000968.

[53] *New names for Enceladus’ features | The Planetary Society*. URL: https://www.planetary.org/articles/0769.

[54] F. Nimmo et al. “Shear heating as the origin of the plumes and heat flux on Enceladus”. In: *Nature* 447.7142 (May 2007), pp. 289–291. ISSN: 0028-0836. DOI: 10.1038/nature05783. URL: http://www.nature.com/articles/nature05783.

[55] Michael Nosonovsky and Vahid Hejazi. “Why superhydrophobic surfaces are not always icephobic”. In: *ACS Nano* 6.10 (Oct. 2012), pp. 8488–8491. ISSN: 19360851. DOI: 10.1021/NN302138R/ASSET/IMAGES/LARGE/NN-2012-02138R{_}0003.JPEG. URL: https://pubs-acs-org.tudelft.idm.oclc.org/doi/full/10.1021/nn302138r.

[56] Masahiro Ono et al. “Enceladus Vent Explorer Concept”. In: *Outer Solar System*. Cham: Springer International Publishing, Apr. 2018, pp. 665–717. DOI: 10.1007/978-3-319-73845-1{_}13. URL: http://link.springer.com/10.1007/978-3-319-73845-1_13.

[57] Victor F. Petrenko and Suogen Qi. “Reduction of ice adhesion to stainless steel by ice electrolysis”. In: *Journal of Applied Physics* 86.10 (Nov. 1999), pp. 5450–5454. ISSN: 0021-8979. DOI: 10.1063/1.371544. URL: /aip/jap/article/86/10/5450/490776/Reduction-of-ice-adhesion-to-stainless-steel-by.

[58] J. J. Petrovic. “Mechanical properties of ice and snow”. In: *Journal of Materials Science* 38.1 (Jan. 2003), pp. 1–6. ISSN: 00222461. DOI: 10.1023/A:1021134128038/METRICS. URL: https://link-springer-com.tudelft.idm.oclc.org/article/10.1023/A:1021134128038.

[59] C. C. Porco et al. “Cassini observes the active south pole of Enceladus”. In: *Science (New York, N.Y.)* 311.5766 (Mar. 2006), pp. 1393–1401. ISSN: 1095-9203. DOI: 10.1126/SCIENCE.1123013. URL: https://pubmed-ncbi-nlm-nih-gov.tudelft.idm.oclc.org/16527964/.

[60] Carolyn Porco, Daiana DiNino, and Francis Nimmo. “HOW THE GEYSERS, TIDAL STRESSES, AND THERMAL EMISSION ACROSS THE SOUTH POLAR TERRAIN OF ENCELADUS ARE RELATED”. In: *The Astronomical Journal* 148.3 (July 2014), p. 45. ISSN: 0004-6256. DOI: 10.1088/0004-6256/148/3/45. URL: https://iopscience.iop.org/article/10.1088/0004-6256/148/3/45.

[61] F. Postberg et al. “A salt-water reservoir as the source of a compositionally stratified plume on Enceladus”. In: *Nature* 474.7353 (June 2011), pp. 620–622. ISSN: 0028-0836. DOI: 10.1038/nature10175. URL: http://www.nature.com/articles/nature10175.

[62] F. Postberg et al. “Plume and Surface Composition of Enceladus”. In: *Enceladus and the Icy Moons of Saturn*. The University of Arizona Press, 2018, pp. 129–162. DOI: 10.2458/azu{_}uapress{_}9780816537075-ch007. URL: https://uapress.arizona.edu/book/enceladus-and-the-icy-moons-of-saturn.

[63] F. Postberg et al. “Sodium salts in E-ring ice grains from an ocean below the surface of Enceladus”. In: *Nature* 459.7250 (June 2009), pp. 1098–1101. ISSN: 0028-0836. DOI: 10.1038/nature08046. URL: http://www.nature.com/articles/nature08046.

[64] Pottinger. *Swathing Rake*. URL: www.poettinger.at.

[65] Florian Richter et al. “ARCSnake: Reconfigurable Snake-Like Robot with Archimedean Screw Propulsion for Multi-Domain Mobility”. In: *IEEE Transactions on Robotics* (July 2021). URL: http://arxiv.org/abs/2107.14427.

[66] S. B. Riffat and Xiaoli Ma. “Improving the coefficient of performance of thermoelectric cooling systems: A review”. In: *International Journal of Energy Research* 28.9 (July 2004), pp. 753–768. ISSN: 0363907X. DOI: 10.1002/ER.991.

[67] Sigrid Rønneberg, Jianying He, and Zhiliang Zhang. “The need for standards in low ice adhesion surface research: a critical review”. In: *Journal of Adhesion Science and Technology* 34.3 (Feb. 2020), pp. 319–347. ISSN: 0169-4243. DOI: 10.1080/01694243.2019.1679523. URL: https://www.tandfonline.com/doi/full/10.1080/01694243.2019.1679523.

[68] Sigrid Rønneberg et al. “The effect of ice type on ice adhesion”. In: *AIP Advances* 9.5 (May 2019), p. 055304. ISSN: 21583226. DOI: 10.1063/1.5086242. URL: https://aip-scitation-org.tudelft.idm.oclc.org/doi/abs/10.1063/1.5086242.

[69] Changhai Ru et al. “A new ice gripper based on thermoelectric effect for manipulating micro objects”. In: *2007 7th IEEE International Conference on Nanotechnology - IEEE-NANO 2007, Proceedings* (2007), pp. 438–441. DOI: 10.1109/NANO.2007.4601227.

[70] Anna Rudawska et al. “The effect of sandblasting on surface properties for adhesion”. In: *International Journal of Adhesion and Adhesives* 70 (Oct. 2016), pp. 176–190. ISSN: 0143-7496. DOI: 10.1016/J.IJADHADH.2016.06.010.

[71] Ivan A. Ryzhkin and Victor F. Petrenko. “Physical mechanisms responsible for ice adhesion”. In: *Journal of Physical Chemistry B* 101.32 (Aug. 1997), pp. 6267–6270. ISSN: 15206106. DOI: 10.1021/JP9632145/ASSET/IMAGES/MEDIUM/JP9632145E00009.GIF. URL: https://pubs-acs-org.tudelft.idm.oclc.org/doi/full/10.1021/jp9632145.

[72] B.C. Sales. “Thermoelectric Devices: Refrigeration and Power Generations With No Moving Parts”. In: *Encyclopedia of Materials: Science and Technology* (2001), pp. 9179–9185. DOI: 10.1016/B0-08-043152-6/01655-7. URL: https://www.researchgate.net/publication/290282373_Thermoelectric_Devices_Refrigeration_and_Power_Generations_With_No_Moving_Parts.

[73] Liwen Sang. “Diamond as the heat spreader for the thermal dissipation of GaN-based electronic devices”. In: *Functional Diamond* 1.1 (Jan. 2021), pp. 174–188. ISSN: 2694-1112. DOI: 10.1080/26941112.2021.1980356. URL: https://www.tandfonline.com/doi/full/10.1080/26941112.2021.1980356.

[74] Jürgen Schmidt et al. “Slow dust in Enceladus’ plume from condensation and wall collisions in tiger stripe fractures”. In: *Nature* 451.7179 (Feb. 2008), pp. 685–688. ISSN: 0028-0836. DOI: 10.1038/nature06491. URL: http://www.nature.com/articles/nature06491.

[75] Bruno Sena Maia. “Study on the Effect of Surface Energy of Polypropylene/Polyamide12 polymer Hybrid Matrix Reinforced with Virgin and Recycled Carbon Fiber”. PhD thesis. Mar. 2017.

[76] Kazimierz Skrobas et al. “Surface free energy of diamond nanocrystals - a molecular dynamics study of its size dependence”. In: *Physical chemistry chemical physics : PCCP* 23.18 (May 2021), pp. 11075–11081. ISSN: 1463-9084. DOI: 10.1039/D1CP00282A. URL: https://pubmed.ncbi.nlm.nih.gov/33942829/.

[77] Kai Sotthewes et al. “Pressure-Induced Melting of Confined Ice”. In: *ACS Nano* 11.12 (Dec. 2017), pp. 12723–12731. ISSN: 1936086X. DOI: 10.1021/ACSNANO.7B07472/SUPPL{_}FILE/NN7B07472{_}SI{_}002.AVI. URL: https://pubs-acs-org.tudelft.idm.oclc.org/doi/full/10.1021/acsnano.7b07472.

[78] J. R. Spencer et al. “Enceladus Heat Flow from High Spatial Resolution Thermal Emission Observations”. In: *European Planetary Science Congress* 8 (2013).

[79] John R. Spencer et al. “Enceladus: An Active Cryovolcanic Satellite”. In: *Saturn from Cassini-Huygens*. Dordrecht: Springer Netherlands, 2009, pp. 683–724. ISBN: 9781402092169. DOI: 10.1007/978-1-4020-9217-6{_}21. URL: http://link.springer.com/10.1007/978-1-4020-9217-6_21.

[80] Joseph N. Spitale et al. “Curtain eruptions from Enceladus’ south-polar terrain”. In: *Nature 2015 521:7550* 521.7550 (May 2015), pp. 57–60. ISSN: 1476-4687. DOI: 10.1038/nature14368. URL: https://www.nature.com/articles/nature14368.

[81] Jörg Stephan and Guenther Seliger. “Handling with ice – the cryo□gripper, a new approach”. In: *Assembly Automation* 19.4 (Dec. 1999), pp. 332–337. ISSN: 0144-5154. DOI: 10.1108/01445159910295249. URL: https://www.emerald.com/insight/content/doi/10.1108/01445159910295249/full/html.

[82] https://lairdthermal.com/products/thermoelectric-cooler-modules <OR> I. Surname, I. Surname, and I. Surname. *Title of the Website*. 2000. URL: https://example.com (visited on 12/24/2020).

[83] T.M. Tritt. “Thermoelectric Materials: Principles, Structure, Properties, and Applications”. In: *Encyclopedia of Materials: Science and Technology*. Elsevier, Jan. 2002, pp. 1–11. DOI: 10.1016/B0-08-043152-6/01822-2. URL: https://linkinghub.elsevier.com/retrieve/pii/B0080431526018222.

[84] Anne Verbiscer et al. “Enceladus: cosmic graffiti artist caught in the act”. In: *Science (New York, N.Y.)* 315.5813 (Feb. 2007), p. 815. ISSN: 1095-9203. DOI: 10.1126/SCIENCE.1134681. URL: https://pubmed-ncbi-nlm-nih-gov.tudelft.idm.oclc.org/17289992/.

[85] Jiangtao Wei et al. “Review of current high-ZT thermoelectric materials”. In: *Journal of Materials Science 2020 55:27* 55.27 (June 2020), pp. 12642–12704. ISSN: 1573-4803. DOI: 10.1007/S10853-020-04949-0. URL: https://link-springer-com.tudelft.idm.oclc.org/article/10.1007/s10853-020-04949-0.

[86] Brian H. Wilcox et al. “A deep subsurface ice probe for Europa”. In: *IEEE Aerospace Conference Proceedings* (June 2017). ISSN: 1095323X. DOI: 10.1109/AERO.2017.7943863.

[87] Andrew Work and Yongsheng Lian. “A critical review of the measurement of ice adhesion to solid substrates”. In: *Progress in Aerospace Sciences* 98 (Apr. 2018), pp. 1–26. ISSN: 03760421. DOI: 10.1016/j.paerosci.2018.03.001. URL: https://linkinghub.elsevier.com/retrieve/pii/S0376042118300058.

[88] Senbo Xiao, Jianying He, and Zhiliang Zhang. “Modeling nanoscale ice adhesion”. In: *Acta Mechanica Solida Sinica* 30.3 (June 2017), pp. 224–226. ISSN: 0894-9166. DOI: 10.1016/J.CAMSS.2017.05.001.

[89] Yang Yang and Jing Liu. “Thermal Radiative Cooling Enabled Freeze Tweezer for Manipulating Micro Scale Objects”. In: *ASME 2011 International Mechanical Engineering Congress and Exposition, IMECE 2011* 11 (Aug. 2012), pp. 539–543. DOI: 10.1115/IMECE2011-65755. URL: https://dx-doi-org.tudelft.idm.oclc.org/10.1115/IMECE2011-65755.

[90] Yang Yang, Jing Liu, and Yi-Xin Zhou. “A convective cooling enabled freeze tweezer for manipulating micro-scale objects”. In: *Journal of Micromechanics and Microengineering* 18.9 (Sept. 2008), p. 095008. ISSN: 0960-1317. DOI: 10.1088/0960-1317/18/9/095008. URL: https://iopscience.iop.org/article/10.1088/0960-1317/18/9/095008.

[91] Kris Zacny et al. “SLUSH: Europa hybrid deep drill”. In: *IEEE Aerospace Conference Proceedings* 2018-March (June 2018), pp. 1–14. ISSN: 1095323X. DOI: 10.1109/AERO.2018.8396596.

[92] Frank J. Zerilli and Hermenzo D. Jones. “Surface energy and the size of diamond crystals”. In: *AIP Conference Proceedings* 370.1 (May 2008), p. 163. ISSN: 0094-243X. DOI: 10.1063/1.50738. URL: https://aip-scitation-org.tudelft.idm.oclc.org/doi/abs/10.1063/1.50738.

[93] Dongliang Zhao and Gang Tan. “A review of thermoelectric cooling: Materials, modeling and applications”. In: *Applied Thermal Engineering* 66.1-2 (May 2014), pp. 15–24. ISSN: 13594311. DOI: 10.1016/j.applthermaleng.2014.01.074. URL: https://linkinghub.elsevier.com/retrieve/pii/S1359431114000854.

[94] Yizhi Zhuo et al. “Polysiloxane as icephobic materials – The past, present and the future”. In: *Chemical Engineering Journal* 405 (Feb. 2021), p. 127088. ISSN: 1385-8947. DOI: 10.1016/J.CEJ.2020.127088.

[95] M. Zou et al. “Effects of surface roughness and energy on ice adhesion strength”. In: *Applied Surface Science* 257.8 (Feb. 2011), pp. 3786–3792. ISSN: 01694332. DOI: 10.1016/j.apsusc.2010.11.149. URL: https://linkinghub.elsevier.com/retrieve/pii/S0169433210016727.

[96] Enci Zuo et al. “Electronic work function, surface energy and electronic properties of binary Mg-Y and Mg- Al alloys: A DFT study”. In: *Surface Science* 712 (Oct. 2021), p. 121880. ISSN: 0039-6028. DOI: 10.1016/J.SUSC.2021.121880.

A

Preparatory Ice Adhesion Tests

A series of preliminary tests are performed to identify flaws in the setup that potentially influence the repeatability of the results. All experiments are performed in the Material Science and Engineering lab, located in the faculty of Mechanical, Maritime and Materials Engineering of Delft Technical University.

A.1. Component Compatibility Test in Zwick Z010 Machine

A preliminary test is set up in a Zwick Roell Z010 material testing machine, as shown in figure A.1. This machine has a dual column load frame and can be used for tensile, compression and flexure tests up to 10 kN. The machine has a test speed range from 0.0005-2000 mm/min, travel resolution of 0.636 µm, repetitional position accuracy of $\pm$2 µm. Data is acquired with a rate of 400 kHz with 24 bit resolution and transferred to the connected computer at 500 Hz. The ice sample holder is secured to the bottom attachment point with a coupling, creating a rigid connection. The cross bar is fitted with a 10 kN load cell (Zwick Roell XForce K; 10 kN), this load cell type (XForce K) has a typical accuracy (maximum display deviation) <$\pm$0.25% of the measured value from 0.4% of load cell capacity; from 0.1% of load-cell capacity the accuracy is <1% of measured value. The calibration and accuracy of the load cell is in accordance with ISO 7500-1. A Zwick Roell Wedge Grip type 8302 10 kN is mounted on the load cell, the wedge grip has V shaped jaw inserts to accommodate the M10 bolt fastened on the adhesion effector. The mass of the wedge grip is approx. 8 kg. This wedge grip can be opened by moving the handle, when closed, the closing force is proportional to the tensile force applied during testing. These preliminary tests are performed in an open environment at room temperature, to see if any changes are required to the system. The ice samples are prepared beforehand and are stored in an insulated box.

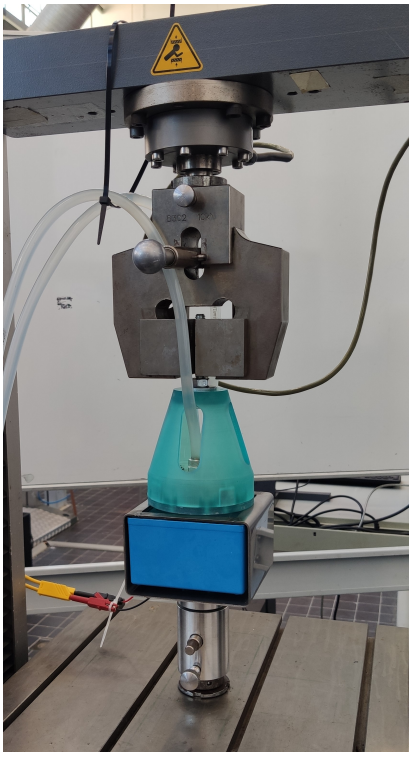

Figure A.1: Test setup for preliminary test.

During these tests, the ice sample is placed in the sample holder, see figure A.2a. Then the crossbar is lowered until the adhesion pad almost touched the ice sample top surface. After which the wedge grip lever is disengaged, releasing the adhesion effector onto the ice. If the cross bar were to be moved until the adhesion pad contacts the ice, there could be significant compressive forces acting on the adhesion effector assembly, since the crossbar is moved to an absolute position, rather than relative position to the ice. Essentially, the crossbar will move to the set position regardless of the ice surface height; deviation in ice surface height could cause the adhesion pad to 'crash' into the ice, with the possibility to damage components. Now, since there is no power supplied to the peltier module, the adhesion pad is at room temperature the moment it contacts

Table A.1: Preliminary test results - Copper Adhesion Pad - Polished (K4000)

Sample	F_{max} [N]	F_{break} [N]
Clear Ice 1	1089	1089
Clear Ice 1 - re-tested	392	392
Clear Ice 2	1181	1181
Regular Ice	738	738

the ice, thus the ice in contact with the adhesion pad starts to melt. After contact, power is supplied to the peltier module (I = 4 A), and the wedge grip lever is engaged 10 seconds after the peltier is powered on, securing the adhesion effector in the wedge grips. The peltier module is left to cool the adhesion pad and ice for a total of 60 seconds, before the pull-off test is initiated, figure A.2b. Once started, the cross bar will move vertically up with a constant test speed of 100 µm/s, this test speed is in accordance with tensile ice adhesion strength tests performed by Mirshahidi et al. [51] and Petrenko and Qi [57]. While the crossbar is moving, the standard force and strain are recorded until a break is detected. After the effector and ice are separated, the crossbar is raised manually to inspect the ice sample, depicted in figure A.2c. Additionally, the surface of the adhesion pad is examined for any residual ice, as seen in figure A.2d, residual ice on the ice suggests a (partial) cohesive break.

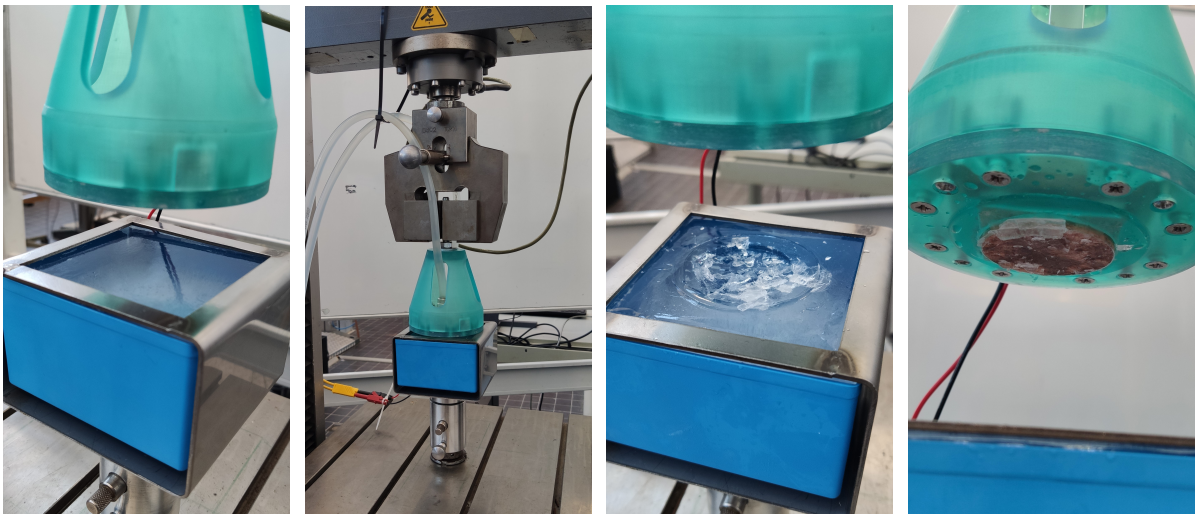

(a) Ice sample in ice sample holder.

(b) Adhesion effector lowered and attached to ice sample.

(c) Adhesion effector separated from ice sample; after test.

(d) Residual ice visible on adhesion pad, indicating adhesive/cohesive failure.

Figure A.2: Preliminary test procedure depicted.

Four samples were used during these preliminary tests, two samples are created with the directional freezing method, referred to as 'Clear Ice', one of which was tested twice (tested again after break; damaged ice surface), and one sample was created with the standard freeze method. The maximum recorded force and force at break during the tests are given in table A.1

These results show that the maximum force equals the force at break, indicating a brittle fracture as expected. The highest forces recorded are from the clear ice samples, a much lower adhesion strength is obtained when the ice sample is re-tested, confirming that a fresh sample should be used for every test. While the results can not be considered as significant, all the components function as expected and a more elaborate preliminary test can be set up that includes a temperature controlled chamber. There is no possibility to monitor the adhesion pad temperature with the current effector design, as there is no temperature sensor integrated in the effector housing. The ability to monitor the adhesion pad temperature is beneficial for the repeatability of the experiments. Additionally, the circular design of the adhesion effector housing prevents the effector to fit within the metallic frame of the sample holder. In order to ensure the adhesion pad is able to contact the ice sample surface and slightly penetrate the

surface to guarantee a proper connection, the design of the effector housing should be modified.

Changes

A new iteration of the effector housing design allows to address the two observations from the first preliminary test. While the working principle of the effector housing is the same as the previous design, the new iteration features a square footprint that allows the effector to fit inside the metallic sample holder and therefore the adhesion pad can rest on the ice sample without obstruction. A square shape is obligatory in this case, because simply reducing the diameter of the old, circular effector design until the effector fits within the sample holder would not provide the required space inside the housing to mount the water cooling block. Instead, a square shape is more compatible with the square mounting bracket of the water cooling block. The new effector housing, without internal components, is shown in figure A.3.

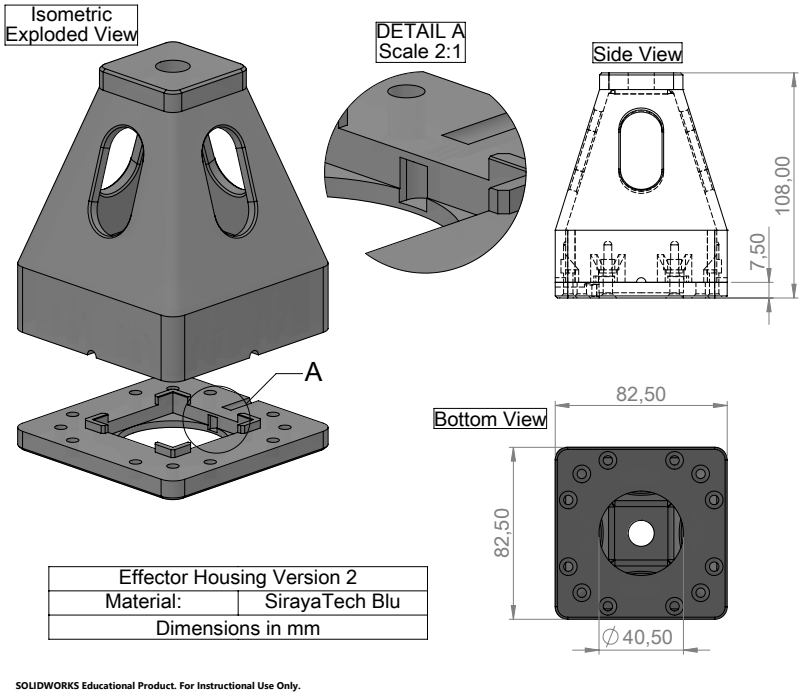

Figure A.3: CAD Model of the effector housing. Second iteration.

Detail **A** in figure A.3 reveals a recess in the effector housing bottom. This recess is dimensioned to accept a DS18B20 temperature sensor chip, and therefore enables the temperature sensor to be integrated in the effector housing. Once an adhesion pad is inserted in the effector bottom, the sensor will contact the side of the adhesion pad; a thermal interface material is applied to improve temperature measurement accuracy. The three pins for wiring the DS18B20 temperature sensor to the data logger are routed through small channels in the effector housing bottom, as shown in figure A.4, then an electrical wire is is soldered to the pins. Because the sensor is encapsulated in the plastic effector bottom, and therefore only has a single area contacting the adhesion pad, the temperature measurements of the adhesion pads are influenced by the temperature of the plastic housing. The difference in temperature readings, comparing the measurements from a sensor placed on the outer surface and the integrated sensor are shown in figure A.5.

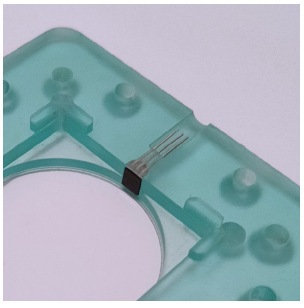

Figure A.4: DS18B20 Temperature sensor integrated in housing.

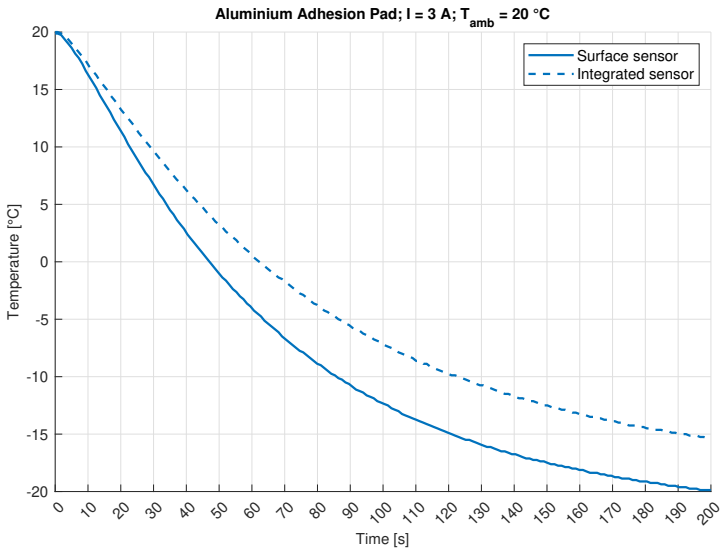

Figure A.5: Difference in temperature readings of the integrated sensor and surface mounted sensor.

A.2. Test: Component Compatibility in Cooling Chamber

The second preliminary test involves testing the components in a temperature controlled environment. Using a temperature chamber improves ice temperature consistency during the tests, this an important parameter to control since the ice cohesive and adhesive strength are influenced by the temperature of the ice. Fortunately, a tensile testing machine with temperature chamber is available at the Material Science and Engineering department of Delft University of Technology. This temperature chamber has a temperature range of -80°C to 250°C and can be fitted to various testing machines. In this case, it is fitted to a Zwick Roell Z100 AllroundLine Universal testing machine. The temperature chamber is electrically heated and requires supplied liquid nitrogen for cooling, therefore an insulated vat with a capacity of 20 liters is filled with liquid nitrogen before each set of experiments. The machine has a test speed range from 0.00005-100 mm/min, travel resolution of 0.484 µm, repetitional position accuracy of $\pm$2 µm. Data is acquired with a rate of 400 kHz with 24 bit resolution and transferred to the connected computer at 500 Hz. The cross bar is fitted with a 100 kN load cell (Zwick Roell XForce K; 100 kN), this load cell type (XForce K) has a typical accuracy (maximum display deviation) <$\pm$0.25% of the measured value from 0.4% of load cell capacity; from 0.1% of load-cell capacity the accuracy is <1% of measured value. The calibration and accuracy of the load cell is in accordance with ISO 7500-1. This machine has a larger volume and load capacity compared to the Z010 testing machine, but the fitted temperature chamber reduces the available space significantly. As a result, mounting the adhesion effector using the appropriate wedge grips and sample holder adapter in a conflicting height between the adhesion effector and sample holder, as shown in figure A.6a. Fortunately, there are different adapters already available for this machine, a combination of which resulted in the setup shown in figure A.6b. Now the adhesion effector is attached to a solid aluminium testing adapter with an M12 bolt screwed in the threads of the adapter. This adapter is fitted to a reducing adaptor with a pin.

The testing procedure for the setup shown in figure A.6b slightly differs from the procedure in the Z010 testing machine. Firstly, the temperature chamber is set to -15°C and all the ice samples are placed in the chamber. Once the internal ice and chamber temperature reach -15°C, the experiment can begin. The ice sample is placed in the holder, followed by lowering the crossbar until the adhesion pad is almost touching the surface of the sample, then a pin is released to manually lower the adhesion effector onto the sample. Then power is supplied to the adhesion effector (I = 4 A), and left to cool for 20 seconds. After 20 seconds, the crossbar is lowered until the pin can be reinserted to connect the adhesion effector to the top assembly. After an additional 40 seconds has passed, the test is initiated. This procedure is repeated for all 10 samples. The mean F_{max} for a copper adhesion pad with polished surface (K4000) is 514 $\pm$216 N (%42 of the mean), with a highest recorded force F_{max} of 972 N and lowest F_{max} of 225 N. While these results can not directly be compared to the first preliminary

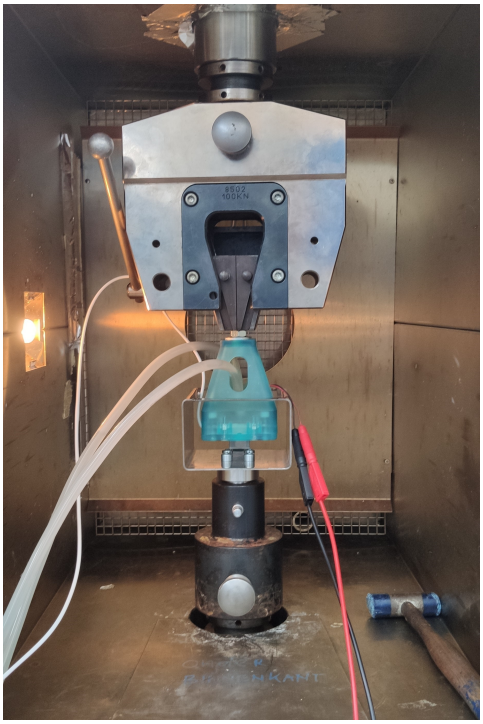

(a) Failed setup: combined height of components are conflicting.

(b) Resulting setup for preliminary test in temperature chamber.

Figure A.6: Different test setups in the temperature chamber.

tests, since the first preliminary test was performed with only two clear ice samples in an uncontrolled temperature environment, the difference in results do suggest there are environmental and or procedural factors influencing the tests, this is confirmed by the high standard deviation of the mean. The issues encountered during this second preliminary experiment are elaborated in the following paragraphs.

Issues: Adapters

An ample amount of adapters is required to mount the adhesion effector and ice samples in the Zwick Roell Z100 testing machine; each adaptor introduces some degree of play in the assembly (highlighted in figure A.7. As a result, the adhesion effector can move a total of 11 mm in lateral direction. Therefore it is difficult, if not impossible to attach the adhesion pad to the ice sample perfectly aligned to the central axis of the tensile pulling force. This introduces a peeling force, or bending moment at the connection between the adhesion pad and ice sample, resulting in areas of high stress concentrations at which the adhesion or ice possibly fails, influencing the test results. Although the ice sample holder is held more securely, there is still some lateral play leading to the same issues. Additionally, the geometry of the ice samples is not perfectly consistent throughout all samples, causing some samples to have a closer fit in the sample holder than others. If the top surface of the ice sample is not flush against the metal structure of the sample holder, it will move up with the adhesion effector during the experiment until it makes contact with the sample holder. This can also lead to an uneven loading on the adhesive connection between adhesion pad and ice sample.

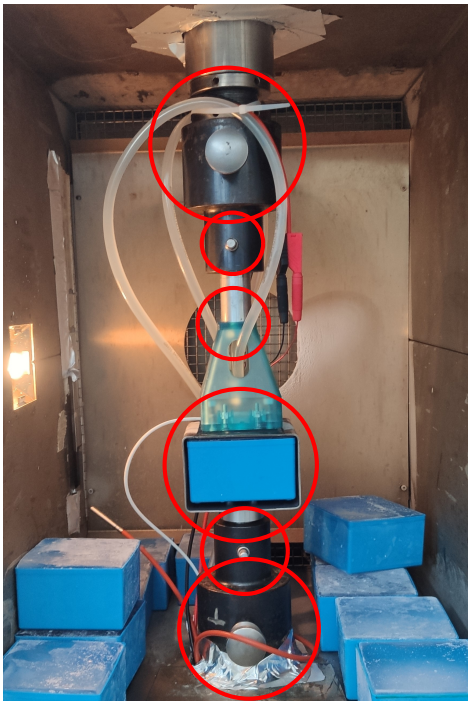

Figure A.7: Adaptors in test setup highlighted.

Issues: Manual Interactions
The current setup requires a lot of manual steps before the test can be started, each of these interactions introduce uncontrolled parameters during the test. First of all, attaching the adhesion effector to the ice sample requires a lot of manual steps. A pin has to be released to allow the adhesion pad to contact the ice, then while holding the effector with one hand, the power supply to the peltier module is switched on with the other hand. Not only does this greatly reduce the chance of attaching the adhesion effector to the sample straight, the pressure applied on the ice during this process will differ between tests as well. Additionally, the 'melt time', the time between the adhesion pad contacting the ice and switching on the cooling of the adhesion pad, is uncontrolled and thus different in each test. Longer melt times lead to deeper penetration of the adhesion pad, while melt times that are too short can lead to incomplete melting of the adhesion pad - ice interface, and thus incomplete attachment of the adhesion pad area. Then, after establishing an adhesive connection between the adhesion pad and ice sample, the crossbar is lowered to be able to re-insert the pin, connecting the adhesion effector to the crossbar assembly. Aligning the holes in the adaptors was found difficult due to the play in the adaptors. And finally, while all these steps are executed, the door of the temperature chamber is opened, which causes a change in temperature inside the temperature chamber, often close to 0°C. Cooling the temperature chamber back to the desired temperature takes a significant amount of time (> 60 s) and liquid nitrogen.

Setup Changes
This section elaborates on a set of improvements to the experimental setup, to reduce the variance in experimental conditions.

Adhesion Effector Mounting
A new adhesion effector mounting adaptor is designed and machined to accomplish multiple goals. First of all, it should drastically reduce lateral movement of the adhesion effector once mounted to the crossbar assembly, to avoid uneven loading conditions. Additionally, it should eliminate the need to manually attach the adhesion effector to the ice sample, which implies that the adhesion effector mounting should be unconstrained in the positive vertical direction to avoid damage when the crossbar is lowered to a pre-defined height. This requirement attains another positive effect, namely the possibility to apply constant pressure during the attachment of the adhesion effector to the ice sample. The CAD

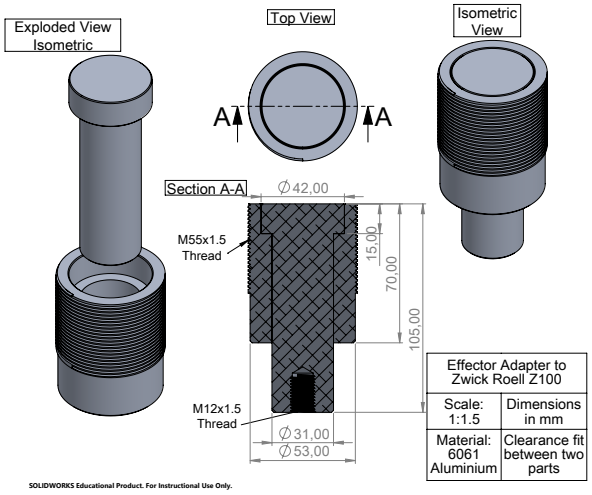

Figure A.8: Sliding adapter to connect the adhesion effector to the Zwick Roell Z100 testing machine.

design of the new adapter is shown in figure A.8. This adapter consist of two parts, the main body features M55x1.5 external threads that allow the adapter to be attached directly to the existing threads of the machine, a retaining nut will eliminate any backlash. And the inner part is able to slide and rotate within the main body, and features a shoulder that rests on the outer body, this will transfer the load during the pull-off tests. Additionally, M12 threads are tapped in the bottom of the inner part, used to securely mount the adhesion effector. The parts are machined to achieve a clearance fit that allows material contraction due to temperature fluctuations.

Ice sample container and holder

While the existing ice sample containers provide a cost effective method to produce ice samples, the low stiffness of the containers leads to irregular ice sample geometries. This is caused by the expansion of water transforming from a liquid to solid state, causing the sample to deform and/or break the plastic container. Although it is possible to obtain a relatively flat ice surface by melting the surface on a highly conductive surface (e.g. aluminium), overall dimensions of the samples are inconsistent. These irregularities translate to very loose or tight fit of the sample in the sample holder. Therefore a more rigid container is preferred, to reduce the ice sample irregularities. Albeit of low priority, the time required to produce ice samples with the containers is relatively high, as every sample takes 24 hours to freeze. And with the available freezer, the maximum number of insulated sample container is limited to three. And lastly, considering that the sample holder has a much looser fit in the Z100 machine compared to the Z010 machine, allowing more lateral play, a new iteration of both the sample container and holder is favored. The new sample containers are constructed from 80 mm stainless steel tubing with a wall thickness of 2 mm, this tube is cut to 60 mm lengths and the ends are squared on a manual lathe. A circular, stainless steel disk is welded concentric to the bottom of this tube to create a watertight container. The disk fitted to the bottom has a thickness of 3 mm and diameter of 90 mm. The larger disk diameter creates a lip at the bottom of the container, which acts as the feature to secure the container. A total of 12 containers are fabricated for the experiments, three of which are displayed in figure A.9. These containers are placed in an styrofoam tray to insulate the sides and bottom, to effectuate the directional freeze method. Now, due to the smaller footprint of the containers, a total of 12 ice samples can be prepared in 24 hours. A complete re-design of the ice sample holder is also required for the new sample container, the new holder is machined from solid 6061 aluminium round stock. The CAD design of the sample holder is shown in figure A.10. This sample holder can be attached to the bottom mounting shaft of the Zwick Roell Z100 testing machine with a 30 mm pin and a retaining nut removes any clearance between the parts. The ice sample containers are easily slotted in the holder, while vertical movement is constrained. The vertical clearance between the sample container and holder is removed by inserting a wedge between the two parts, illustrated in the bottom left of figure A.10.

Figure A.9: New ice sample container

Controlling Melt and Freeze Time

During the first and second preliminary tests, it proved to be difficult to create similar melt and freeze times throughout the tests. Additionally, the temperature of the adhesion pad at the start of the experiment should be consistent throughout the tests. Different melt times lead to dissimilar adhesion pad penetration and therefore a variance in volume of water undergoing a phase transformation (solid-liquid and vice versa). Since the cooling/heating surface of peltier modules are easily reversed by switching the polarity of the power supply, a basic control system can be designed to enforce the desired melt and freeze time. This control system is made up from electro-mechanical relays that are wired in an H-bridge configuration. An H-bridge is an electrical circuit that can change the direction of current passing through a load by switching its polarity, as illustrated in figure A.11, commonly used to control the direction of rotation of electric motors. While there is a wide variety of H-bridge circuits, from dedicated integrated circuits (IC), to mechanical switches; electro-mechanical relays are selected to build the H-bridge circuit. These relays are cost effective, easily controlled and capable of handling the loads applied to the peltier (max 15V, 5A), but do not provide the most compact solution, however.

An Arduino Nano microntrollerboard is programmed to switch the H-Bridge circuit according to a pre-defined timer sequence. Before activating the sequence, the 'normal' state of the controller is the cooling configuration. This is to ensure the same adhesion pad starting temperature before the sequence is initiated, and allows the adhesion pad to contact the ice before the experiment is started, since both the substrate and adhesive are at sub-zero temperatures; no melting will occur. Once activated, the sequence is as follows:

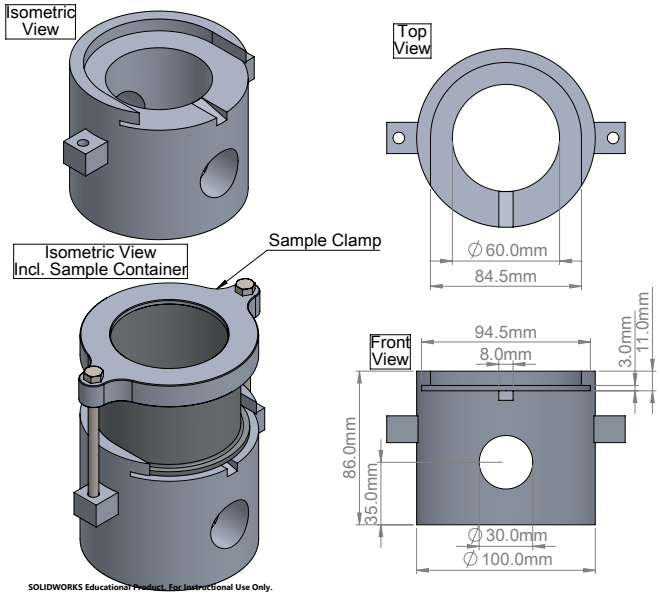

Figure A.10: CAD design of second version of the sample holder.

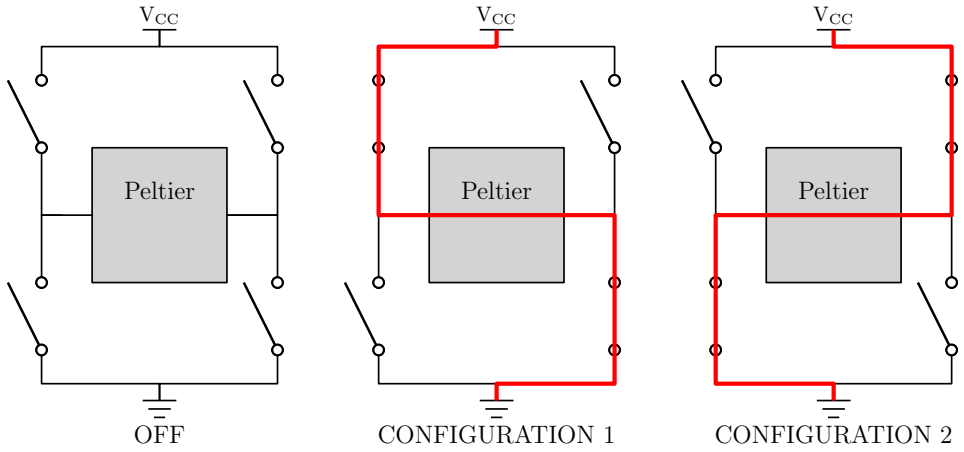

Figure A.11: Schematic overview of H-Bridge circuits.

1. Rest for 10 s, no power to peltier
2. Heat for 25 s
3. Rest for 10 s, no power to peltier
4. Cool indefinitely; buzzer sounds after 80 s to initiate test

Rest periods are added in the sequence to avoid rapid switching of the peltier module, which can cause damage. The components are fitted in a small enclosure manufactured using the Elegoo Saturn mSLA printer, see figure A.12. The toggle switch on the enclosure sets the actions performed by the controller; 'cooling', 'off', and 'test sequence'. The momentary switch can manually activate the heating configuration when depressed, given that the toggle switch is in the 'off' position. When the 'test sequence' is selected, the peltier will be switched to the cooling configuration, until the sequence is initiated. In fact, the controller is signalled by the temperature logger; initiating the data logging to SD card will signal the peltier controller to start the sequence.

Figure A.12: H-bridge peltier controller box.

A.3. Test: Second Iteration Adhesion Effector and Ice Samples

All the modifications combined result in the setup shown in figures A.13, this figure shows the parts inside the temperature chamber. Now the test procedure is as follows: the temperature chamber is cooled to -15°C and the samples are placed inside. Once the internal ice sample temperature equals the temperature inside the chamber, the first sample is placed in the bottom sample holder and secured using the 15°wedge. Meanwhile the H-Bridge controller is initialized and set to 'sequence mode'; this sets the peltier to cooling. Then the crossbar is lowered to the start position, this lowers the adhesion effector on the ice. In fact, the crossbar start height is set to 5 mm below the ice sample surface, this ensures the adhesion effector is able to descend during the melting phase and apply constant pressure. Once the start position is reached, data logging is enabled on the temperature logger; initiating the melt-freeze sequence on the H-Bridge controller. After 150 seconds, the sequence is complete and the buzzer indicates the test should commence. After a break is detected, the ice sample and adhesion surface are inspected, any ice remaining on the adhesion pad is removed. For this preliminary test, 12 samples are prepared and the polished (K4000) copper adhesion pad is used, however the experiment is canceled after only four samples; in two of the samples the ice separated from the sample container as a whole, as shown in figure A.14. This indicates that the adhesive strength between the ice sample and container does not prove to be a reliable method for constraining the ice in vertical direction.

Figure A.13: Preliminary test 3: Setup

Changes

To prevent the ice sample from slipping, adding a retaining ring near the top of the ice sample containers would seem to be the most obvious and effective solution. However, such a ring would also restrain the movement of ice during the freezing process, likely causing deformation or damage to the ice, restraining ring or sample container. Instead, anchoring the ice near the bottom of the container would circumvent such issues, and is compatible with the directional freeze method since the anchor would be the last part to freeze solid. Figure A.15a shows a section view of the sample container with the proposed anchor. Stainless steel carriage bolts, commonly used in woodworking applications, have similar shape and can therefore be used as such anchors with limited modifications. Threads are tapped in the bottom of each container, these threads ensure the carriage bolt is fitted perpendicular and concentric to the container. To create a secure and watertight joint, the carriage bolt is welded to the container using a gas tungsten arc welding (GTAW) process. The modified containers are shown in figure A.15b.

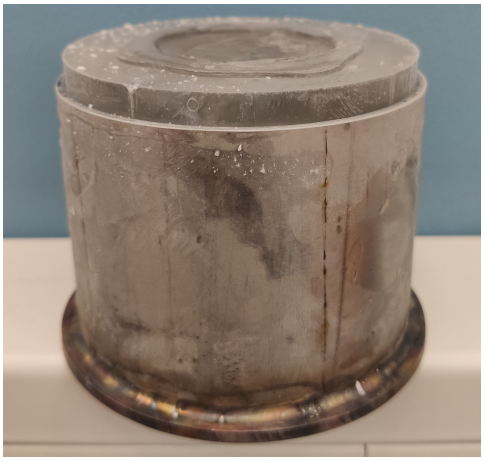

Figure A.14: Ice separated from sample container.

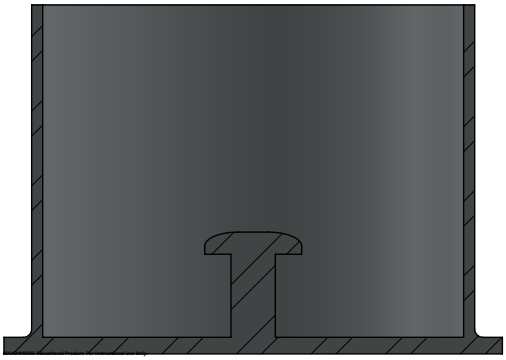

(a) CAD model section view of the ice sample container with anchor.

(b) All sample containers with the anchor modification.

Figure A.15: Modifications to the ice sample containers.

A.4. Test: Ice Sample Anchors

This set of experiments is similar to preliminary test 3; 12 samples are prepared and tested in the Zwick Z100 tensile testing machine. The adhesion effector is fitter with a polished (grit: K4000) copper adhesion pad. This time, all 12 samples are tested until failure, resulting in a mean F_{max} = 660 $\pm$350 N (53% of the mean), with highest recorded force F_{max} of 1280N and lowest recorded force F_{max} of 160 N. Revealing an increase in variance over preliminary test 2 (mean F_{max} = 514 $\pm$216 N (%42 of the mean)). In addition to the high variance, two ice samples failed at the added anchors as shown in figure A.16a and A.16b, implying that the anchor does not not provide a reliable way to secure the sample to the container.

In addition to the two samples that separated from the container, the inspection of the remaining sample revealed another irregularity. The ice transformed to liquid during the melt phase seems to contact the effector housing and freeze, since this housing is also at a temperature of -15°C. This creates an adhesive connection between the ice sample and plastic effector housing. Inspecting the ice sample surface after testing reveals an apparent failure at this additional connection, while the ice surface of the adhesive connection between the adhesion pad surface and ice remains relatively undamaged. Two examples illustrate this observation in figure A.17a and A.17b, where the areas of additional adhesion are highlighted in red, and the area contacted by the adhesion pad is highlighted in green.

This additional connection is undoubtedly undesirable since the measured adhesive strength is now measured of compound materials; adhesion between water ice - copper and water ice - plastic. While the tests should be limited to a single material with known surface area, in order to obtain results that can be compared between materials. While comparability of results is the primary argument to resolve this issue, another telling observation is found when examining the ice samples of the maximum forces recorded in this experiment set. The ice samples of the two highest recorded tests (F_{max} = 1280 and

(a) Ice sample attached to the adhesion effector; separated from the container with F_{max} = 1250 N.

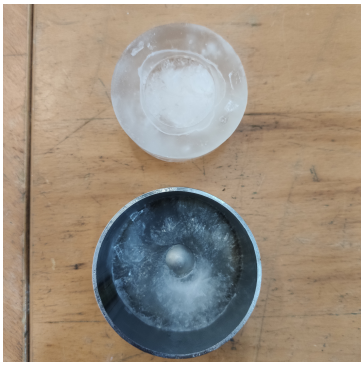

(b) Ice sample failed at the ice anchor.

Figure A.16: Ice sample separating from container during preliminary test 4.

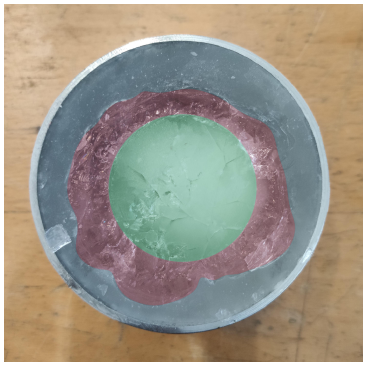

(a) Ice sample 4 after test, failed at F_{max} = 450 N.

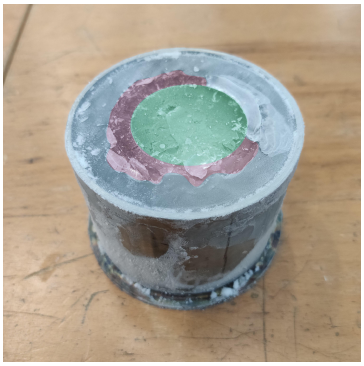

(b) Ice sample 9 after test, failed at F_{max} = 301 N.

Figure A.17: Inspecting ice samples after test. Green areas indicate adhesion pad contact, red areas indicate the (failed) adhesive connection between ice sample and effector housing.

1250 N) show no signs of this additional connection when inspecting the samples after testing. This is in contrary to first intuition; a larger adhesive area should increase maximum recorded force. Further inspection of the ice samples with the signs of additional adhesion, in combination with the properties of liquid and solid water help form a theory. Liquid water formed during the melt phase is rejected from underneath the adhesion pad and spills sideways. Since the adhesion pad only protrudes 2.5 mm below the effector housing bottom plate, and the adhesion pad will slightly penetrate the ice sample, capillary action of water allows the water to contact both the surface of the ice sample and effector housing bottom. The effector housing is also at sub-zero temperatures, this causes the liquid water between the effector housing bottom and ice sample to transform back to solid (ice). Now, liquid water at 0°C has a density of 999.9 kg/m^3, while the density of solid water at 0°C is 916.8 kg/m^3; an expansion of roughly 9%. Since the liquid water formed underneath the adhesion pad is mostly rejected to the sides, the layer of liquid water underneath the adhesion pad is expected to be thin. Meanwhile the distance between the effector bottom and ice sample surface is between 1.5 and 2.0 mm thick, depending on the penetration depth of the adhesion pad. Resulting in an expansion mismatch of the two volumes of liquid water transforming to solid; water expanding between the effector housing bottom and ice sample forces the effector to move up. This then either causes a preload on the adhesion between adhesion pad and ice sample, or the two surfaces to separate. Both resulting in a lower measured force during the test. This theory is illustrated in figure A.18. Note that this theory is inconclusive and lacking evidence; dedicated tests are required to either validate or reject this theory.

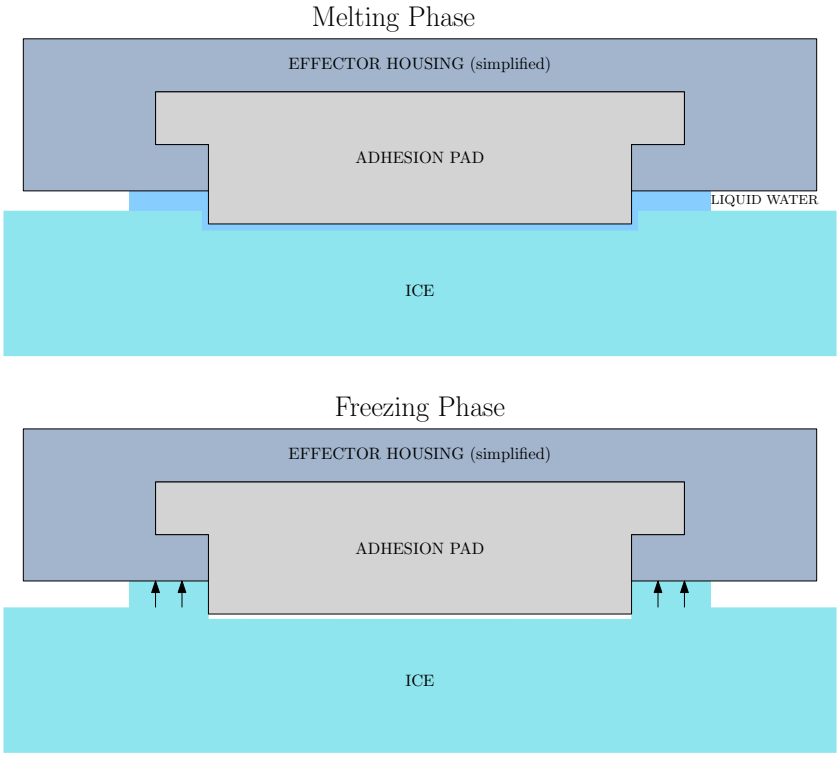

Figure A.18: Liquid water formed during the melting phase (top), potentially causing the adhesion pad and ice sample to separate (bottom). Deformations are scaled up (3X) to visualize the effect.

Changes

Eliminating the additional adhesive connection is easily resolved by increasing the distance the adhesion pad protrudes from the effector housing. This ensures that the liquid water formed during the melt phase and rejected to the side of the adhesion pad, is unable to contact and adhere to the effector housing bottom. To accomplish this effect, the total adhesion pad height is increased to 14 mm, so that the adhesion pad protrudes 6.5 mm below the effector housing bottom.

A.5. Test: Increased Adhesion Pad Height

This tests will determine the new melt and freeze times appropriate for the increased adhesion pad height, since the new adhesion pad has a larger volume, more time is required to reach the desired temperatures. Additionally this test will examine if the increased adhesion pad height eliminates the additional adhesive connection between effector housing and ice sample, and how that effects the variance in test results. First of all, 12 samples are prepared in order to determine the melt and freeze times for both the copper and aluminium adhesion pads, resulting in six samples for each material. For aluminium, melt time is increased from 20 s with steps of 2.5 s until the adhesion pad penetration is measured at 1 mm. In the case of the copper adhesion pad, melt time is increased from 25 s with 2.5 s steps to achieve the same adhesion pad penetration. This test resulted in melt times of 30 and 35 s for aluminium and copper, respectively. Freeze times are set to the time required until the effector temperature sensor indicates a temperature of -15°C, resulting in 90 s and 100 s for aluminium and copper, respectively.

With these new parameters, six samples are prepared and tested in combination with the polished (K4000) copper adhesion pad, resulting in a mean F_{max} of 1075 $\pm$119 N (11% of the mean). While the standard deviation of the mean shows a substantial improvement over the previous preliminary tests, the failure mode of the samples indicate more modifications to the setup are required. Five out of the six samples failed cohesively halfway along the sample, as shown in figures A.19. All those five samples failed at the interface where bubbles start to form during the directional freeze process, indicating that the yield strength of this bulk material (ice and bubbles) is lower than pure water ice and the limiting factor for these tests. Although some additional modifications are desirable, the recorded force at break

shows a significant increase over previous preliminary tests. This is in favor of the proposed theory behind the premature adhesive failures that is illustrated in A.18, since no additional adhesive contact areas is observed. In fact, these results are more similar to the very first preliminary tests performed without the temperature chamber, even though there is limited data available. Nonetheless, the first preliminary test was performed in an open environment at room temperature, which implies that the plastic effector housing was also at room temperature. It then follows that any liquid water contacting the plastic effector bottom that has been rejected from underneath the adhesion pad will not transform to ice, causing the expansion.

Figure A.19: Cohesive failure of ice sample at bubble interface.

Changes

Since the ice is not properly constrained in the sample holder and the defects in the ice cause the sample to fail before the adhesion fails, a direct comparison of ice adhesion strength of different materials is impossible. Therefore additional measures are required to secure the ice sample. The addition of a top 'lid' with a circular cutout in the center, secures the ice sample and container to the sample holder using two M10 bolts. These parts are produced with basic lathe and mill operations and welded using a GTAW process. The modifications are shown in figure A.20. To ensure this clamp contacts the ice rather than the sample container, thus preventing any movement of the sample, the contact surface is angled 5 degrees.

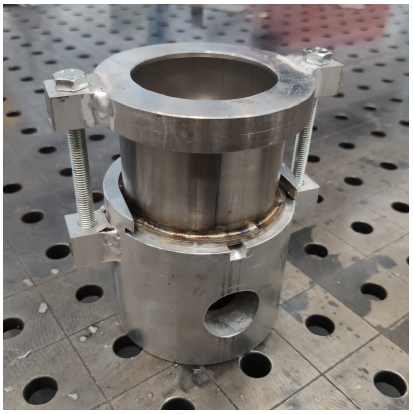

Figure A.20: Additional features to prevent ice slipping from the sample container.

A.6. Test: Ice Sample Clamp

Testing the effectiveness of the modifications introduces after preliminary test 5 is done by testing 12 prepared ice samples with a polished (K4000) copper and aluminium adhesion pad; six samples for each material type. The results are given in table A.2. A visual inspection of the samples after testing indicate that tests with the polished copper adhesion pad result in a adhesive fracture of the adhesive interface for four out of six samples, although some residual ice is found on the adhesion pad after testing. Meanwhile the polished aluminium adhesion pad exclusively resulted in cohesive fracturing of the ice. No obvious flaws are observed during the experiments, so the preliminary testing phase is concluded with this set of experiments.

Table A.2: Preliminary test 6: Tensile pull off test results for polished copper and aluminium.

	Copper F_{max} [N]	6061 Aluminium F_{max} [N]
Sample 1	1220	1190
Sample 2	2220	1410
Sample 3	1713	2130
Sample 4	1270	1320
Sample 5	1130	1650
Sample 6	1650	1810
Mean	**1533** $\pm$376 (%24.5)	**1585** $\pm$319 (%20.1)

B

Tensile Pull-off Tests: Comparative Study

B.1. In Depth Analysis of Ice Adhesion Tests

Including all the preparatory tests (described in appendix A) and final set of experiments, more than 100 ice adhesion tests have been performed. Here these results are discussed in detail.

Table B.1: Mean ice adhesion strength for the six adhesion pads, including standard deviation.

Surface Type	Material	Mean adhesion strength [MPa]	Standard deviation [MPa (%)]
Polished K4000	Copper	1.220	±0.299 (24.5%)
	Aluminium	1.261	±0.253 (20.1%)
Sandblasted	Copper	1.348	±0.589 (43.7%)
	Aluminium	1.515	±0.239 (15.8%)
Grid Pattern	Copper	1.026	±0.158 (15.4%)
	Aluminium	1.043	±0.218 (20.1%)

Adhesion Strength Compared

The results from the final set of experiments indicate that the grit-blasted aluminium adhesion pad results in the highest average grip strength (1.515 MPa), followed by the grit-blasted copper adhesion pad (1.348 MPa). Coincidentally, both the highest (2910 N) *and* lowest (861 N) recorded force at break of this set of experiments was also measured with the grit-blasted copper adhesion pad, in fact, these measurements are from consecutive tests. The lowest average grip strength is found using the copper adhesion pad (1.026 MPa) with the grid pattern milled in the surface, although the difference with the grid patterned aluminium adhesion pad (1.043 MPa) is marginal. Conversely, these adhesion pads have the highest contact area. Both of the polished adhesion pads performed similar to one another, with the aluminium pad (1.261 MPa) marginally outperforming the copper adhesion pad (1.220 MPa). At first sight, the results suggest that the surface treatment is the governing factor in grip strength, since the differences between materials in the same surface type are smaller than the differences between surface types. However, additional factors need to be considered. First of all, the results of the final set of experiments indicate that failure mode of the majority of tests is a cohesive break (31 out of 36 tests), and the tests that did fail with an adhesive break are mostly the tests using the polished copper adhesion pad (four out of six samples). Meanwhile the measured grip strength of the copper adhesion pad (1.220 MPa) is similar to the polished aluminium adhesion pad (1.261 MPa), which in turn displayed solely cohesive breaks. Cohesive breaks indicate that the ice strength or quality is the limiting factor in the connection between substrate and adhesive. Then, the working principle(s) responsible for the differences in measurements are not so conspicuous, however, multiple factors are discussed.

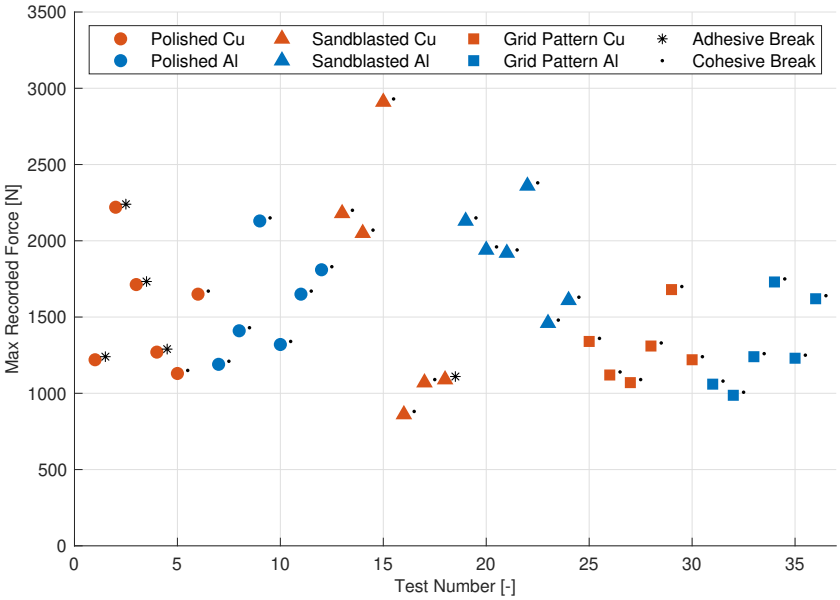

Figure B.1: Test results of the tensile pull-off tests for the six adhesion pads.

Influence Properties of Ice

The brittle nature of ice makes the material sensitive to stress concentrations; the combination of brittle materials and stress concentrations may lead to (premature) fractures. Stress concentrations in a material or adhesive joint arise from sharp corners, defects (such as air bubbles) of uneven loading. Although the grid pattern adhesion pads have the highest contact area, the protruding features on the surface also introduce a high number of sharp corners. Each of the sharp corners are potential locations for cracks in the ice to initiate, leading to a cohesive break. Contrarily the polished adhesion pads are free of any deformations, so it is unlikely for stress risers to occur on the pad contact surface. However, the polishing process is only applied to the contacting surface of the adhesion pads, resulting in relatively sharp edges of the pad. Then, the grit-blasting surface treatment also introduces surface deformations, but on a much smaller and moderate scale. In fact, the grit-blasting process removes the sharp corners of the pad edges, while increasing the wettability of the surface; decreasing the likeliness of in-ice cracks initiating at the substrate-adhesive interface. The effect of stress risers in ice is in fact observed when inspecting the ice samples after testing. Figures B.2a and B.2a of figure B.2 show ice sample 24 after testing with the grit-blasted aluminium adhesion pad. The arrows point out a circular fracture line, this line coincides with the location and circular shape of the clamp used to secure the sample to the bottom assembly of the test setup. Moreover, the angled inner surface of the clamp contacting the ice, establishes a line contact rather than contact surface on which the force during testing is transmitted. This line contact therefore introduces localized stress concentrations in the ice sample. In fact, an audible crack could be observed when securing the M10 bolts on the clamp for some of the ice samples (samples four and five of the grit-blasted copper adhesion pad; test numbers 16 and 17 of figure B.1. This suggests that defects could have be introduced in the sample prior to testing, these defects can lead to premature failure of the ice; a possible explanation for the relatively large deviation recorded with the grit-blasted copper adhesion pad.

Temperature During the Tests

All of the experiments are performed in the temperature chamber to create a controlled environment, the target temperature was -15°C for all the tests. However, since the door of the temperature chamber is frequently opened to replace the ice sample in the sample holder, as well as the removal of any residual ice from the adhesion pad surface, the temperature in the chamber would drop dramatically after each test, causing large temperature fluctuations. The cooling of the chamber is regulated using a basic temperature controller, and the cooling rate is highly dependent on the pressure of the supplied liquid nitrogen. If the supply pressure is low, the temperature chamber undershoots the target temperature (higher temperature) or takes a long time to reach the target temperature, while high pressures resulted

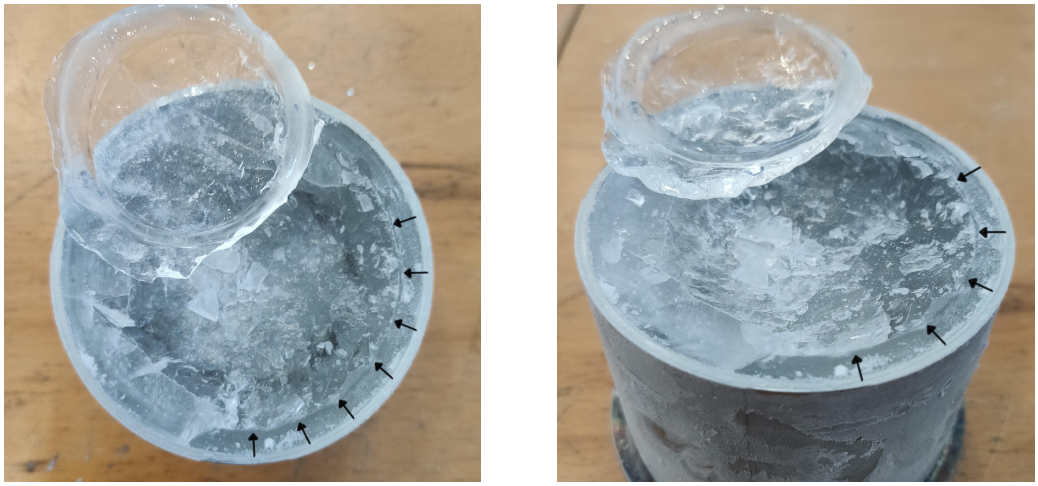

(a) Top view of ice sample. **(b)** Isometric view of ice sample.

Figure B.2: Ice sample 24, tested with a grit-blasted aluminium adhesion pad. Arrows indicate signs of stress concentrations leading to a cohesive fracture.

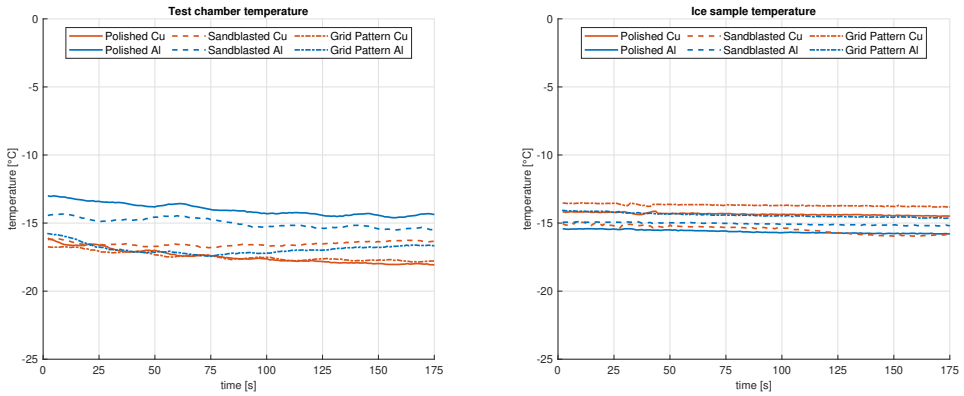

Figure B.3: Average ice sample temperature (right) and test chamber temperature (left) during the experiments.

in chamber temperatures overshooting the target temperature (lower temperature). Now, to supply a flow of liquid nitrogen to the temperature chamber, the isolated vat of liquid nitrogen is initially pressurized using high pressure nitrogen from a separate cylinder. After the tank of liquid nitrogen is pressurized and a good flow of liquid nitrogen to the temperature chamber is established, the supply pressure to the tank had to be shut of in order to limit waste of nitrogen gas. Therefore the pressure inside the tank of liquid nitrogen relies on the vapor pressure inside the tank, the back pressure of the tank was regulated by an over pressure relief valve. Due to the cold temperature of the liquid nitrogen, ice would form inside the relief valve; leaving it in the open position. This then prevented the vapor pressure to reach an equilibrium (between condensation and evaporation) in the tank, but caused positive feedback effect instead; more nitrogen released from the valve caused more ice to form in the valve from the humidity in the air, releasing more pressure from inside the tank. All in all this resulted in an unsteady supply of liquid nitrogen to the temperature chamber, inevitably leading to fluctuations in cooling performance and thus in temperature throughout the tests. In some severe cases, the tank of liquid nitrogen would be empty before a set of six samples are tested. This would be the case when the tank of liquid nitrogen was not filled sufficiently and heavy icing in the relief valve. While testing the ice samples with the grit-blasted copper adhesion pad, the tank of liquid nitrogen was empty after the second sample (test number 14 in figure B.1), unavailability of lab technicians meant the tank could not be refilled immediately. This caused the internal ice sample temperature of the remaining samples (test numbers 15-18) to reach nearly 0°C, before testing could continue, the samples were cooled in the temperature chamber until the internal temperature was equal to the target temperature, however. These complications lead to the differences in average chamber temperatures during the

tests, visible in the left graph of figure B.3. While the temperature fluctuations do effect the internal ice sample temperature, the variation in average sample temperature of the tests is less pronounced because of the thermal mass, and medium of the samples. While there is some variation in chamber and sample temperature, the tensile ice adhesion tests performed by Mirshahidi et al. [51] report that the ice adhesion strength performed at different temperatures (-5°C to -20°C in 5°C increments) are statistically equivalent, however these tests were performed with polypropylene and polyethylene materials, resulting in exclusively adhesive fractures. According to the critical review by RØnneberg et al. [67] on ice adhesion test methods, the ice temperature can dictate the failure mode of the adhesion; ice temperatures close to the melting point result in adhesive fractures, while ice temperatures lower than the transition temperature result in cohesive fractures, but is highly dependent on ice and material type, however. This transition temperature is found to be between -10°C and -20°C for precipitation ice adhered to aluminium surfaces with a centrifuge ice adhesion test, this was not observed for other materials [21].

Although the temperature at test is similar across all tested samples, the samples that have been close to 0°C (test numbers: 15-18 and 19-24) could have experienced an 'annealing' cycle. Ice forms at 0°C (in normal air pressures) as a result from the release from latent heat while freezing, the liquid-solid interface is therefore at 0°C, but the ice directly after the interface is at lower temperatures. The temperature difference of the interface might induce strain and fracturing in the ice [45]. Ice samples that have been close to the melting point might have reduced internal stresses, since ice becomes more ductile at temperatures close to the melting point. Experiments performed by Petrenko and Qi allowed the generated ice samples to anneal for 48 hours at -10°C [57]; the critical review by Work and Lian suggests that this likely aided in reducing internal stresses in the samples. A reduction in internal ice stresses translate to a reduced probability of premature ice failure from internal fractures during testing.

Results Compared to Literature

Although more than 100 ice adhesion tests are performed including the preliminary tests, the final set of experiments only consist of six samples per adhesion pad type. Despite the limited number of tests, the adhesion strength and standard deviation of the measurements obtained here are in accordance with results found in existing literature. Mirshahidi et al. observed solely cohesive fracturing of the ice samples, testing the adhesive strength of aluminium in tension at -15°C, resulting in a adhesive strength of 1400 $\pm$300 kPa (21%)[51]. The critical review by Work and Lian compares data from 58 studies, testing common substrate materials (aluminium, steel, Teflon, and polyurethane). Across all test and test methods, the average standard deviation was found to be 24.5% for aluminium, 17.2% for steel, 24.2% for polyurethane, and 124% for Teflon[87]. The standard deviation of the measurements obtained here are in the same range, except for the grit-blasted copper adhesion pad. The substantially larger standard deviation observed in the measurements of the grit-blasted copper adhesion pad, can be the result of pre-fracturing the ice sample while securing the sample clamp, however. Literature values of tensile ice adhesion experiments for copper are not available, literature reporting results from shear tests range from 185-1043 kPa [2, 40].

B.2. Conclusion

Even in controlled environments, water ice is still a natural material with properties that are difficult to control. Despite conducting thorough testing and making adjustments to the experimental setup in order to enhance repeatability, there are still many conditions left to explore. Here the developed adhesion effector is tested in tensile direction, but for the application of robotic systems, tests including shear forces and bending moment are most certainly relevant.

The ample amount of preliminary tests were not in vain; it was found that the adhesion pad height is an important parameter to consider for systems in cold environments. The substrate pad height should provide sufficient clearance between the ice and and other parts of the system, to avoid the ice expansion effect to cause premature failure of the adhesive connection.

A promising result of these experiments is the observed failure mode of the tests, cohesive fracture of the ice indicates that the adhesive strength of the effector is not the limiting factor, this was observed for most adhesion pads tested here. At the same time, this raises more questions about the effectiveness of an ice adhesion approach for robotic systems in situations where ice quality is not guaranteed. Of course, additional measures could be applied to limit the chance failure during operation (e.g. multiple adhesive contact points).

In terms of differences between materials, the average measured adhesion strength was found to be comparable between the same surface treatment. The difference in surface energy of the materials (aluminium having roughly %50 lower surface energy), showed to have no negative effect on the adhesion strength, in fact, aluminium outperformed the copper adhesion pad if only the average adhesion strength is considered. Considering this result in combination with material cost, weight and even temperature response of the adhesion pad in combination with the thermoelectric cooling setup: aluminium is the superior material for the application of a switchable adhesion effector.

It was found that stress concentrations play a significant role in the measured force at break; grit-blasted surfaces outperformed both the polished and grid patterned surfaces. Limiting the interfacial stresses is therefore more important than increasing the substrate contact area, *if* the increased surface area is at the expense of high stress concentrations. Thus, adhesion pad design for robotic systems employing ice adhesion for locomotion or anchoring should be void of sharp or thin features, but an increased surface roughness can prove to be beneficial.

C

Paper

Bio-inspired ice adhesion robot for exploration on Enceladus, an icy moon of Saturn

Thomas Mooijman[1], Stéphanie Cazaux and Jovana Jovanova

Abstract— **Enceladus, one of the icy moons of Saturn, has been of major scientific interest since the Cassini-Huygens mission has explored the Saturn system. This is due to cryovolcanic geysers with complex organic molecules and other ingredients for life in it blasting into space from its subglacial warm ocean. The moon's harsh environmental conditions require innovative bio-inspired locomotion strategies that enable the exploration of Enceladus. This paper presents a novel ice adhesion effector based on the thermoelectric effect to create reversible adhesive connections. The effector developed here has a recorded ice adhesive strength of 1.5 MPa. This strength is enough to support the small-scale robotic system developed in this paper. The robotic system combines a tracked locomotion method with the ice adhesion technology, that enables the robot to move continuously on steep inclined ice walls.**

I. Introduction

Space is closer than ever. Reusable launch vehicles, extremely efficient propulsion systems, commercial space companies and revived public interest has given the space sector an amazing boost over the last few decades. This boost has enabled major advancements in space exploration with NASA returning to the moon in a couple of years and even aiming for manned Mars missions as the next step, turning science fiction into science fact.

Another high priority in space exploration is a mission to the outer solar system, in particular the small icy Saturnian moon Enceladus. After the Cassini-Huygens spacecraft finished its exploration mission of the Saturn system in 2017 after 20 years of research on the planet and its moons, more questions were raised than answers regarding this one small icy moon, Enceladus. This is due to the discovery of cryovolcanic geyser plumes blasting into space from cracks in its ice shell which are located on the south polar terrain [1]. Cassini flew through these plumes on multiple occasions to analyze the composition using onboard mass spectrometers [2]. Plume material was comprised of many different molecules including salts and volatiles but also more complex organic molecules [3], the nature of which still uncertain due to low mass resolution of the instruments. Cassini discovered evidence of a liquid water ocean underneath the ice shell, claimed to be the plume source, and a relatively high heat flux through the same cracks on the south polar terrain [4]. Proof of molecular hydrogen furthermore indicated hydrothermal activity deep within Enceladus [5] [6]. Similar conditions on Earth have been speculated to be one of the most probable sites for development of early terrestrial life[7]. Since these findings, the moon is of major scientific importance due to presence of necessary ingredients for life [2].

Realizing a landed life detection mission to Enceladus that will explore the south polar cracks poses a significant challenge. The extreme environment with mostly unknowns requires the need for a robust, versatile, autonomous and adaptable spacecraft. Current proposals for exploration robots range from melting probes [8], [9] to snake-like robots capable of crawling in the icy crevasses[10]. This project also aims to make use of the existing cracks on the moon to reach the subsurface ocean. To achieve this, a system that can reliably scale icy surfaces is needed. While the physical properties of ice render any existing climbing robots ineffective, this project actually employs the physical properties of ice to develop a new locomotion strategy; the adhesive properties of ice.

This paper presents a novel ice adhesion locomotion strategy, based on the thermoelectric effector to effectuate the phase change of water between liquid and solid. By first developing a switchable ice adhesion effector, the feasibility of this locomotion strategy is evaluated. This effector enforces local phase change on an icy surface, such that liquid water is formed and can adhere to a substrate material (adhesion pad), after which the liquid water is cooled to form ice, this creates a rigid bond between ice and the substrate material. After the adhesion strength of the ice adhesion effector is quantified, the system is miniaturized and integrated in a robotic system to enable movement on icy surfaces.

II. Principles of Ice Adhesion

Ice adhesion has been a popular research topic for decades, however, most studies focus on minimizing ice adhesion strength for de-icing purposes, rather than maximizing. Utilizing ice adhesion to create temporary anchor points relies on the principle that the adhesion force of water is significantly larger in solid phase than in liquid phase. There are multiple mechanisms responsible for ice adhesion on molecular level, in descending order of their contribution: electrostatic interaction, van der Waals forces and covalent of chemical bonding [11]. On a larger scale, the effect of mechanical interlocking has a significant impact on ice adhesion strength, and can cause hydrophobic surfaces to

[1]Thomas Mooijman is with Faculty of Mechanical Engineering, Delft University of Technology, 2628 CD Delft, The Netherlands t.mooijman@gmail.com

have similar adhesion strengths as hydrophilic surfaces made of the same material [12]. Substrate material properties can cause the adhesion strength between ice and substrate to surpass the cohesive strength of ice in some cases [13], this puts an upper limit to the anchoring strength of ∼1 MPa, but is heavily dependent on the quality and temperature of ice.

III. Thermoelectric Effect

The thermoelectric effect, or in this case, the Peltier effect is suitable for the application of a switchable ice adhesion effector, as it can be used as a solid-state heat pump. Peltier elements consist of P- and N- doped semiconductors and rely on the flow of electrons to achieve a temperature differential between the hot and cold side of the element. The electrons in the P- and N- type semiconductors are vibrating on different energy levels, a voltage difference will cause electrons to move from one metal to the other connected via a junction. Electrons moving to a higher energy orbit will release thermal energy, and vice versa. This current proportional heat flow leads to a temperature difference ΔT between the hot side of the module T_{H} and cold side of the module T_{C}. Due to the internal I^2R losses of the module, additional heat accumulates on the hot side of the module, further increasing T_{H}. Failing to dissipate the heat from the hot side will shift the ΔT upwards and eventually it becomes impossible to sustain freezing temperatures on the cold side of the module. It is therefore important to implement appropriate heat dissipation measures to cool the hot side of the module. The benefit of peltier modules is that the direction of heat flow can be reversed by reversing the polarity, such that heating or cooling of the adhesion pad can be achieved with a single peltier element.

IV. Ice Adhesion Effector Design & Experiments

The ice adhesion effector is constructed from three main components; adhesion pad, peltier element, and heat sink. The adhesion pad is the component that contacts the ice to create an adhesive connection, and should be constructed from materials that fit the purpose of this component. First of all, materials with high surface energy are preferred, as benefits the intrinsic ice adhesion strength between substrate (adhesion pad) and adhesive (ice)[14]. Secondly, since the adhesion pad experiences frequent temperature changes, to melt and freeze a small interface of ice, the materials should be able to quickly change temperature. Hence, materials with high thermal diffusivity are favored. With these criteria, copper and 6061 aluminium are selected as substrate materials. Each of these materials are used to produce adhesion pads with three different surface treatments, resulting in a total of six adhesion pads, as shown in figure 1. The adhesion pad surfaces are either, polished to grit K4000, grit-blasted or machined to create a 1 mm deep grid-pattern in the surface. The surface treatments result progressively increasing surface roughness of the adhesion pads, and are used to determine the effect of surface roughness and contact area on ice adhesion strength. Overall dimensions of the adhesion pads are 40x40x14 mm, the contact surface has a circular cross section of 1256 mm^2.

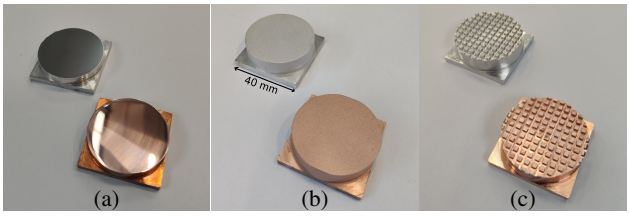

Fig. 1: 6061 and Copper Adhesion Pads: (a) Polished (K4000), (b) Grit-blasted, (c) Grid-pattern

The peltier elements are interfaced with the adhesion pads with thermally conductive paste to ensure proper heat conduction between the two components. For this adhesion effector, TEC1-12706 peltier elements are used, these elements have a maximum cooling rate of 65W and can reach a maximum temperature difference ΔT of 70 K. This temperature difference can only be reached if the heat flow through the peltier is zero. The peltier element is powered by a constant current power source, delivering a current between 1 - 5 A. Heating or cooling of the adhesion pad is achieved by controlling the electrical polarity of the peltier.

The hot side of the peltier is interfaced with a heat sink, to dissipate both the pumped and internally generated heat (I^2R losses). Since the maximum theoretical temperature difference peltier elements can achieve is around 70 K, it is essential to provide ample cooling capacity at the hot side of the element in order to reach sub-zero temperatures at the cold side of the element. For this reason, a liquid cooling system is used to dissipate the heat from the peltier. A copper water cooling block with a constant flow of cooling water at 18°C is interfaced with the hot side of the peltier element.

These parts are combined, and mounted inside a housing produced with additive manufacturing techniques. The 'stack' of components is displayed in figure 2, the top cover of the housing is removed in this figure.

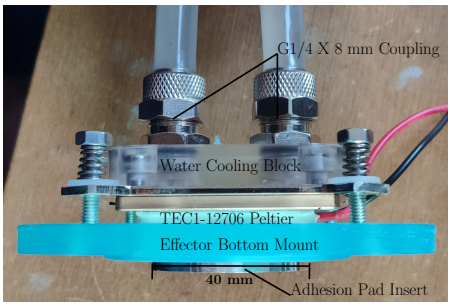

Fig. 2: Components of the adhesion effector (top cover removed).

The adhesion effector is tested to measure the temperature response of the copper and aluminium adhesion pad ma-

terials. In this test, the peltier element is powered with 3 A; 8 V to cool the adhesion pads. Starting temperature of the adhesion pads is equal to the ambient temperature of 18°C. The temperature during the test, as shown in figure 3, is measured by a digital temperature sensor is placed on the outer surface of the adhesion pads. This test shows that the 6061 aluminium is cooled more rapidly by the peltier element, reaching 0°C in 42.9 s, compared to 53.7 s for the copper adhesion pad.

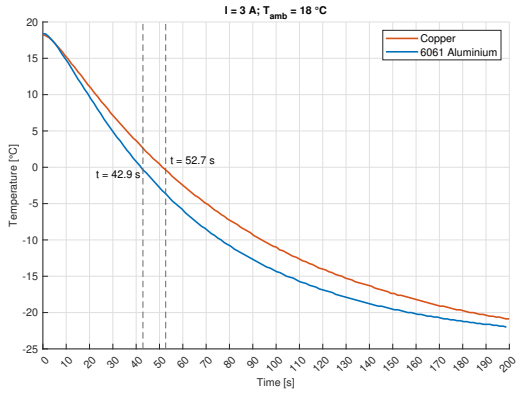

Fig. 3: Temperature response of the copper and aluminium adhesion pads.

In operation, the adhesion pad is not exclusively cooled by the peltier element. Instead, some of the thermal energy is dissipated to the ice and causes the ice to transform from a solid to liquid phase, as required to establish an adhesive connection. As added benefit, the time required to cool the adhesion pad from ambient temperature to 0°C ('time-to-adhere') is also reduced. The time-to-adhere is measured for both materials by placing the adhesion pad on a block of ice, activating the peltier element once the adhesion pad contacts the ice. Meanwhile, the time until movement of the adhesion pad is restricted, as a result from liquid water solidifying between the adhesion pad and ice, is recorded:

- Time-to-adhere, copper: ∼8.5 seconds
- Time-to-adhere, aluminium: ∼6.8 seconds

While copper has a higher thermal diffusivity, the volumetric heat capacity of aluminium is 39% lower. The effect of the reduced heat capacity of the aluminium adhesion pad, is illustrated in both the temperature response graph 3 and the measured time-to-adhere.

V. Ice Adhesion Strength Experiments

The adhesion strength of the effector is quantified with a tensile pull-off test using a Zwick Roell Z100 materials testing machine, this machine is fitted with a temperature chamber to create a controlled environment of -15°C. Ice samples are prepared in stainless steel cups, 80 mm in diameter and 60 mm high. The water used is regular tap water, however the water is boiled before freezing to reduce the dissolved air in the water. Additionally a directional freeze technique is used to force the dissolved gases and minerals in the water to the bottom of the sample, before coming out of solution and freezing. This ensures the top half of the sample is clear ice and free of any defects. Each test is performed with a new sample.

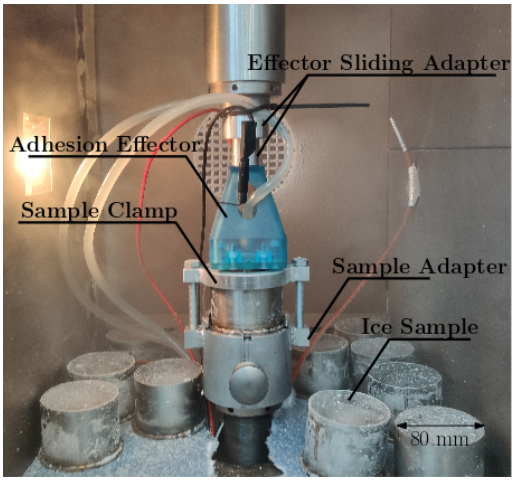

Fig. 4: Tensile pull-off tests to quantify ice adhesion strength of the effector.

During the test, the effector is lowered on the ice sample, briefly heating the ice followed by quickly freezing the liquid water to the adhesion pad. Once the adhesion pad temperature reaches -15°C, the test is initiated and the machine raises the effector with a test speed of 100μm/s, measuring the tensile force until a break is detected. This test is repeated for all six adhesion pads, each tested with six samples, the results are shown in table I.

TABLE I: Mean ice adhesion strength for the six adhesion pads, including standard deviation.

Surface Type	Material	Mean adhesion strength [MPa]	Standard deviation [MPa (%)]
Polished K4000	Copper	1.220	±0.299 (24.5%)
	Aluminium	1.261	±0.253 (20.1%)
Grit-blasted	Copper	1.348	±0.589 (43.7%)
	Aluminium	1.515	±0.239 (15.8%)
Grid Pattern	Copper	1.026	±0.158 (15.4%)
	Aluminium	1.043	±0.218 (20.1%)

Indicating that the aluminium substrate material has a higher adhesion strength compared to copper for all surface treatments. Comparing the surface treatments shows that the grit-blasted surface provides the highest adhesion strength. Conclusively, an aluminium adhesion pad with grit-blasted surface is results in the highest adhesion strength. Then, also considering the temperature response and density of both materials, aluminium is determined to be the preferred material for the implementation of a switchable ice adhesion effector to be integrated in a robotic system.

VI. Ice Climbing Robot

With the adhesion strength of the switchable adhesion effector quantified, together with the substrate material choice, the realization of a robotic system that uses ice adhesion as a locomotion strategy is no longer an abstract idea. The robotic system developed here, uses the tracked locomotion principle in combination with the new ice adhesion technology. A tracked locomotion strategy is well suited for the integration of the adhesion effector components; integrating these parts in the track links creates multiple attachment points on an icy surface to increase overall payload capacity, as illustrated in figure 5. This locomotion strategy also enables continuous motion of the vehicle. In addition to the integration of the adhesion technology in the track links, the heat dissipation system should also be integrated in the payload of the robot, as each individual link requires a constant supply of cooling water. The first prototype is a robot with a single track, movement is therefore limited to 1 Degree of Freedom.

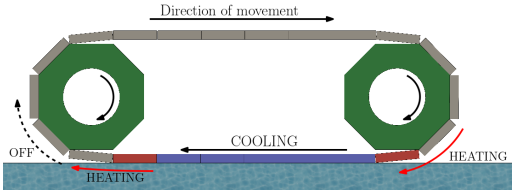

Fig. 5: Concept of tracked locomotion with an ice adhesion strategy.

A. Track Link and Components

The individual track links that make up the whole drive track of the robot need to be equipped with multiple components, similar to the adhesion effector used in the ice adhesion experiments. In addition to the adhesion pad, peltier element and heat sink, the link is also fitted with a mechanical switch to control the polarity of the peltier element. A CAD model of the track link, including all the components, is shown in figure 6.

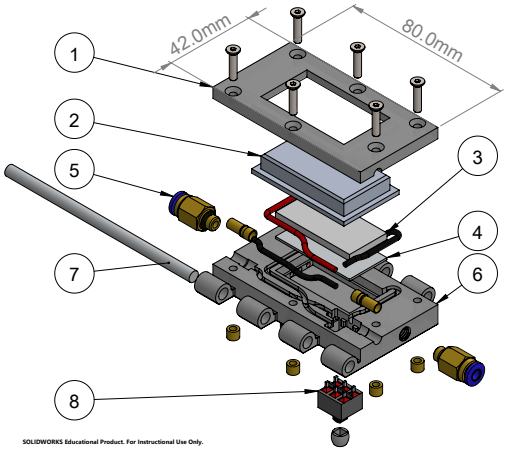

Fig. 6: Exploded view of the track link and components.

In figure 6, the vital components are highlighted; component (1) is the *track link top* and secures the *aluminium adhesion pad* (2) to the *TEC1-06308 peltier element* (3). The peltier element is interfaced with the *heat sink* (4), which is placed inside a cavity of the *track link bottom* (6). The track link bottom has internal water channels that direct incoming water from the *push-in pneumatic coupling* (6) to flow underneath the heat sink. The track links are linked with a *connecting rod* (7) to form a chain. This connecting rod also enables the chain to be driven by a sprocket. Part (8) indicates a modified *Double-Pole Double Throw Switch* (DPDT), this switch functions as a mechanical H-bridge that determines the electrical polarity of the peltier element; controlling the heating and cooling operation of the link. The *track link bottom* and *track link top* are produced using additive manufacturing techniques. Refer to figure 7 for images of an assembled track link.

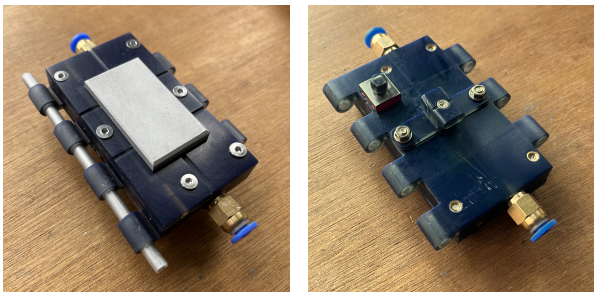

(a) (b)

Fig. 7: Assembled track link; (a) top view, (b) bottom view

B. Robot Frame and Components

The track chain moves around a central frame, driven by a drive sprockets on one side, supported and tensioned by idler sprockets at the other side of the frame. Space inside the frame can be used to accommodate the components required for the ice adhesion technology, as well as the drive-train of the robot. A CAD design is shown in figure 8. The frame is dimensioned such that the track consists of 16 links, such that four links contact the ice at all time.

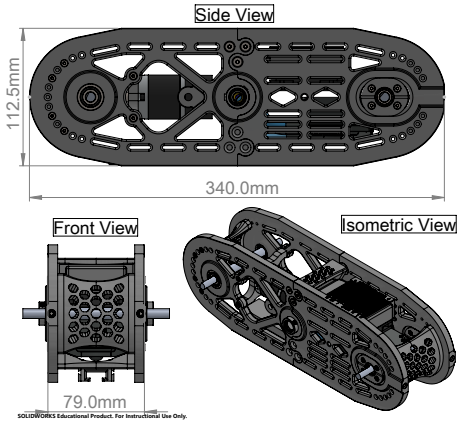

Fig. 8: Multiple views of the robot frame.

A closed water circulation loop is used to provide a continuous supply of cooling water to the track links. Consequently, the heat absorbed by the water should be dissipated to the surroundings to ensure the peltier elements are sufficiently cooled. By integrating this heat dissipation system inside the frame, the robot is not dependent on any external systems to operate; the robot is a self sustaining unit. The heat dissipation system consists of a *water pump* to circulate the water, a *radiator* that transfers the thermal energy from the water to the surroundings with the help of an *axial fan* that creates a forced air convection through the fins of the radiator. These parts are illustrated in figure 9.

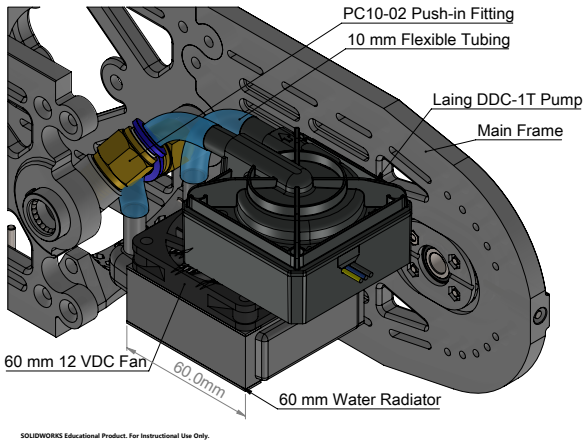

Fig. 9: Heat dissipation system inside the robotic frame.

Since the track is continuously rotating around the central frame, the water loop is fitted with a live swivel in combination with a 16-spout manifold to supply each individual track link with cooling water. The live swivel provides a watertight connection whilst allowing the manifold to rotate freely. An exploded view of this system is shown in figure 10. A rubber O-ring creates a watertight seal between the body of the swivel and the manifold. The ball bearings allow rotation between the two bodies, but prevent axial movement.

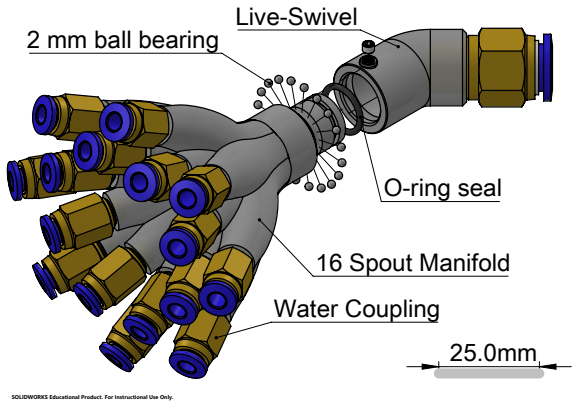

Fig. 10: Water manifold with integrated live swivel.

C. Track Link Control

Controlling the heating and/ cooling timing of the track links is essential to ensure the oncoming track links seize the ice at the beginning of the track run. Similarly, the links should disconnect from the ice at the end of the run. To achieve this, a mechanical control system is implemented that makes use of the fact that the links follow the same trajectory around the frame and the timing of the links can be defined as stationary points along this trajectory. Then, by implementing a cam-follower principle, the mechanical DPDT switches integrated in the track links are actuated at the correct moment. The frame is fitted with multiple guides that interact with the DPDT switches, as illustrated in figure 11.

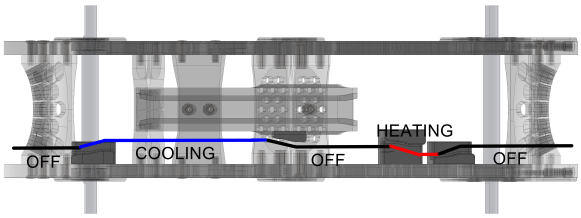

Fig. 11: Mechanical heating/cooling control system, based on a cam-follower principle.

D. Complete System and Demonstration

Combining all the parts of the system, results in the robotic system shown in figure 12. The combined mass of the robot is 4.2 kg, and the system is capable of moving with a velocity up to 80 cm/min. A 12 VDC, 6.5 W, 36mm DC planetary geared motor with an internal gear reduction of 721:1; Model NFP-GA36Y-3525 is selected for driving the robot. The motor has a rated torque of 2.75 Nm, output torque is increased using an additional 3:1 bevel gear reduction, such that the robot has the ability to climb vertically up.

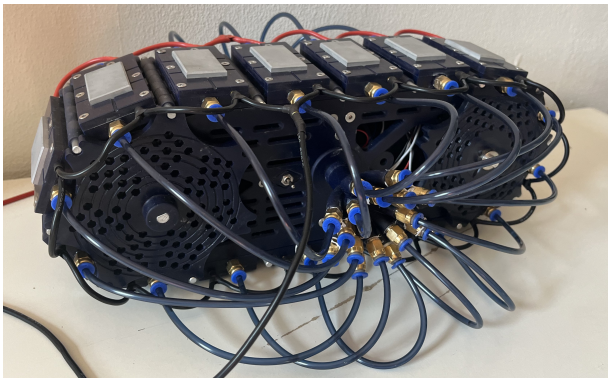

Fig. 12: Assembled ice climbing robot.

The robot's ability to scale icy surfaces is evaluated on a block of ice oriented at different angles. These tests indicate that the robot can successfully travel on inclined surfaces angled up to 60°, as illustrated in figure 13. Steeper angles causes the robot to slightly tilt backward, which in turn

causes the track links to make insufficient contact with the ice, preventing proper adhesion.

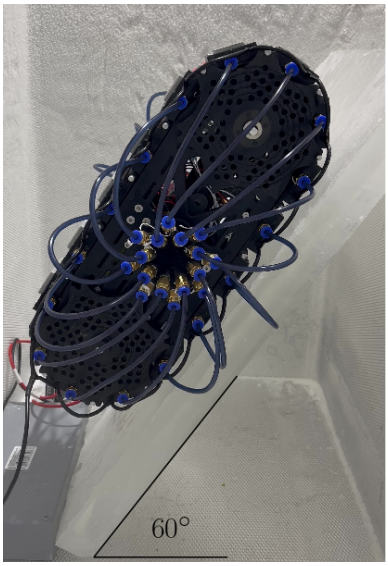

Fig. 13: Robot climbing a sheet of ice with 60° incline.

Additional tests show that once the robot has established adhesive contact points with the ice, the robot can be inverted, and hang upside-down from the sheet of ice, as illustrated in figure 14.

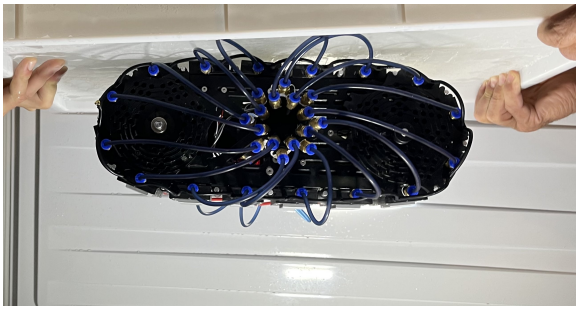

Fig. 14: Robot inverted and anchored to the block of ice.

VII. Conclusion

This paper has investigated the possibility to use the effect of ice adhesion as a locomotion strategy, that can aid the development of exploration robots for extreme environments on earth, or the icy moons found in our solar system. First, a novel ice adhesion effector was developed that employs the thermoeelectric effect to locally effectuate the phase change of water. With this adhesion effector, this work compared the ice adhesion strength of aluminium and copper substrate materials with three different surface treatments: polished, grit-blasted and deep grid pattern. Revealing that the aluminium substrate material with grit-blasted surface provide the best adhesion strength (1.515 MPa). By miniaturizing the components of the ice adhesion effector and integrating this system with a tracked locomotion type, the first ice climbing robot that adopts ice adhesion as a locomotion strategy was developed. The very first prototype is capable of scaling ice walls at a 60°, as well as hanging securely in an inverted position. Further experimental investigations on proper ice wall surfaces are needed to test the reliability of the robot travelling longer distances. Other locomotion methods, such as legged locomotion might be suitable to adopt the developed ice adhesion technology. Future work also includes testing the ice adhesion in low pressure environments, to simulate environmental conditions on Enceladus.

Acknowledgment

We thank the Delft Bioengineering Institute (Delft University of Technology) for supporting and sponsoring this project through the BioDate 2020 initiative.

References

[1] C. C. Porco, P. Helfenstein, P. C. Thomas, A. P. Ingersoll, J. Wisdom, R. West, G. Neukum, T. Denk, R. Wagner, T. Roatsch, S. Kieffer, E. Turtle, A. McEwen, T. V. Johnson, J. Rathbun, J. Veverka, D. Wilson, J. Perry, J. Spitale, A. Brahic, J. A. Burns, A. D. DelGenio, L. Dones, C. D. Murray, and S. Squyres, "Cassini observes the active south pole of enceladus," *Science*, vol. 311, no. 5766, pp. 1393–1401, 3 2006.

[2] J. R. Spencer, A. C. Barr, L. W. Esposito, P. Helfenstein, A. P. Ingersoll, R. Jaumann, C. P. McKay, F. Nimmo, and J. H. Waite, "Enceladus: An active cryovolcanic satellite," in *Saturn from Cassini-Huygens*. Springer Netherlands, 2009, pp. 683–724.

[3] F. Postberg, N. Khawaja, B. Abel, G. Choblet, C. R. Glein, M. S. Gudipati, B. L. Henderson, H. W. Hsu, S. Kempf, F. Klenner, G. Moragas-Klostermeyer, B. Magee, L. Nölle, M. Perry, R. Reviol, J. Schmidt, R. Srama, F. Stolz, G. Tobie, M. Trieloff, and J. H. Waite, "Macromolecular organic compounds from the depths of Enceladus," *Nature*, vol. 558, no. 7711, pp. 564–568, 6 2018.

[4] P. C. Thomas, R. Tajeddine, M. S. Tiscareno, J. A. Burns, J. Joseph, T. J. Loredo, P. Helfenstein, and C. Porco, "Enceladus's measured physical libration requires a global subsurface ocean," *Icarus*, vol. 264, 2016.

[5] J. H. Waite, C. R. Glein, R. S. Perryman, B. D. Teolis, B. A. Magee, G. Miller, J. Grimes, M. E. Perry, K. E. Miller, A. Bouquet, J. I. Lunine, T. Brockwell, and S. J. Bolton, "Cassini finds molecular hydrogen in the Enceladus plume: Evidence for hydrothermal processes," Tech. Rep. [Online]. Available: https://www.science.org

[6] News staff, "Life Originated in Hydrothermal Vents, New Study Suggests," 11 2019.

[7] D. Deamer and B. Damer, "Can Life Begin on Enceladus? A Perspective from Hydrothermal Chemistry," *Astrobiology*, vol. 17, no. 9, pp. 834–839, 9 2017.

[8] K. Konstantinidis, C. L. Flores Martinez, B. Dachwald, A. Ohndorf, P. Dykta, P. Bowitz, M. Rudolph, I. Digel, J. Kowalski, K. Voigt, and R. Förstner, "A lander mission to probe subglacial water on Saturns moon Enceladus for life," *Acta Astronautica*, vol. 106, pp. 63–89, 1 2015. [Online]. Available: https://linkinghub.elsevier.com/retrieve/pii/S0094576514003610

[9] B. H. Wilcox, J. A. Carlton, J. M. Jenkins, and F. A. Porter, "A deep subsurface ice probe for Europa," *IEEE Aerospace Conference Proceedings*, 6 2017.

[10] K. Carpenter, A. Thoesen, D. Mick, J. Martia, M. Cable, K. Mitchell, S. Hovsepian, J. Jasper, N. Georgiev, R. Thakker, A. Kourchians, B. Wilcox, M. Yip, and H. Marvi, "Exobiology Extant Life Surveyor (EELS)," in *Earth and Space 2021*. Reston, VA: American Society of Civil Engineers, 4 2021, pp. 328–338. [Online]. Available: http://ascelibrary.org/doi/10.1061/9780784483374.033

[11] I. A. Ryzhkin and V. F. Petrenko, "Physical mechanisms responsible for ice adhesion," *Journal of Physical Chemistry B*, vol. 101, no. 32, pp. 6267–6270, 8 1997. [Online]. Available: https://pubs-acs-org.tudelft.idm.oclc.org/doi/full/10.1021/jp9632145

[12] J. Chen, J. Liu, M. He, K. Li, D. Cui, Q. Zhang, X. Zeng, Y. Zhang, J. Wang, and Y. Song, "Superhydrophobic surfaces cannot reduce ice adhesion," *Applied Physics Letters*, vol. 101, no. 11, p. 111603, 9 2012. [Online]. Available: https://aip-scitation-org.tudelft.idm.oclc.org/doi/abs/10.1063/1.4752436

[13] E. H. Andrews and N. A. Lockington, "The cohesive and adhesive strength of ice," *Journal of Materials Science 1983 18:5*, vol. 18, no. 5, pp. 1455–1465, 5 1983. [Online]. Available: https://link-springer-com.tudelft.idm.oclc.org/article/10.1007/BF01111965

[14] L. Makkonen, "Ice Adhesion —Theory, Measurements and Countermeasures," *Journal of Adhesion Science and Technology*, vol. 26, no. 4-5, pp. 413–445, 3 2012. [Online]. Available: https://www.tandfonline.com/doi/full/10.1163/016942411X574583